ROTATING CONVECTION DRIVEN BY DIFFERENTIAL BOTTOM HEATING AND ITS APPLICATION

by

Young-Gyu Park

B.A., Seoul National University, Seoul, Korea, 1987
M.S., Seoul National University, Seoul, Korea, 1989
S.M., MIT/WHOI Joint Program, 1993

Submitted in partial fulfillment of the
requirements for the degree of

Doctor of Philosophy

at the

MASSACHUSETTS INSTITUTE OF TECHNOLOGY

and the

WOODS HOLE OCEANOGRAPHIC INSTITUTION

September 1996

Signature of Author .....
Joint Program in Physical Oceanography
Massachusetts Institute of Technology
Woods Hole Oceanographic Institution
July 3, 1996

Certified by .....
Dr. John A. Whitehead
Senior Scientist, W.H.O.I.
Thesis Supervisor

Accepted by .....
Professor Paola Malanotte-Rizzoli
Chairman, Joint Committee for Physical Oceanography
Massachusetts Institute of Technology
Woods Hole Oceanographic Institution

ROTATING CONVECTION WITH DIFFERENTIAL BOTTOM HEATING AND ITS APPLICATION

by
Young-Gyu Park

Submitted in partial fulfillment of the requirements for the degree of
Doctor of Philosophy at the Massachusetts Institute of Technology
and the Woods Hole Oceanographic Institution
July 3, 1999

Abstract

A convection experiment was done with a rotating rectangular tank as a model of oceanic meridional overturning circulation. Heat flux was fixed at one bottom end of the tank using an electrical heater. Temperature was fixed at the other end using a cooling plate. All other boundaries were insulated. The cross sections of temperature field were made at several locations. In equilibrium, the heat input to the fluid H was the same as the meridional heat flux (heat flux from the source to the sink), so it was possible to find a scaling law relating H to the temperature difference across the tank ΔT and rotation rate f. The experimental result suggests that the meridional heat transport in the experiment was mostly due to geostrophic flows with a minor correction caused by the bottom friction. If there was no friction, the scaling law from the experiment resembles the one verified in part in the numerical model by Bryan and Cox (1967). Flow visualization and temperature sections showed that there were meridional geostrophic currents that transported heat. When the typical values of the North Atlantic are introduced, the geostrophic scaling law predicts meridional heat flux comparable to that estimated in the North Atlantic when the vertical eddy diffusivity of heat is about $1cm^2s^{-1}$.

Naturally, this experiment is a only crude model of the oceanic convective circulation. We do not claim that the geostrophic scaling applies in detail to the oceans, however, it may have some important use in climate modeling. For example, almost all existing box models and two-dimensional numerical models of ocean circulation use a frictional scaling law for buoyancy transport. A box model with the geostrophic scaling law is shown to be more robust to a change in the boundary forcing so that it is less likely to have a thermohaline catastrophic transition under the present conditions. It is also shown that a restoring boundary condition for salinity introduces stability to a thermal mode circulation, unless the restoring time for salinity is several orders of magnitude larger than that for temperature.

Thesis Supervisor: John A. Whitehead
Senior Scientist, Department of Physical Oceanography
Woods Hole Oceanographic Institution

Acknowledgments

Throughout my study many people have helped me in many ways, and I want to thank them all.

Most of all, I would like to express my sincere gratitude to my advisor Dr. John A. Whitehead. He believed that I could be a scientist and has been a very patient and supportive mentor for me. During my stay at MIT, Prof. Glenn Flierl enthusiastically taught me various topics, making the learning process great fun. Dr. Karl Helfrich always listen and helped me every time I knocked on his door. Drs. Xin Huang and Jochem Marotzke gave numerous suggestions and comments to improve my thesis. I am grateful to Dr. Nelson Hogg kindly chairing my defense.

Friendship from my friends Joe (my only classmate), Cecilie, Dan, Gary and Javier have helped me to stay sane and survive. Korean guys at MIT, especially J. and Brian, were with me when I needed company. Abbie in the education office taught me how to speak English and live in America. In the laboratory, Bob and John have helped me to perform experiments and prevented me from destroying apparatus and hurting myself.

This work would not be possible without the encouragement and care from my family in Korea. With my love and respect I dedicate this work to my parents in Korea, who have always loved and supported me unconditionally.

This study has been funded by NSF grant number OCE92-01464 and Korean Government Overseas Scholarship Grant.

Contents

Chapter 1

Introduction

The local imbalance between the solar radiation and the earth's back radiation generates a meridional temperature gradient on the surface of the oceans. The temperature gradient drives a well-known vertical convective oceanic circulation. Water in the polar oceans loses heat to the atmosphere, becomes dense, and then sinks to some depth, forming the deep water mass. The water mass flows away from the polar regions and ultimately upwells to the surface to compensate for the sinking. This water gains heat from solar radiation and becomes warm surface water, which then flows toward the polar oceans to satisfy continuity, thus completing the cycle.

The meridional convective circulation is believed to be important in maintaining the climate of the earth and oceans in two ways. First, the oceanic currents carry half of the heat accumulated in the equatorial regions toward the pole (Vonder Haar and Oort, 1973), and compensate the imbalance of the solar radiation and the earth's back radiation. They help to reduce the temperature contrast between the equatorial region and the polar region. Second, the circulation supplies cold water to the upper ocean that balances downward heat diffusion from the surface and helps to maintain the thermocline where temperature changes rapidly.

The most prominent characteristic of oceanic convection is a highly asymmetric circulation pattern. The sinking or "deep water mass formation" is confined to some narrow

polar regions. The upwelling is believed to occur throughout most of the oceans with the exception of the sinking regions. Another asymmetry in the pattern is that most of the vertical temperature gradient is confined to the upper $1000m$ or so of the oceans in a region called the thermocline; the interior of the oceans shows very small vertical temperature gradient compared to that in the thermocline.

Many studies, called thermocline theories, explain how buoyancy forcing and wind stress at the sea surface penetrates to great depths, and creates such a vertical temperature structure in the interior of the oceans (for reviews see Welander; 1986, Pedlosky; 1987, and Huang; 1995). Although it is evident that the thermocline of the oceans is similar to the thermal boundary layer of the circulation driven by differential surface heating, the thermocline theories have not treated the thermocline as a part of convection. In most convection studies, heat transport has been a major goal, but in the thermocline theories, heat transport has not been considered. Furthermore, the thermocline theories cannot explain why the water mass formation region is small.

Studies on convection driven by differential surface heating have been successful in showing the small size of water mass formation regions. A horizontal thermal boundary layer along with an interior of very small vertical temperature gradient was also observed. Even studies of convection in non-rotating frames such as those by Rossby (1965) and Beardsley and Festa (1972) showed the asymmetric circulation pattern. According to Rossby (1965), "The interior is advectively warmed, hence its temperature is an average of the warm fluid supplying it. The heat is withdrawn from it by forcing the warm fluid (by continuity) down against the bottom where it is cooled by conduction. Hence the asymmetry is just a measure of the efficiency by which heat is transported by convection and conduction." These studies might suffice for a brief qualitative explanation of the oceanic convective circulation, but they lack some important factors of the oceanic environment. For example, rotation is an important factor in the dynamics of large scale oceanic flow.

Most of the studies on rotating convection were done using rotating annuli and these mainly had atmospheric applications. One of the most important geometrical differences

between the atmosphere and oceans is that the atmosphere covers all topography and has no lateral boundaries, whereas most oceans, except the Southern Ocean, are bounded meridionally by continents. In the atmosphere, a zonal pressure gradient supported by continents is small, and consequently a meridional geostrophic flow, which is in the direction of the applied temperature gradient, is weak. The heat transport from the equatorial region to the polar region is principally provided by weak ageostrophic flows, eddies and Ekman fluxes, instead. In the oceans (except the Southern Ocean where there is no meridional boundary), meridional boundaries support a zonal pressure gradient that allows meridional geostrophic flows parallel to the applied temperature gradient. The geostrophic flows, thus, are capable of transporting heat from the equatorial oceans (the source of heat) to the polar oceans (the sink of heat).

Numerical studies on large scale ocean circulation showed that meridional geostrophic flow is important in meridional heat transport. For example, Bryan and Cox (1967) derived a scaling law for meridional heat transport based on geostrophy and advective-diffusive heat balance, and confirmed the relation with their numerical circulation model. Colin de Verdière (1988) also showed that the meridional heat transport in his numerical experiment is due to a direct Hadley cell (or vertical circulation cell). In laboratory experiments on thermally driven circulations in a rotating frame, the nature of vertical convective circulation in the presence of meridional boundaries is different from that in an annulus. Condie (1989) and Condie and Griffiths (1989) observed flows that carried heat from the source to the sink. In Speer and Whitehead (1988), horizontal gyres were observed.

Direct estimations using hydrographic data (Bryden and Hall, 1980; Hall and Bryden, 1982) also showed that vertical convective circulation is important in meridional heat transport in the North Atlantic. In the North Pacific, however, due to the lack of deep water mass formation, the meridional heat transport is mostly due to wind-driven circulation (Bryden *et al*; 1991). It is interesting to note that the North Pacific is about twice as large as the North Atlantic, but the meridional heat transport in the North Pacific is about half of that in the North Atlantic (Bryden and Hall, 1980; Bryden *et al.*, 1991).

One way of studying the physics of a phenomenon is to find scaling laws between the parameters. In rotating convection driven by differential heating, the external parameters are the temperature forcing ΔT, the rotation rate f and geometrical constants related to the container and physical properties of the test fluid. The internal parameters are temperature and velocity distributions and heat transport.

If one can find correct scaling laws by whatever means, they can be quite useful in climate studies. In some climate models, major balances in the equation of motion are implemented as simple relations based on assumptions that were not verified. For example, in box models for the thermohaline catastrophe, circulation strength is determined by a scaling law based on a balance between north-south pressure gradient and frictional drag proportional to the strength of the circulation (Stommel, 1961; Marotzke, 1990; Thual and McWilliams, 1992; Huang *et al.*, 1992). This is also true for zonally averaged or two-dimensional circulation models such as studies by Marotzke *et al.* (1988), Thual and McWilliams (1992) and Quon and Ghil (1992). Since the frictional scaling law is set at the value that is appropriate for the present oceans, its value is applicable by definition only to the present oceans. However, studies on the thermohaline catastrophe are dealing with oceans whose density structure varies widely. The predictions of transitions using the frictional relation may not be correct.

One can ask "Don't we have scaling laws for a convective circulation in rotating containers?" There are a few scaling laws based on different dynamics. Using geostrophy and advective diffusive heat balance, one can derive a scaling law for a convective circulation in a rectangular container (Bryan and Cox, 1967; Welander, 1986; Whitehead, 1991). When meridional temperature (buoyancy) forcing is applied along the surface of water in a rectangular container, the meridional boundaries of the container allow zonal pressure gradient. The pressure gradient supports meridional geostrophic flows that carry heat from a source to a sink. This scaling law is equivalent to the classical thermocline theory by Robinson and Stommel (1959).

Another scaling law is for laminar flows in rotating annuli (Stern, 1975; Hignett *et al.*, 1981). There are no vertical boundaries in the meridional (radial) direction, which is

parallel to the applied temperature gradient, so that the meridional geostrophic flows from the source to the sink of heat are not possible. Instead, the thermal forcing drives zonal (axial) geostrophic flows, which are perpendicular to the applied temperature gradient. These flows cannot transport heat directly, but they drive the meridional Ekman flows next to the horizontal boundaries. These frictional flows are parallel to the temperature gradient, and are capable of transporting heat in the meridional direction.

Using baroclinic instability, one can drive another scaling law (Green, 1970; Stone, 1972). When isotherms get shallower to the north, zonal flows can be unstable so that they produce baroclinic eddies that are capable of transporting heat in a meridional direction. The details of the above theories are described in Section 2.1.

One can also ask "Which one of the three mechanisms is most effective for oceanic convective circulation?" Considering that the oceans, excluding the Southern Oceans, have meridional boundaries from the continents and there are well defined large scale meridional flows, the one based on geostrophic flows looks more reasonable for the oceanic convective circulation. There have been only a few physical studies concerning the validity of those scaling laws, however. In simplified numerical models such as zonally averaged models (for instance Marotzke *et al.*, 1988), *a priori* assumptions between the meridional mass flux and meridional pressure gradient were made to close the models. Therefore, they do not contain unbiased scaling laws for heat flux and mass flux.

Three dimensional numerical models that do not make such *a priori* assumptions could conceivably be used to determine a scaling relation. In experiments by Bryan (1987) and Colin de Verdière (1988) on thermally driven circulation, the thermocline thickness and the meridional heat transport follow a simple scaling law based on geostrophy and advective diffusive heat transport (Bryan, 1991). A circulation driven by fresh water flux at the surface follows a similar scaling law based on geostrophy and advective-diffusive salt balance (Huang and Chou, 1994). In the numerical studies on thermally driven circulation, the focus was given to the dependence of the circulation on the vertical heat diffusivity κ. A functional relation between buoyancy forcing and convective circulation, which has not been considered

in those studies, must be equally important for climate, since a change in buoyancy forcing modifies convective circulation and subsequently climate, and vice versa.

With a laboratory experiment with a fluid one does not have to make any *a priori* assumptions about dynamics. It is also often easy to change and explore wide ranges of parameters so that one can find relations among a number of parameters (scaling laws). The isolation of phenomena of interest is also easy. The Rayleigh number, which is one of the most important parameters of convection and represents the ratio of buoyancy forcing to viscous dissipation and heat diffusion, can be several orders of magnitude larger in a laboratory fluid than in a numerical model. Most earlier laboratory experiments on circulation driven by differential heating along a horizontal surface, however, did not have enough precision to find a scaling law for thermal convection.

In this thesis, an experimental study on circulation driven by differential bottom heating in a rotating frame has been performed. The experiment is intended to understand the basic physics of rotating convection in a square container and hence the thermal component of the thermohaline circulation. Given a surface heat flux distribution, we seek to answer the following main questions with the experiments:

1. What are the scaling laws governing the temperature field and heat transport?
2. What does the convective flow field look like?
3. What are the strength and limitations of this experiment as a model of oceanic thermal circulation?

In Chapter 2, previous experimental, theoretical and numerical studies on meridional overturning circulation and their scaling laws for the circulation are reviewed. The experiment and the results are also described in the chapter. Scaling laws are compared with the data from the experiment, and the more successful ones are discussed. The implication of the experimental results to oceanic thermal convection are discussed. In Chapter 3, the results from the experiment were applied to a simple climate model. A simple two-box model based on Stommel (1961) but utilizing the scaling law from the present experiment was developed. The effects of oceanic meridional buoyancy transport on the stability and

climate of thermohaline circulation were studied. The effects of air-sea fresh water (salt) exchange parameterization on the stability were also studied and compared with those of the meridional buoyancy transport. A brief summary and conclusion are drawn in Chapter 4.

Chapter 2

Convection Driven by Differential Bottom Heating

2.1 Previous Studies

2.1.1 Non-rotating System

Rossby (1965) developed a scaling law for convective circulation driven by differential surface heating in a non-rotating system. A temperature difference ΔT was maintained along the bottom of a tank, and all other boundaries were insulated. The configuration is equivalent to an upside-down, non-rotating ocean. A highly asymmetric convection cell, which consisted of a narrow rising region, a thin thermal boundary layer along the bottom, and an interior of almost uniform temperature was observed as can be seen in Fig. 2.1.

The balance between buoyancy forcing and vertical viscous dissipation in the thermal boundary layer,

$$\nu v_{zzz} \approx \alpha g T_y,$$

yields a meridional velocity scale V_n

$$V_n \equiv \frac{\alpha g \Delta T \delta_{T_n}^3}{\nu l_y}. \tag{2.1}$$

Here, y is the meridional direction, which is parallel to the temperature gradient at the bottom, z is positive upward, δ_{T_n} is the thickness scale of a thermal boundary layer, ΔT is

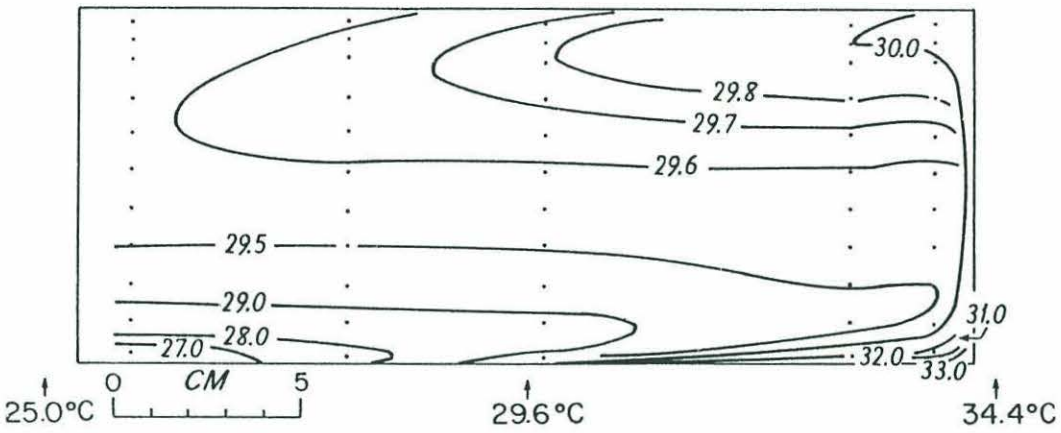

Figure 2.1: A temperature section from Rossby (1965) (Fig. 5b in the paper). A thermal boundary layer and an interior of nearly uniform temperature can be seen. Note that isotherms are not drawn at equal intervals.

thermal forcing, v is the meridional velocity, l_y is the length of the tank, g is gravitational constant, α is the thermal expansion coefficient, ν is the kinematic viscosity of water, and the subscript 'n' represents a non-rotating system. In the heat equation, the balance between advection and vertical diffusion in the thermal boundary layer,

$$wT_z \approx \kappa T_{zz}$$

yields a vertical velocity scale W_n

$$W_n \equiv \frac{\kappa}{\delta_{T_n}}$$

where w is vertical velocity and κ is the thermal diffusivity of water. If we use continuity

$$V_n = l_y \frac{W_n}{\delta_{T_n}},$$

then

$$V_n = \frac{\kappa l_y}{\delta_{T_n}^2}. \tag{2.2}$$

The replacement of Eq. 2.2 in Eq. 2.1 yields

$$\begin{aligned} \delta_{T_n} &= l_y Ra^{-1/5} \left(\sim \Delta T^{-1/5}\right), \text{ and} \\ Q_n &= \kappa Ra^{1/5} \left(\sim \Delta T^{2/5}\right), \end{aligned} \tag{2.3}$$

where Rayleigh number $Ra = \alpha g \Delta T l^3/\nu\kappa$, and $Q_n \equiv V_n \delta_{T_n}$ is the mass transport in the thermal boundary layer per unit width of the tank. By comparing his experimental results (Table 2 in Rossby, 1965) and the estimations from the scaling law (Table 3 in the paper), one can find linear relations between them as follows:

$$\begin{aligned} \delta_{T_{exp}} &\approx 1.1\delta_{T_n} \\ Q_{exp} &\approx 0.5 Q_n. \end{aligned}$$

The scaling law compares well with the experimental results. In the thermal boundary layer, the water flows from the cold end to the hot end, and the meridional heat flux H_n per unit width is,

$$H_n \equiv \rho_o C_p \Delta T Q_n \sim Ra^{6/5} \left(\sim \Delta T^{6/5}\right). \tag{2.4}$$

In the numerical experiment by Somerville (1967), the circulation pattern is slightly asymmetric and $H \sim Ra^{8/5}$ $(\Delta T^{8/5})$. The results are different from those of Rossby (1965). In the numerical study, $10 < Ra < 10^4$ and it is much smaller than the range $10^6 < Ra < 10^9$ in Rossby (1965). Using a numerical study, Beardsley and Festa (1972) showed that when $Ra \approx 10^5$, the power dependence of H on Ra changes from Somerville's to Rossby's. The asymmetry in the circulation intensified as Ra increases (Fig. 1 in the paper). We can deduce that the asymmetry in the circulation is the nature of convection in the limit of large Ra.

Nelken (1987) assigned heat flux instead of temperature along the top boundary of a non-rotating box in his numerical study, and claimed different scaling laws as follows:

$$\begin{aligned} Q_n &\sim Ra_f^{1/6} (\sim H_n^{1/6}), \quad \text{and} \\ \delta_{T_n} &\sim Ra_f^{-1/6} (\sim H_n^{-1/6}). \end{aligned}$$

In his work, heat flux H was fixed, so the flux Rayleigh Number $Ra_f \equiv Hd/\rho_o C_p \kappa$. Since $\Delta T Q_n \sim H_n$,

$$\Delta T \sim Ra_f^{5/6}.$$

If we rewrite Nelken's (1987) scaling laws using Ra (or ΔT), although it is not an external parameter,

$$\delta_{T_n} \sim Ra^{-1/5} \left(\sim \Delta T^{-1/5}\right), \quad Q_n \sim Ra^{-1/5} \left(\sim \Delta T^{1/5}\right)$$

$$\text{and } H_n \sim Ra^{6/5} \left(\sim \Delta T^{6/5}\right).$$

Therefore, Nelken's (1987) and Rossby's (1965) scalings were equivalent, although Nelken (1987) compared differently defined Rayleigh numbers without appropriate conversion and concluded that convection with a heat flux boundary condition yields different scaling laws from those with a temperature boundary condition.

2.1.2 Ekman Scaling Law

A rotating annulus or "dishpan" has been used in many studies about convective circulation. Through the thermal wind balance, a meridional (radial) temperature difference ΔT, which is imposed externally, drives a zonal (axial) geostrophic flow in the interior, as sketched in Fig. 2.2. The zonal flow is perpendicular to the applied temperature gradient so it cannot transport heat. At the horizontal (top and bottom) boundaries, a no slip condition is satisfied and Ekman layers are established. In the Ekman layers, the geostrophic zonal velocity becomes weaker due to the friction and the Coriolis force cannot balance the meridional pressure gradient. Ekman fluxes, which are parallel to the temperature gradient and are capable of transporting heat, are induced by the interior zonal geostrophic flow. Almost all of the meridional mass and heat transport is due to the Ekman fluxes in the top and bottom Ekman layers. Thus, the scaling law described in this section will be called an **Ekman scaling law**.

Hignett *et al.* (1981) developed scaling laws in a rotating annulus with a differentially heated bottom in several different regimes, which depend on f and ΔT. Each regime can be defined using the ratio of the thermal boundary layer scale of Rossby (1965) (Eq. 2.1.1(a)) to the Ekman depth $\delta_E = dE^{1/2}$, where Ekman number, $E = 2\nu/fd^2$, and is d the depth of a container. The square of the ratio

$$r \equiv \left(\frac{\delta_T}{\delta_E}\right)^2 = Ra^{-2/5}E^{-1}\left(\frac{l_y}{d}\right)^2 \sim f\Delta T^{-2/5} \tag{2.5}$$

represents the importance of rotation. Here, l_y is the length of the container which for annuli would be the difference between inner and outer radii.

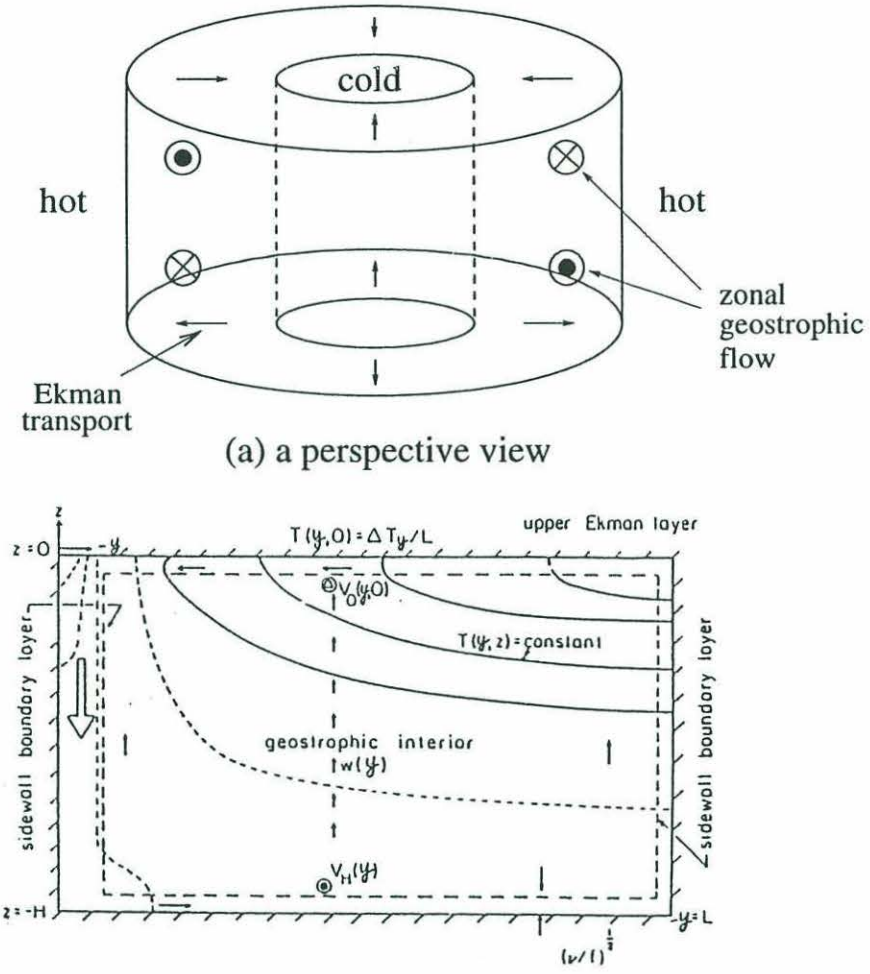

Figure 2.2: Schematic convective flow pattern in a rotating annulus. (a) a perspective view and (b) a radial (meridional) section (adapted from Stern's (1975) Fig. 12.2). The interior zonal (axial) geostrophic flows ($\otimes$ and $\odot$) are perpendicular to the applied temperature gradient. These cannot transport heat directly from the hot end to the cold end. The Ekman fluxes (thin arrows) which are driven by the interior geostrophic flows, are in the direction of the temperature gradient and transport the heat.

When rotation is weak ($r < 1$), the scaling law for the thermal boundary is basically the same as that of Rossby (1965). As the rotation becomes strong ($r \sim O(1)$), the increased Ekman spiral tendency reduces Q_e, and thickens the thermal boundary layer. Here the subscript 'e' is for a quantity related to the Ekman scaling law. For fast rotation rates ($r > O(1)$), the thermal boundary layer is thicker than the Ekman layer, and the thermal wind balance away from the Ekman layer,

$$-fu_z = g\alpha T_y,$$

yields interior zonal geostrophic velocity scale U_e

$$U_e \equiv \frac{g\alpha\delta_{T_e}\Delta T}{fl_y}. \tag{2.6}$$

In the heat equation, the balance between vertical advection and vertical diffusion,

$$wT_z \approx \kappa T_{zz},$$

yields vertical velocity scale W_e

$$W_e \equiv \frac{\kappa}{\delta_{T_e}}. \tag{2.7}$$

Meridional mass flux per unit area within the thermal boundary layer Q_e, which is the Ekman flux driven by the zonal flow, is (Pedlosky, 1987)

$$Q_e \equiv \frac{1}{2}U_e\delta_E. \tag{2.8}$$

Since there is no zonal variation ($\partial/\partial x = 0$) and no meridional geostrophic flow in the interior ($v = 0$), continuity gives $w_z = 0$ in the interior away from the top and bottom Ekman layers. The variation of w is confined to the Ekman layers so

$$W_e \equiv \frac{\delta_E U_e}{l_y}. \tag{2.9}$$

The above relations can be written using thermal forcing ΔT and physical and geometrical constants as follows:

$$\begin{aligned} Q_e &= \left(\frac{\nu(g\alpha\kappa\Delta T)^2}{f^3}\right)^{1/4}, \quad \text{and} \\ \delta_{T_e} &= l_y\left(\frac{\kappa^2 f^3}{\nu(g\alpha\Delta T)^2}\right)^{1/4}. \end{aligned} \tag{2.10}$$

The meridional heat flux per unit area H_e/l_x is then

$$\frac{H_e}{l_x} = \rho_o C_p \left(\frac{\nu (g\alpha\kappa)^2 \Delta T^6}{f^3} \right)^{1/4} . \tag{2.11}$$

The regime $r > O(1)$ is the same as that of Stern (1975), so both studies show the same scaling law. When $r \gg 1$, the thermal boundary layer extends beyond the depth of the annulus. The temperature field satisfies Laplace's equation. Meridional heat transport is due to diffusion so it becomes independent of f.

Fig. 2.3(a) is a meridional temperature section of Hignett *et al.*'s (1981) experimental results (Fig. 3 of their paper) when $f = 0$. A thermal boundary layer near the bottom can be seen clearly. Fig. 2.3(b) (Fig. 4 of their paper) is a meridional temperature section with fast rotation ($r = 2.88$). A thicker thermal boundary layer was observed, as their theory (Eq. 2.10(b)) predicted. However, due to the technical difficulty of making accurate heat flux measurement, they could not verify their scaling law for heat flux.

In an annulus, the pattern of the flow field is effectively two dimensional since meridional geostrophic flow is not possible. In the oceans, however, the flow field is three dimensional so the meridional geostrophic velocity is comparable to the zonal geostrophic velocity. Observations (Hall and Bryden, 1982) showed that the meridional geostrophic velocity is important in the meridional heat transport. The scaling law for an annulus may not be applicable to the oceans.

2.1.3 Baroclinic Eddy Scaling Law

Convection in an annulus or dishpan shows an interesting phenomenon, regardless of the way that buoyancy forcing was imposed. When rotation is slow, flow is axially symmetric and a direct meridional circulation cell appears along with zonal flow. This symmetric flow is usually called the Hadley regime, since it resembles the symmetric component of the atmospheric circulation identified by Hadley. When rotation becomes fast, baroclinic instability develops so irregular wave-like fluctuations and meandering zonal jets form. This type of flow is usually called the Rossby regime. If rotation becomes even stronger, the

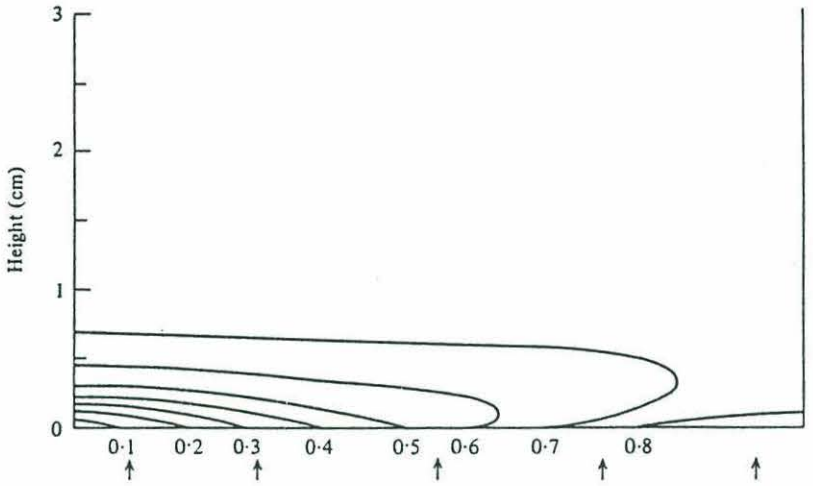

FIGURE 3. A radial temperature cross-section at $\gamma = 0$, $Ra = 2{\cdot}34 \times 10^8$, working fluid water, $d = 10{\cdot}0$ cm. The isotherms are expressed as fractions of ΔT and were drawn subjectively from vertical temperature profiles at the arrowed positions. The gradients above about 1 cm are too weak to include.

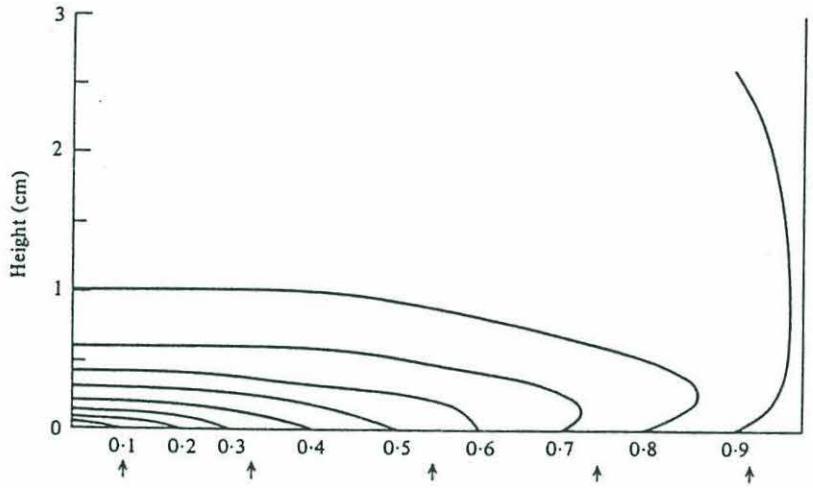

FIGURE 4. As for figure 2 except $\gamma = 2{\cdot}88$, $Ra = 2{\cdot}38 \times 10^8$, $E = 1{\cdot}55 \times 10^{-4}$, working fluid water. Note the slight deepening of the thermal layer and the increase of the interior temperature from $\gamma = 0$.

Figure 2.3: Temperature sections from Hignett *et al.* (1981) with (a) for zero rotation and (b) for fast rotation. Thermal boundary layers can be seen in both figures. The thermal boundary layer is thicker in (b) as their theory predicted.

Hadley regime reappears (Holton, 1992). The kinetic energy of baroclinic eddies is derived from the available potential energy of the mean flow due to the meridional temperature gradient. The eddies rearrange the mean field toward a lower potential energy state so that the heat must be transferred poleward. Thus, a scaling law based on the eddies, a **baroclinic eddy scaling law**, could be obtained (Green, 1970; Stone, 1972).

When the meridional slope of an isotherm is δ_{T_b}/l_y (subscript 'b' for the baroclinic scaling law), the available potential energy ($A.P.E.$)

$$A.P.E. \sim \rho_o g\alpha\Delta T\delta_{T_b}.$$

Since $A.P.E.$ is the source of eddy kinetic energy, we can define

$$V_b^2 \equiv g\alpha\Delta T\delta_{T_b},$$

where V_b is the velocity scale of eddies. The meridional heat flux due to baroclinic eddies is

$$\overline{v'T'} \sim CV_b\Delta T = C(g\alpha\delta_{T_b}\Delta T^3)^{1/2}.$$

Here, primed variables represent eddy related quantities.

Since the release of $A.P.E.$ may depend on rotation and stratification, C, the correlation coefficient between v' and T', may not be a constant. In Green (1970), the application was limited to the atmosphere and he treated C as a constant. Stone (1972), however, generalized the idea by assuming that over a long time the vertically averaged amplitude of the baroclinic eddies was equal to that of the baroclinic component of the mean zonal wind, and found through his calculation that

$$C \equiv \left(\frac{N\delta_{T_b}}{fl_y}\right)^2,$$

where $N^2 = g\alpha\Delta T/\delta_{T_b}$. Thus,

$$\overline{v'T'} \sim \left(\frac{(g\alpha)^3\delta_{T_b}^3\Delta T^5}{f^4 l_y^4}\right)^{1/2}.$$

Since $(\overline{v'T'})/l_y \approx (\overline{w'T'})/\delta_{T_b}$, the heat equation

$$(\overline{v'T'})_y + (\overline{w'T'})_z = \kappa\overline{T}_{zz}$$

yields

$$\overline{v'T'} \sim \frac{\kappa l_y \Delta T}{\delta_{T_b}^2}.$$

We, then, can define a scale for the thermal boundary layer thickness δ_{T_b}

$$\delta_{T_b} \equiv \left(\frac{\kappa^2 l_y^6 f^4}{(g\alpha\Delta T)^3} \right)^{1/7}. \tag{2.12}$$

Meridional heat transport per unit width of a basin is

$$\begin{aligned} \frac{H_b}{l_x} &\equiv \rho_o C_p \delta_T \overline{vT'} \\ &\sim \rho_o C_p \left(\frac{(g\alpha)^3 l_y \kappa^5 \Delta T^{10}}{f^4} \right)^{1/7}. \end{aligned} \tag{2.13}$$

The above relation holds where mean flow is predominantly zonal. In the atmosphere and the Southern Oceans, the mean flows are zonal so the scaling law may be applicable. However, in the Atlantic, Pacific or Indian Oceans, strong meridional currents, which are known to be important in meridional heat transport, are observed near the meridional boundaries. During the release of the available potential energy, the cold water in the northern half of the domain sinks and the warm water in the southern half rises. A symmetric meridional overturning circulation cell (Gill, 1982), which is not compatible with the asymmetric thermohaline circulation of the oceans, is developed.

2.1.4 Geostrophic Scaling Law

Assume that a meridional (north-south) temperature difference ΔT is applied to the surface of water in a rectangular basin. The water near the cold (northern) end becomes dense and sinks rapidly to the bottom. The water then flows toward the hot (southern) end while ascending toward the surface. At the surface, water flows from the hot end toward the cold end. Since the active descending motion (water mass formation) occurs over a small region near the cold end, if the water mass formation region is excluded, the flow pattern can be simplified as a two layer lock-exchange flow with vertical motion across the interface as shown in Fig. 2.4.

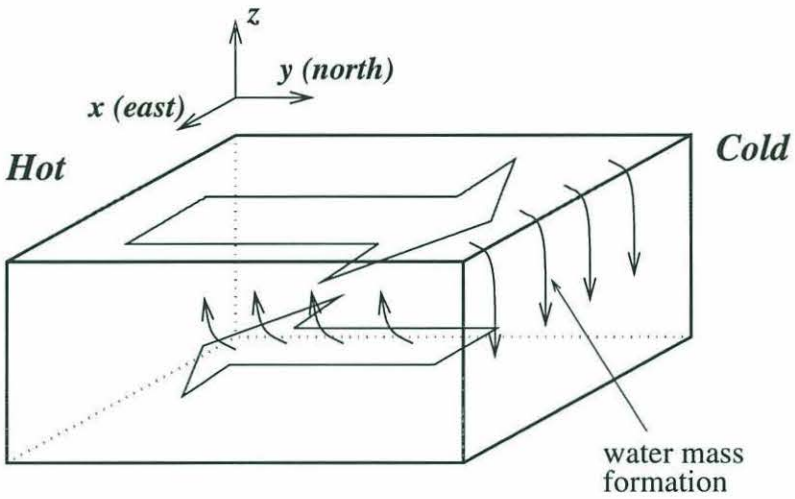

(a) a perspective view

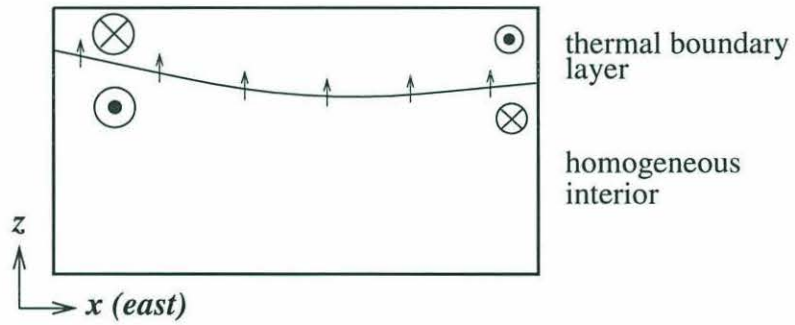

(b) a zonal section

Figure 2.4: Schematic convective flow pattern driven by meridional temperature gradient at the surface of a rectangular basin. (a) a perspective view of meridional circulation, and (b) a zonal section. See the text for the detail.

In addition to the meridional overturning circulation, the vertical motion stretches the lower layer and generates cyclonic relative vorticity to conserve potential vorticity, and shrinks the upper layer and generates anticyclonic vorticity. In the western half, the vortical motion and the meridional overturning circulation are in the same direction in each layer so that strong flows occur. These strong flows happen in an f-plane so they are different from western boundary currents in a β-plane. In the eastern half, the motion due to the relative vorticity and the meridional overturning circulation are in opposite directions. If the horizontal motion due to the relative vorticity is stronger than meridional overturning circulation, horizontal gyres become dominant in each layer. This schematic flow pattern is similar to those of Colin de Verdiére's (1988) and Winton's (1996) numerical experiments in f-plane oceans.

A scaling law for such a meridional overturning circulation based on geostrophy and advective-diffusive heat balance, a **geostrophic scaling law**, can be found in many studies (Bryan and Cox, 1967; Welander, 1971a and 1986; Bryan, 1987; Colin de Verdiére, 1988; Whitehead, 1991; Huang and Chou, 1994; Winton, 1996). Consider that meridional temperature gradient ($T_y = \Delta T/l_y$) is given along the surface of a rectangular basin, where l_y is the length of the basin. In a numerical study by Huges and Weaver (1994), within the thermal boundary layer the North Atlantic overturning is almost linearly proportional to the meridional difference in the zonal average of depth-integrated steric height between the latitude of maximum zonally averaged surface density and the southern limit of the North Atlantic ($1.75°N$). The results suggests that the zonal temperature gradient (T_x) that drives the meridional overturning circulation is linearly proportional to the meridional temperature gradient.

If we assume $T_x \sim T_y$ in the thermal boundary layer, thermal wind balance yields a meridional velocity scale V_g

$$V_g \equiv \frac{g\alpha\Delta T\delta_{T_g}}{fl_y}. \tag{2.14}$$

The assumption $T_x \sim T_y$ is equivalent to an assumption $V_g \sim U_g$, where U_g is a zonal velocity scale. The meridional movement of a fluid must be compensated by upwelling into

the thermal boundary layer so

$$W_g \equiv \frac{V_g \delta_{T_g}}{l_y}. \tag{2.15}$$

If we further assume that the vertical advection of the cold water is balanced by the downward diffusion of heat from the surface within the base of the thermal boundary layer (Munk, 1966), i.e.,

$$wT_z \approx \kappa T_{zz},$$

we can obtain

$$W_g \equiv \frac{\kappa}{\delta_{T_g}}. \tag{2.16}$$

The horizontal advection of heat was not considered in the above relation but if we use continuity

$$vT_y \approx U_g \Delta T / l_y \approx W_g \Delta T / \delta_{T_g} \approx wT_z.$$

Thus, all the terms in the heat equation are equally important.

From Eqs. 2.14, 2.15 and advdiff, one can get

$$\delta_{T_g} = \left(\frac{\kappa l_y^2 f}{g \alpha \Delta T} \right)^{1/3}, \tag{2.17}$$

$$U_g = \left(\frac{\kappa (g \alpha \Delta T)^2}{l_y f^2} \right)^{1/3}. \tag{2.18}$$

Meridional mass transport per unit width Q_g is then

$$Q_g = U_g \delta_{T_g} = \left(\frac{\kappa^2 l_y g \alpha \Delta T}{f} \right)^{1/3}. \tag{2.19}$$

The meridional heat flux per unit width H_g / l_x is thus

$$\begin{aligned} \frac{H_g}{l_x} &\equiv \rho_o C_p \Delta T Q \\ &= \rho_o C_p \left(\frac{l g \alpha \kappa^2 \Delta T^4}{f} \right)^{1/3} \end{aligned} \tag{2.20}$$

Here, l_x is the width of the basin.

The geostrophic scaling law is discussed for convective circulation in an f-plane basin, but in numerical studies by Bryan and Cox (1967 and 1968), Bryan (1987), Colin de Verdiére

(1988), Huang and Chou (1994), and Winton (1996), the scaling law was applied to thermally driven circulations in β-plane basins. Bryan and Cox (1967 and 1968) found that the meridional heat transport from model is about 0.3 of that from the geostrophic scaling law. In their studies, only a few points in the parameter space were considered so that their data are not enough to establish a definite relation. In Bryan (1987) and Colin de Verdiére (1988), the power dependences of properties related to meridional overturning circulation on κ were studied. The thermocline thickness δ_T follows

$$\delta_T \sim \kappa^{1/3},$$

reasonably well as the geostrophic scaling law suggests. The meridional heat transports in Bryan (1987)'s experiment and Colin de Verdiére (1988)[1] also follow the scaling law (Bryan, 1991), so

$$H \sim \kappa^{2/3}.$$

The meridional mass transport Q, however, shows different relations. In Bryan (1987), $Q \sim \kappa^{1/3}$. Later, Huang and Chou (1994) suggested that Bryan (1987)'s experiments did not reach equilibrium states, and in equilibria $Q \sim \kappa^{1/2}$. In Colin de Verdiére (1988), the kinetic energy $\sim \kappa^{2/3}$ and he concluded that the velocity scale follow the scaling law since $U \sim \kappa^{1/3}$ yields $U^2 \sim \kappa^{2/3}$. It is not clear how the kinetic energy is defined, but if it is an average over a meridional section, the kinetic energy is proportional to $U^2\delta_T$. Since $Q^2 \sim U^2\delta_T^2 \sim \kappa^{2/3+1/3}$, $Q \sim \kappa^{1/2}$. There is no clear explanation why Q does not follow the scaling law whereas δ_T and H do.

Huang and Chou (1994) derived a scaling law for a convective circulation in a β-plane driven by precipitation and evaporation $(E - P)$ using thermal wind relation, advective-diffusive salt balance, continuity and the salt conservation. Their scaling law is physically the same as the geostrophic scaling law. If we consider H as a variable and write ΔT, δ_T and Q using H (as in Table 2.1) and and replace ΔT by ΔS and $H/\rho_o C_p$ by $l_y(E - P)\overline{S}$,

[1]Colin de Verdiére (1988) concluded that $H \sim \kappa^{1/2}$ in his experiment but $H \sim \kappa^{2/3}$ is also a statistically acceptable fit (Bryan, 1991 and see Fig. 4 of the paper).

we can get their scaling law. Here, ΔS is the meridional salinity contrast and $\overline{S}$ the mean salinity. Their scaling law was confirmed by their numerical experiments.

2.1.5 Comparison of the Scaling Laws

A brief summary of the three scaling laws discussed in the previous sections is shown in Table 2.1. If thermal forcing ΔT is known, meridional heat flux H, and thermal boundary layer thickness δ_T, can be represented using ΔT and other external parameters such as f, the physical properties of the test fluid, and the geometrical constants of the container. If H is known as in the present experiment (described in the next section), ΔT and δ_T can be represented using H and other external parameters of an experiment.

The three scaling laws are compared in Fig. 2.5. In Fig. 2.5(a), which shows the dependence of ΔT on f for fixed H, the geostrophic scaling law shows lowest ΔT for the same heat flux; thus the geostrophic scaling law is the most effective in transporting heat. This is natural since the geostrophic scaling law allows geostrophic flow that carries heat from the source to the sink directly, while the other scaling laws do not.

A thermal boundary layer thickness can be treated as an indicator of heat transfer efficiency, independent of meridional heat transfer mechanism. Heat loss to the system by deep water mass formation (heat input for an upside down ocean like the present experiment) H is the same as diffusive heat input (loss) through the surface (bottom) excluding the water mass formation region, which is $H \sim \kappa\Delta T/\delta_T$; thus, $\delta_T \sim \kappa\Delta T/H$. Here ΔT can be treated as buoyancy forcing and H meridional heat flux. When buoyancy forcing ΔT is fixed, a system with higher heat transfer efficiency gives higher H and subsequently a thinner thermal boundary layer. When H is fixed, ΔT and δ_T are the smallest in the most effective system. The geostrophic scaling law is the most effective in meridional heat transport, so it shows the smallest δ_T as shown in Fig. 2.5(b), which represents the dependence of δ_T on f for fixed H. Note that in the figure, ΔT and δ_T from the Ekman scaling law and the baroclinic eddy scaling law show similar magnitude and f dependence. It may not be easy to differentiate the two scaling laws in laboratory or numerical experiments where

	geostrophic scaling law	Ekman scaling law	baroclinic eddy scaling law
$H(\Delta T, f)$	$\left[\rho_o C_p l_x (l_y g\alpha\kappa^2)^{1/3}\right] f^{-1/3}\Delta T^{4/3}$	$\left[\rho_o C_p l_x \nu^{1/4}(g\alpha\kappa)^{1/2}\right] f^{-3/4}\Delta T^{3/2}$	$\left[\rho_o C_p l_x \{l_y (g\alpha)^3\kappa^5\}^{1/7}\right] f^{-4/7}\Delta T^{10/7}$
$\delta_T(\Delta T, f)$	$\left[\left(\frac{l_x l_y \kappa}{g\alpha}\right)^{1/3}\right] f^{1/3}\Delta T^{-1/3}$	$\left[l_y\left(\frac{\kappa^2}{(g\alpha)^2\nu}\right)^{1/4}\right] f^{3/4}\Delta T^{-1/2}$	$\left[\left(\frac{(\kappa l_y^3)^2}{(g\alpha)^3}\right)^{1/7}\right] f^{4/7}\Delta T^{-3/7}$
$\Delta T(H, f)$	$\left[\{(l_x\rho_o C_p)^3 (l_y g\alpha\kappa^2)\}^{-1/4}\right] f^{1/4} H^{3/4}$	$\left[\{\nu(\rho_o C_p l_x)^4 (g\alpha\kappa)^2\}^{-1/6}\right] f^{1/2} H^{2/3}$	$\left[\{l_y(\rho_o C_p l_x)^7 (g\alpha)^3\kappa^5\}^{-1/10}\right] f^{2/5} H^{7/10}$
$\delta_T(H, f)$	$\left[\left(\frac{\rho_o C_p l_x l_y^3 \kappa^2}{g\alpha}\right)^{1/4}\right] f^{1/4} H^{-1/4}$	$\left[l_y\left(\frac{(l_x\rho_o C_p\kappa^2)^2}{\nu(g\alpha)^2}\right)^{1/6}\right] f^{1/2} H^{-1/3}$	$\left[\left(\frac{l_y^9 (l_x\rho_o C_p)^3\kappa^5}{(g\alpha)^3}\right)^{1/10}\right] f^{2/5} H^{-3/10}$

Table 2.1: A summary of scaling laws. In the table, ρ_o is reference density, C_p specific heat, κ thermal diffusivity, ν viscosity, α thermal expansion coefficient, g gravitational constant, l_x the width, and l_y is the length of the tank. Quantities inside the square brackets have fixed values in the experiment to be described here.

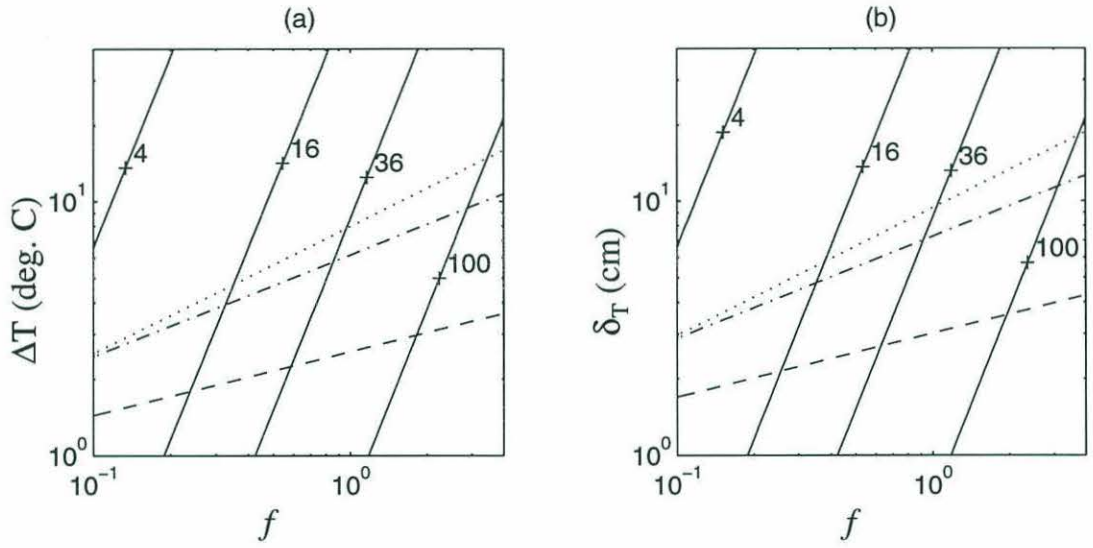

Figure 2.5: Comparison of the scaling laws in Table 2.1 in (a) the dependence of ΔT, and (b) the dependence of δ_T on f when $H = 50W$. The dashed lines are for the geostrophic scaling law, the dotted lines are for Ekman scaling law, and the dash-dotted lines are for the baroclinic eddy scaling law. The solid lines are contours of r. The scaling laws are valid when $r > O(1)$. In the calculation $l_x = l_y = 100cm$, $\kappa = 1.4 \times 10^{-3} cm^2 s^{-1}$, $\nu = 10^{-2} cm^2 s^{-1}$, $\alpha = 2 \times 10^{-4\circ} C^{-1}$, $g = 980 cms^{-2}$, $\rho_o = 1 gcm^{-3}$, and $C_p = 4.2 gJ^\circ C^{-1}$. Note that the proportionality constant is assumed "1" for each case. A proper proportionality constant can be determined thorough laboratory experiments, numerical runs, or analytical solutions.

f is systematically varied.

2.1.6 Thermocline Theory

Thermocline theories attempt to explain how surface forcing by heat and wind stress penetrates to great depths in the oceanic gyres (Pedlosky, 1987). Depending on how the vertical velocity is determined, they can be divided into two kinds; wind driven thermocline theories and classical thermocline theory. In the former, Ekman pumping at the surface specifies vertical velocity and the motion is driven by wind stress. In the latter, vertical velocity is determined internally and the motion is primarily thermally driven. The review in this section is based on Pedlosky (1987) and Huang (1995).

Classical Thermocline Theory

The classical thermocline theory in a β-plane ocean (Robinson and Stommel, 1959) is similar to the geostrophic scaling law. The linear vorticity equation in a β-plane from geostrophy

$$\beta v = f\frac{\partial w}{\partial z}$$

yields

$$\beta V \sim \frac{f_o W}{\delta_T}.$$

If we assume $T_x \sim T_y$, the meridional velocity scale V satisfies thermal wind relation Eq. 2.14. If Eq. 2.16, the balance between vertical advection and diffusion in the heat equation, is used for W

$$\delta_T \sim \left(\frac{\kappa l_y f_o^2}{\beta g \alpha \Delta T}\right)^{1/3}, \quad W \sim \left(\frac{\kappa^2 \beta g \alpha \Delta T}{l_y f_o^2}\right)^{1/3}. \tag{2.21}$$

As in the geostrophic scaling law, the horizontal advection of heat is as large as the vertical advection and the vertical diffusion. This, thus, is sometimes called the advective-diffusive thermocline theory. The vertical velocity compensates for the water mass formation in the polar region, and it is upward. In thermocline theories, the thermocline has not been

considered part of a convective circulation driven by differential heating. Meridional heat transport has not been estimated but it can be estimated easily as follows:

$$\begin{aligned} \frac{H}{l_x} &\equiv \rho_o C_p V \delta_T \Delta T \\ &\sim \rho_o C_p \left(\frac{g\alpha\kappa^2 l_y^4 \beta \Delta T^4}{f_o^2} \right)^{1/3} . \end{aligned} \tag{2.22}$$

If $\beta = f_o/l_y$ is introduced into the above equations, Eq. 2.21 and 2.22 become the same as those from the geostrophic scaling law, Eq. 2.17 and 2.20, respectively.

Robinson and Stommel (1959) derived a similarity solution of the linear vorticity equation by neglecting the zonal advection of heat and assuming special boundary conditions. (The surface temperature is independent of longitude and the east coast temperature is the same as the deep temperature.) The scale depth in their solution is the same as δ_T in Eq. 2.21. The thermocline thickens to the west and shows a maximum in the subtropics as the oceanic thermocline does. To fit the scale to the oceanic value, however, a unrealistically large vertical heat diffusion coefficient ($\kappa \approx 10 cm^2 s^{-1}$) is required.

When thermocline thickness (Eq. 2.21) and vertical velocity are estimated with canonical values from the oceans, which are $\Delta T = 20°C$, $\kappa = 0.1 cm^2 s^{-1} \sim 1 cm^2 s^{-1}$, $f_o = 10^{-4} s^{-1}$, $l = 6 \times 10^8 cm$, $g = 10^3 cm s^{-2}$ and $\alpha = 2 \times 10^{-4}\ °C^{-1}$, δ_T is in the range of 100 to $200m$ and W is in the range of 1×10^{-5} to $5 \times 10^{-5} cm s^{-1}$. These estimated values are smaller than those of the oceans, where the observed thermocline thickness is about $1000m$, and the Ekman pumping at the surface W_E is about $10^{-4} cm/sec$. Note that the estimations are based on a simple scaling argument that lacks proportionality constants.

The vertical velocity from the classical thermocline theory is internally generated by the thermal forcing and independent of the Ekman pumping. If the Ekman pumping is specified at the surface, two quantities (V and δ_T) have to be determined using three independent equations (thermal wind relation, the linear vorticity equation and the heat equation); the problem becomes overspecified. Furthermore, to obtain a boundary layer type solution with Eq. 2.16, $w > 0$. In the subtropical oceans, $W_E < 0$ so a proper solution cannot be obtained. In the subpolar oceans, $W_E > 0$ so that it is possible to include W_E by modifying w in the

deep ocean as in Robinson and Stommel (1959). The deep vertical velocity is believed to be determined by the water mass formation in the polar oceans. It is very unlikely that the deep velocity is determined by W_E at the surface. Thus, the classical thermocline theory is not compatible with the Ekman pumping.

Although the classical thermocline theory incorporates the meridional overturning circulation, it is not sufficient for the theory of the oceanic thermocline. The same problem is expected with the geostrophic scaling law when we try to apply that to the oceans. The classical thermocline theory is believed to be valid in the deep part of the oceanic thermocline below the wind driven thermocline (Welander, 1971a)

Wind Driven Thermocline

In the wind driven thermocline theory, vertical velocity is induced externally by Ekman pumping at the surface. From the thermal wind relation, the linear vorticity equation and $W = W_E$ from the Ekman pumping, we can get a new scaling for thermocline

$$\delta_T \equiv \delta_a \sim \left(\frac{W_E f_o l^2}{g\alpha \Delta T} \right)^{1/2}. \tag{2.23}$$

If we estimate thermocline thickness with the above relation when $W_E = 10^{-4} cms^{-1}$, we find $\delta_a \approx 300m$, and the estimation is better than that from the classical thermocline theory for the oceans.

If we compare the strength of vertical diffusion to advection with δ_a

$$\frac{\kappa T_{zz}}{wT_z} \sim \frac{\kappa}{W_E \delta_a} \approx 0.03 \text{ to } 0.3, \tag{2.24}$$

when κ is in the assumed range. The vertical diffusion can be neglected so that the density balance becomes advective, i.e.,

$$\vec{u} \cdot \nabla T = 0.$$

Hence, this is called the "advective" or "ideal fluid thermocline theory".

When flow enters the geostrophic region from the Ekman layer, temperature must be specified at the inflow region to determine the solution of the density equation. Thus, in

the subtropical gyres where $W_E < 0$, a purely ideal thermocline that satisfies arbitrary surface temperature distribution can exist. In the subpolar gyres where $W_E > 0$, flow leaves the geostrophic region to the Ekman layer carrying fluids whose temperature has been determined within the gyre. The temperature of the exiting fluid cannot be expected to match the arbitrary surface density.

When $W_E < 0$, we can get a diffusive length scale from Eq. 2.16

$$\delta_D \sim \frac{\kappa}{W_E}.$$

Since Eq. 2.16 cannot have a boundary layer type solution when $W_E < 0$, δ_D cannot be applicable to the subtropical gyres. The ratio of δ_D to δ_a is the same as the ratio of the vertical diffusion to the vertical advection (Eq. 2.24), which is small. The diffusive layer is so thin that no thermal wind can develop. This thin diffusive layer, where density signal decays away from the surface, intervenes between the deeper advective layer and the Ekman layer, and removes the mismatch between the surface boundary condition and the advective thermocline (Welander, 1971a; Pedlosky, 1987).

Huang (1988), however, showed all water parcels in subpolar basin come from the western boundary so the upper surface is the downstream boundary. Therefore, the density at the sea surface cannot be prescribed but should be calculated as a part of the solution. By introducing the western boundary and specifying a potential vorticity distribution, he obtained a solution for the ideal fluid thermocline in a subpolar gyre. The surface density distribution was calculated as a part of solution.

In many studies, the thermocline problem has been studied by assuming similarity solutions. Welander (1959) found a similarity solution (M-equation, integrated density function) of the ideal fluid thermocline for given surface density distribution by assuming that the deep ocean is motionless, the vertical structure depends on $(sin\theta)^{-1}$, and the horizontal structure on $sin\theta(\varphi + E(\theta))$. Here, θ means latitude, φ longitude, and $E(\varphi)$ is an arbitrary function that can be determined by boundary conditions. The vertical scale of the solution is $Csin\theta$. The constant C was considered the same as δ_T from the thermal

wind relation by considering that U and ΔT are given so $C \sim Ufly/g\alpha\Delta T$. If the Sverdrup relation is used to relate W_E to U, C becomes the same as δ_a (Eq. 2.23).

The thermocline shrinks in tropical regions as $sin\theta \to 0$, and deepens mid-latitude subtropics, as in the oceans. The solution can satisfy no flux condition across the eastern boundary. The solution, however, requires a special surface condition for the Ekman pumping velocity and density distribution. In his later paper (Welander, 1971a), the vertical diffusion of the heat was included into his M-equation. The diffusion produces a deep upwelling independent of depth. There is no interaction between the diffusion and advection so that the structure of the solution is not changed from that of the ideal fluid thermocline (Pedlosky, 1987).

Welander (1971b) assumed that the potential vorticity of an exponential similarity solution is a linear function of density and the Bernoulli function B, i.e., $f\rho_z = 2\Omega(a\rho + bB)$, where $B = p + \rho gz$, and $a = a(\theta, \phi)$ and $b = b(\theta, \phi)$ are determined through boundary conditions. The equation can satisfy an arbitrary surface density field but cannot satisfy no the flow condition along the eastern wall. He required that ρ goes to a constant for large z so the solution cannot satisfy the Ekman pumping at the surface. The thermocline rises toward the equator, and the depth of it varies as $(sin\theta)^{1/2}$ rather than as $sin\theta$ as it does in Welander (1971a).

By making an appropriate choice of the potential vorticity and specifying surface pressure on the boundaries where fluids move into (or out of) the domain, Huang (1984)'s ideal fluid thermocline solution could satisfy arbitrary surface density and Ekman pumping distributions. Pedlosky (1987) proposed that the theory is expected to apply to a finite depth interval at the surface, and the isopycnal surface bounding that region would become an unknown of the problem. The solution satisfies an arbitrary Ekman pumping at the surface, instead of the constant density condition in the deep ocean.

In Needler (1967), by assuming that the vertical structure of an exponential solution of pressure (p-equation) is $C/sin\theta$, a similarity solution that satisfies an arbitrary surface density distribution was found. Here, C is a constant that can be determined from the

distributions of the density and Ekman pumping at the surface, and the constant requires a special relation between the Ekman pumping and the surface density distribution.

No flux boundary condition across the eastern boundary requires that the surface density is the same as abyssal density on the boundary, so the thermocline thickens to the west. The dependence of the scale depth on $sin\theta$ yields mid-latitude maximum of thermocline thickness as in Welander (1959). Therefore, a realistic temperature structure could be obtained if a special choice in the surface density distribution and Ekman pumping velocity is made (Pedlosky, 1987). In his derivation, the vertical diffusion of heat was included but the only role of diffusion is to produce abyssal upwelling without altering the advective structure as in Welander (1971a). In similarity solutions the vertical structures of the solutions were assumed *a priori* and require special relations between boundary conditions. However, there is no reason that the assumed vertical structures of the solutions are relevant and valid throughout the domain of the flow.

Luyten *et al.* (1983) introduced a layered thermocline model (the ventilated thermocline theory), which does not need a similarity form and satisfies surface temperature distribution directly for the interior of the subtropical gyres excluding the western boundary region and the Ekman layer. The upper ocean, which satisfies the Sverdrup balance, is divided into several constant density layers that outcrop at different locations. Each layer satisfies the continuity, geostrophy, and linear vorticity equation. The top layer at any location is directly influenced by the Ekman pumping. The deepest layer is not influenced by the Ekman pumping at all and motionless.

Once a fluid parcel is subducted below the top layer by the surface Ekman pumping, the parcel flows southward following a trajectory determined by the conservation of potential vorticity, which is given at the outcropping location, and the Sverdrup relation. The water subducted at the eastern boundary has to leave the wall in order to conserve the potential vorticity. Thus, below the top layer there is a region called the shadow zone, which cannot be refreshed by fluid flowing from the outcrop line. Near the western boundary, there is water coming out from the western boundary region whose potential vorticity cannot be

determined by the interior model. This is called the pool zone. Even with two active layers, the ventilated thermocline theory shows a non-self similar solution that consists of three zones of different dynamics; the ventilated zone, the shadow zone and the pool zone. The ventilated thermocline theory, however, cannot explain the effect of the vertical heat diffusion on the thermocline.

If we estimate meridional heat transport with the scales from the wind driven thermocline theory

$$H = \rho_o C_p V \delta_a \Delta T l_x \approx 3 \times 10^{15} W,$$

when $W_E = 10^{-4} cms^{-1}$, $\Delta T = 20°C$, and $l_x = l_y = 6 \times 10^8 cm$. The value is comparable to the estimation using hydrographic data in the North Atlantic across $25°N$ $1.22 \times 10^{15} W$ (Bryden and Hall, 1980; Hall and Bryden, 1982). In the wind driven thermocline theory, convective processes such as water mass formation and deep upwelling cannot be included properly so that one could question the validity of the estimation using the wind driven thermocline theory.

In Bryan and Cox (1967)'s numerical experiment with thermal forcing only, a single large anti-cyclonic gyre exists above the thermocline and a sluggish cyclonic gyre below the thermocline. The meridional heat transport was about 0.3 of the prediction with the geostrophic scaling law. When surface wind stress, which can produce horizontal velocity scale about three times larger than that due to the thermal forcing, was introduced, the horizontal circulation became stronger, and a cyclonic gyre was formed in subarctic latitude. The meridional heat transport and the strength of the meridional circulation, however, did not change much. The wind stress had no apparent effect on meridional overturning circulation. The wind driven gyre was faster than the thermally driven one, but a large part of the former was simply recirculation and did not contribute to the meridional overturning circulation much. It is not hard to expect that the wind driven thermocline theory cannot represent meridional heat transport process properly, although the prediction of the thermocline thickness from the theory is comparable to the observed values.

2.1.7 Laboratory Experiments

A laboratory experiment is useful for the study of a scaling law since it does not require *a priori* assumptions or parameterizations for dynamics. It is also easier to change parameters of interest and isolate a certain phenomenon. However, due to the difficulty of heat flux measurement, most laboratory experiments on rotating convection driven by differential heating have never been used to obtain or test scaling laws related to meridional heat flux except those of Condie and Griffiths (1989).

They heated a vertical wall and cooled the opposing side walls of a rotating cavity. By measuring temperature changes across the side walls, which were consisted with copper and aluminum, they could estimate the heat transport of the experiment. The Nusselt number Nu, the ratio of the heat transport by convection to conduction, was mainly determined by the Rayleigh number ($Nu \sim Ra^{1/4}$) and weakly depended on rotation; when f was increased about 4 times, Nu was decreased by 7%. In the oceans, buoyancy is applied along the sea surface. In their experiment, the buoyancy forcing was applied through the side walls. A horizontal thermal boundary layer, which is equivalent to the thermocline of the oceans, was not observed as shown in Fig. 2.6 (from Condie, 1989). There might have been a vertical thermal boundary layer near the cold wall, but it was not possible to confirm such a layer with the results presented in their paper. An interior of uniform temperature was not observed, either. The temperature fields of the experiment was quite different from those of the oceans so that the flows and the heat transport processes of the experiment might be different from those of the oceans.

Speer and Whitehead (1988) differentially heated the copper bottom of a square tank. A horizontal thermal boundary layer and an interior with a weak temperature gradient were observed as shown in Fig. 2.7. Rising motion was confined to a narrow region near the hottest end of the bottom. A cyclonic gyre was observed in the interior that had relatively uniform temperature shows that the flow field was not two dimensional as in the analysis with an annulus. Thus, the scaling laws with a rotating annulus (the Ekman scaling law) may not be applicable to a rotating rectangular container. The study was

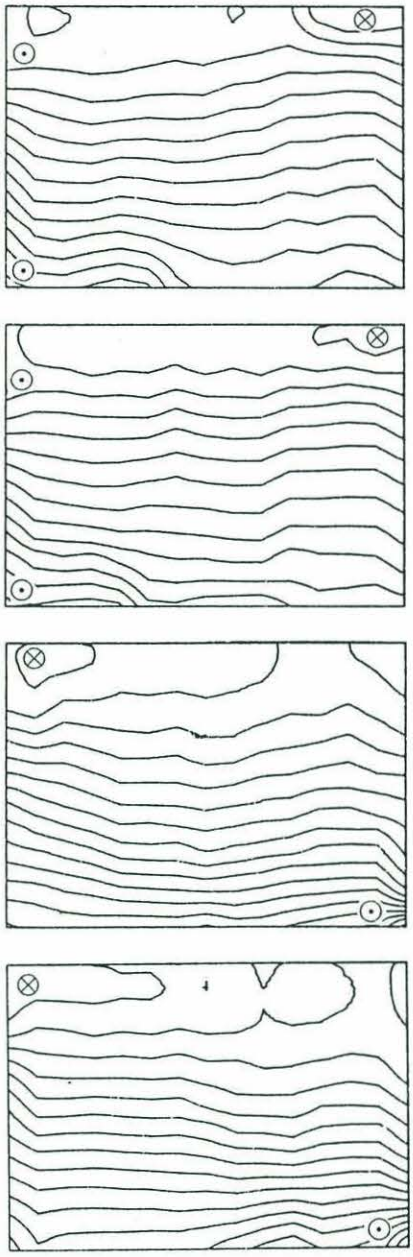

$\frac{x}{L} = 0.28$

$\frac{x}{L} = 0.43$

$\frac{x}{L} = 0.65$

$\frac{x}{L} = 0.80$

Figure 2.6: Zonal temperature sections in Condie (1989) (Fig. 1(d) in the paper) where x/L is the distance from the hot end ($x/L = 0$). The isotherms are drawn at equal intervals. No horizontal thermal boundary layer can be seen. There are fast meridional boundary currents where $\otimes$ means warm current from the warm wall to the cold wall, and $\odot$ means cold current from the cold wall to the warm wall.

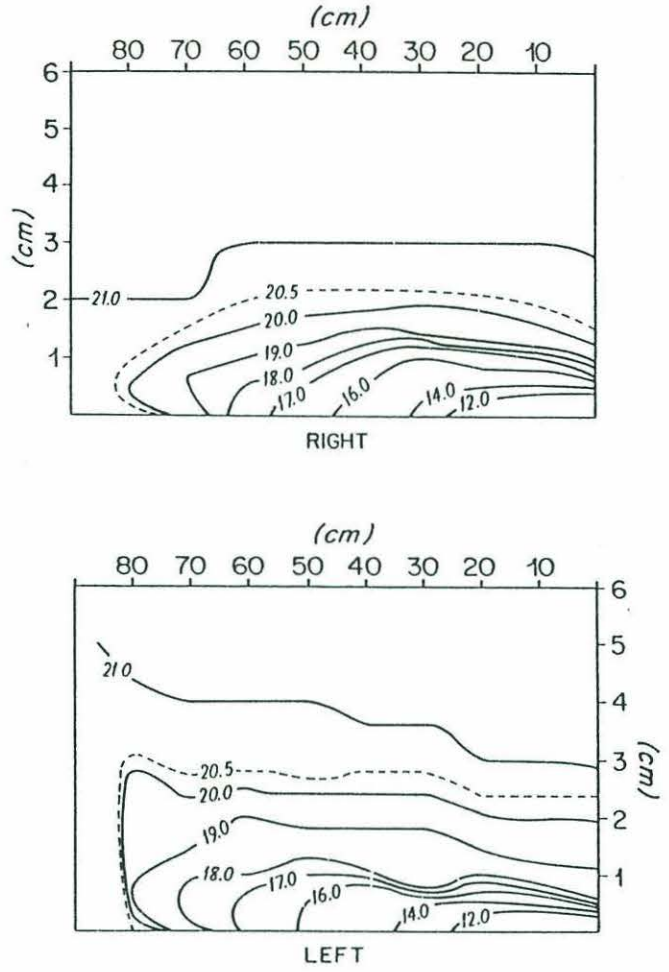

Fig. 5. Vertical sections of temperature from the hot to the cold end, located 10 cm from the left and right walls (looking from the hot end to the cold end).

Figure 2.7: Temperature sections from Speer and Whitehead (1988) (Fig. 5 in the paper). A thermal boundary layer and an interior of nearly uniform temperature can be seen. From the two figures a zonal temperature gradient, which supports a meridional geostrophic flow, can be deduced.

primarily intended for oceanic application but the results were qualitative and descriptive. The functional dependence of the structure of the flow and temperature field on external parameters was not found. Heat flux measurements were not made either.

Most of the theoretical or experimental studies described above on rotating convection were done with two dimensional flow fields and may not be applicable to the oceans. Studies with three dimensional flow fields were exploratory and were not pursued in enough detail to test any of the theories reviewed above. Numerical experiments that try to simulate the present oceans and climates would benefit from additional understanding of the dynamics and scaling laws of oceanic convective circulation.

2.2 Experiment

2.2.1 The Design

The main purpose of the experiment is to study buoyancy driven circulation in a laboratory as a model of oceanic thermohaline circulation. The primary goals were to obtain scaling laws for the meridional heat transport and for the thermal boundary layer, and to identify the flows related to the meridional heat transport. The first priority was given to simulate the effect of the meridional boundaries of the oceans, which make the large scale ocean circulations different from the atmospheric ones. To accomplish this a $100cm \times 100cm \times 20cm$ square tank was used as sketched in Fig. 2.8.

The second priority was to get a thermal boundary layer that is equivalent to the thermocline of the oceans. To accomplish this buoyancy forcing was applied along a horizontal boundary. In the oceans, the buoyancy forcing is applied along the surface of the oceans. In the experiment, differential heating was applied along the bottom for technical convenience. Thus, the experiment was equivalent to an upside-down f-plane ocean. The meridional direction of the experiment (y) is in the direction of the applied temperature gradient. The zonal direction of the experiment (x) is then the direction perpendicular to the meridional direction.

The third priority was to optimize the precision of the heat flux estimation. In previous laboratory experiments, differential heating was implemented by specifying temperature distribution along or across boundaries. Since it is difficult to measure temperature profiles right next to boundaries, heat exchange through the boundaries of the system could not be estimated easily. In this experiment, heat flux was fixed along the bottom using an electrical heater and a cooling plate along the bottom of the tank while insulating all other boundaries.

An electrical heater of $100cm \times 20.3cm$, connected to a constant voltage source, was placed at one end of the bottom of the tank. The cooling plate was a copper plate of $100cm \times 20.3cm$ and was located at the other end. The plate was cooled by running water

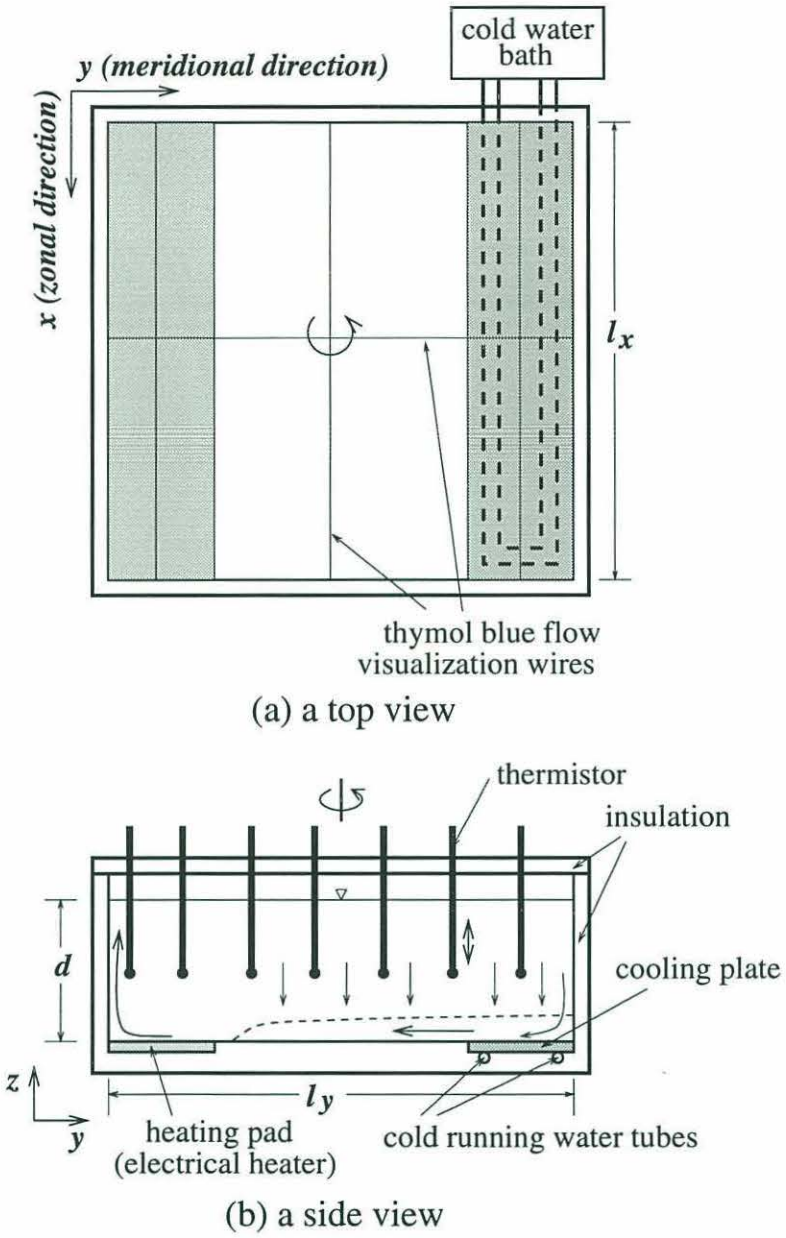

Figure 2.8: The design of the experiment. (a) a top view (b) a side view along a meridional section. The tank is $100cm \times 100cm \times 20cm$. Buoyancy forcing was applied using an electrical heater and a cooling plate along the bottom of the tank. The configuration is equivalent to an upside-down f-plane ocean with constant heat flux at the bottom.

from a constant temperature water bath through copper tubing that was soldered below the plate. A $1.3cm$ thick Plexiglas plate of $100cm \times 59cm$ was placed between the heating pad and the cooling plate to prevent any heat exchange. The four walls of the tank were made of $1.3cm$ thick Plexiglas to retard heat transfer. The outside of the tank was insulated further with $5cm$ thick Styrofoam.

If this system was left alone long enough to reach an equilibrium state, and if all the boundaries except the heating pad and the cooling plate were insulated perfectly, the same amount of heat applied by the heater H would be removed by the cooling plate. The meridional heat flux, thus, would be H within in the experimental error that was mostly due to imperfect insulation. (The detail description of the error is in the next section.) Special tests, which will be subsequently described, showed that the experiment reached the equilibrium state. It follows that the meridional heat flux was used as a known external (control) parameter.

The basic non-dimensional parameters of the experiment were

$$Rayleigh\ Number\ \ Ra = \frac{g\alpha\Delta T l_y^3}{\nu\kappa}$$

$$Ekman\ Number\ \ E = \frac{\nu}{fd^2}$$

$$Thermal\ Rossby\ Number\ \ R_T = \frac{g\alpha\Delta T d}{f^2 l_y^2}\left(= \frac{V_g}{f l_y}\right)$$

$$Prandtl\ Number\ \ Pr = \frac{\nu}{\kappa}$$

$$Aspect\ Ratio\ \ \varepsilon = \frac{d}{l_y}$$

$$Horizontal\ Aspect\ Ratio\ \ \varepsilon_h = \frac{l_x}{l_y}$$

Here, g is gravitational acceleration, ΔT is a meridional temperature difference across the tank, α is the thermal expansion coefficient, κ is the thermal diffusivity, ν is the kinematic viscosity of water, and f is the Coriolis parameter, d is the depth and l_y is the length and l_x is the width of the tank. Since a square tank was used, the width is the same as the length and $\varepsilon_h = 1$. Water was used as a test fluid so $Pr \approx 7$ throughout the experiments. The water depth was $12cm$ throughout the experiment so $\varepsilon = 0.12$.

The thermal Rossby number is the same as the Rossby number if velocity estimation from the thermal wind relation $V_g = g\alpha\Delta T d/fl_y$ is considered. In most cases, $R_T \ll 0.1$ so that the non-linear effects were small compared to the Coriolis effect. Since heat flux H was fixed, ΔT was not an external parameter, but a value to be determined through the experiments. The heat loss through the cooling plate, $\rho_o C_p \kappa T_z$, was the same as the heat input by the heating pad, H, so $\Delta T = Hd/\kappa\rho_o C_p$. This relation was used to get a rough idea of the parameters during the early stages of the experiments. After obtaining ΔT from the experiments, the above definitions of Ra and R_T were used.

The main parameters of interest in this experiment were Ra and E. The variation in Ra was obtained by changing boundary heat flux H, which varied from $20watts$ to $400watts$. The upper limit of Ra was set by the endurance of the tank against heat. If $H > 400watts$ the water became hotter than 50°C and the Plexiglas tank would deform. The maximum value of Ra was about 3×10^{11}, and Ra was varied by about 20. In the experiment, Ra is several orders of magnitude larger than those obtained by any numerical experiment or previous laboratory experiments, but it is still much smaller than those of the oceans. In the oceans, $Ra \approx 8.6 \times 10^{26}$ when $\Delta T \approx 20°C$, $d = 5000m$, $l_y = 6 \times 10^6 m$, $\kappa = 10^{-4} m^2 s^{-1}$, and $\nu = 10^{-4} m^2 s^{-1}$.

The variation of E was obtained by changing f, which was varied from $0.25s^{-1}$ to $1.25s^{-1}$. A few runs were done with $0 \leq f < 0.25s^{-1}$ for comparison. The lower limit in E (the upper limit of f) was determined in such a way that the surface elevation change due to the centrifugal force was less than 5% of the still water depth. The typical value of E was around 10^{-4} and E was varied by about 12.

There are two other parameters that are related to Ra and E, and more clearly indicate the importance of the rotation or balance in a thermal boundary layer (Hignett *et al.*, 1981). One is a thermal boundary layer thickness related to the strength of buoyancy forcing. For this, one can use the thermal boundary layer thickness of a non-rotating system $\delta_{T_n} = l_y Ra^{-1/5}$ (Rossby, 1965), where the subscript 'n' means a non-rotating system. The other, which represents the strength of rotation, is the Ekman layer thickness in a

homogeneous fluid $\delta_E = dE^{1/2}$. The square of the ratio between the two depth scales

$$r = \left(\frac{\delta_{T_n}}{\delta_E}\right)^2 \sim \Delta T^{-2/5} f$$

represents the importance of rotation in convection (Hignett *et al.*, 1981).

When $r > O(1)$ (Fig. 2.9(a)), a thermal boundary layer is far thicker than the Ekman layer; rotation is important within the thermal boundary layer (geostrophic balance within a thermal boundary layer). When $r < O(1)$, the Ekman layer is thicker than a thermal boundary layer (Fig. 2.9(b)); frictional dissipation is important within a thermal boundary layer. In the oceans, the Ekman layer is $O(100m)$ deep (using an empirical turbulent viscosity), but the thermocline is about $1000m$. The thermal boundary layer of the experiment should be thicker than the Ekman layer so that geostrophy is maintained within the thermal boundary layer. Both Ra and E were varied independently to get $r > O(1)$ and most of the runs were done with this range.

2.2.2 Procedure

Spin Up The tank was placed on the $2m$ diameter rotating table in the GFD laboratory, Coastal Research Center, WHOI, and filled with water to $12cm$ deep. The table, the heating pad, and the cooling plate were then turned on. The spin up time for a homogeneous water is $O((\nu f)^{-0.5} d)$, which was less than an hour in this experiment. The time required to raise the temperature of a water of volume V by $\Delta T°C$ using a heater of $Hwatts$ is $\rho_o C_p \Delta T V/H$. Some trial runs showed that $\Delta T/H \approx 0.1°C/watts$, and $V \approx 10^5 cm^3$. The heat up time was about $15hours$. At the same time, there was heat loss through the cooling plate, so it took more time to reach a thermal equilibrium state. After some trial runs, it was possible to know how long it would take to attain equilibrium temperature and what the equilibrium temperature would be. The tank was filled with water a few degrees lower than the expected equilibrium temperature in order to reach an equilibrium state faster. The water was spun up at least 40 hours before temperature sections were made.

To satisfy the flux boundary condition, a run should reach an equilibrium state. It was important to have a clear criterion on a thermal equilibrium state. During the spin

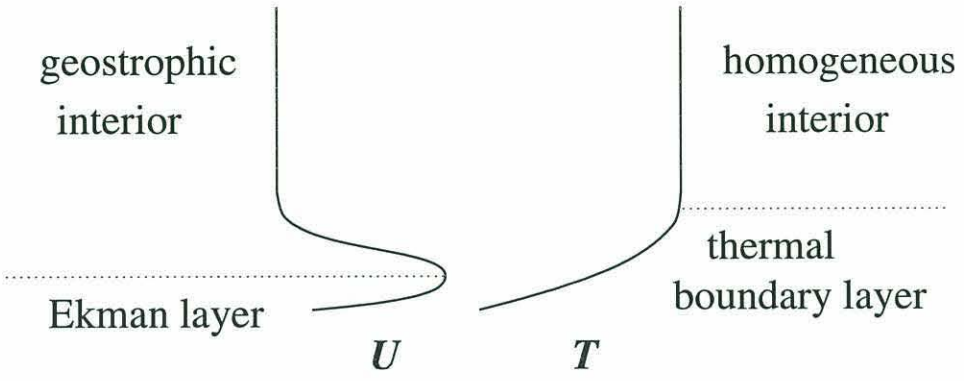

(a) $r >$ O(1)

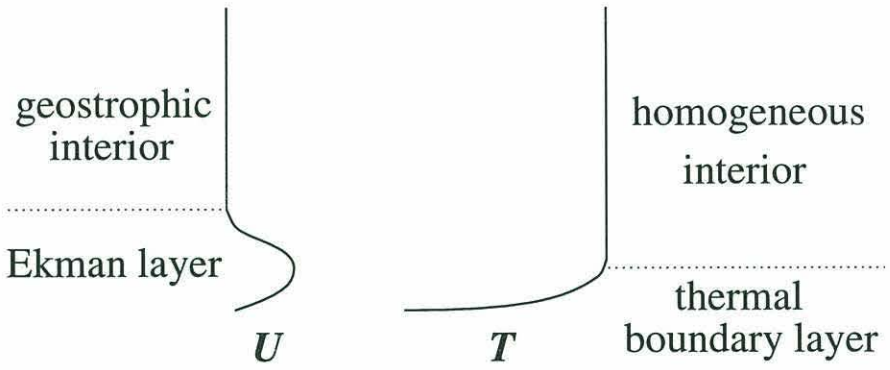

(b) $r <$ O(1)

Figure 2.9: A diagram for the Ekman layer and a thermal boundary layer when (a) $r > O(1)$ and (b) $r < O(1)$. In (a) rotational effect is dominant within the thermal boundary layer. In (b), frictional effect is dominant within the thermal boundary layer.

up, two thermistors were placed on the bottom at $(x, y) = (50cm, 2cm)$ and $(50cm, 98cm)$. In Fig. 2.10(a) and (c), which are typical temperature measurements during the spin up, the temperature changes rapidly right after the beginning of the run, but the change becomes smaller with time. After about 35 hours of spin up, there is no mean trend in the temperature curve. This suggests that the temperature field reached an equilibrium state. Fig. 2.10(b), which is a blow up of the equilibrium state in Fig. 2.10(a), shows some spikes. Considering the active convective motions over the heating pad, those spikes are natural. Fig. 2.10(d), which is a blow up of the equilibrium state in Fig. 2.10(c), shows constant readings relative to those over the heating region. Right over the cooling plate, heat leaves the water by diffusion and motion should be weak, so the temperature should be rather constant. The flat readings also suggest that the drift of the thermistors over time was negligible.

Measurement Temperature sections were made after the hourly average of the readings with the two thermistors changed less than $0.1°C$. The temperature was measured with thermistors of $\pm 0.1°C$ accuracy at 7 to 13 levels with at least 15 locations on each level at each section. Near the bottom about 100 readings and in the interior 50 readings were made at each location and then averaged to remove the variation due to thermals and waves. The thermistors were connected to a data logger, which was in turn linked to a portable computer. The readings, which were the resistance of the thermistors, were stored in the computer and converted to temperature later.

The thermistor array, which was mounted to a rack, was lowered to the bottom of the tank through a narrow slot in the $5cm$ thick Styrofoam cover, which was opened during the measurement. The slot was about $1mm$ wide in most cases so that the heat loss through it was not significantly larger than that due to the imperfect insulation of the tank. After leaving them in that location for a few minutes so that they equilibrated to the ambient water temperature, readings were made. The array was then lifted by a fixed distance using a stepper motor, and then temperature was again measured. This procedure was continued

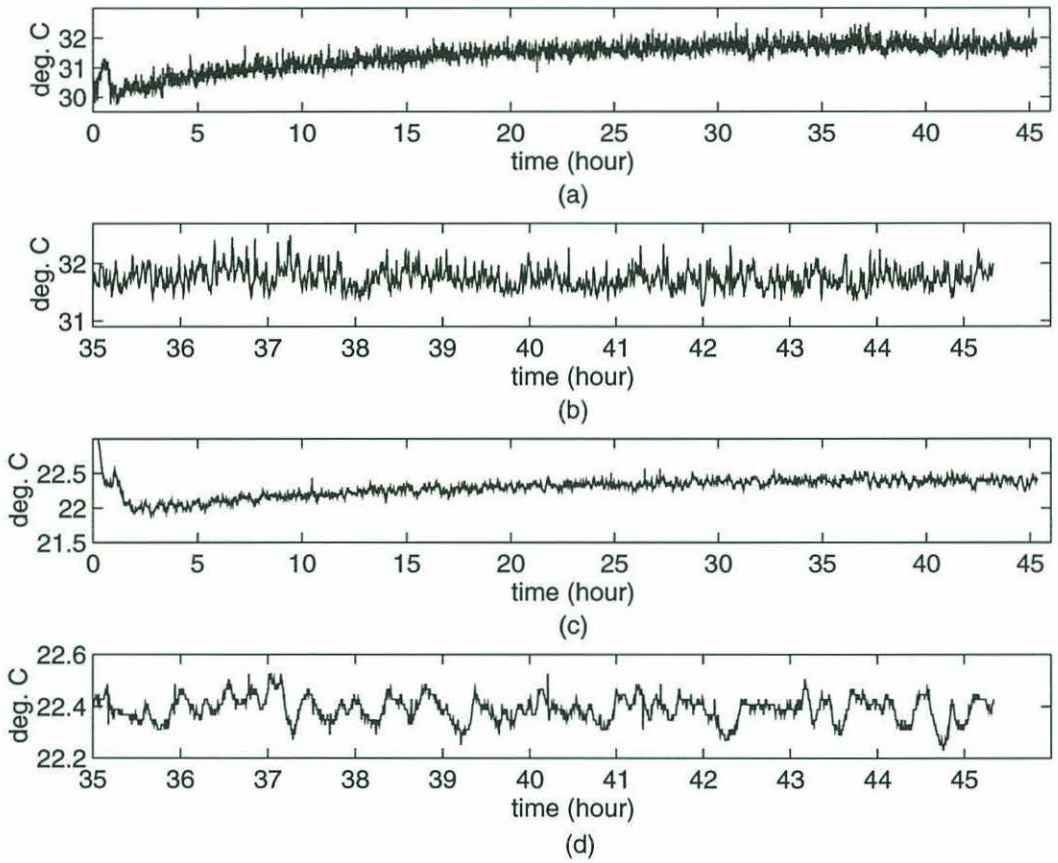

Figure 2.10: Temperature change during spin up when H=100W, $f = 1.25s^{-1}$ ($Ra = 9.3 \times 10^{11}$, $E = 5.6 \times 10^{-5}$) (a) over the heating pad, (b) blow up of (a) when an equilibrium state was reached, (c) over the cooling plate and (d) blow up of (c) when an equilibrium was reached. The measurements were made every 20sec.

until the thermistors reached near the surface of the water. Three meridional sections were made for each parameter in most cases; $10cm$ away from the left and right meridional boundaries and one at the center ($x = 10cm,\ 50cm,\ 90cm$). Zonal sections were made for selected parameters at selected locations to identify heat carrying flows, and to infer flow patterns. It took about two to three hours to complete a section. To remove disturbances that might have occurred during the measurement, the experiment was left at least four hours before making another section. Including the spin-up time, a run took about three to four days.

Flow visualization was done using the thymol blue technique. A stack of two grids was used as electrodes. Each grid consisted of one or more meridional, and three or more zonal wires of $0.16mm$ diameter stainless steel rod. One grid was placed $1cm$ above the bottom so it was within the thermal boundary layer but above the Ekman layer. The other one was placed $7cm$ above the bottom to be in an interior of homogeneous temperature.

Correction, Error Estimation and Instrument Calibration The largest source of error was heat loss through the boundaries of the tank owing to imperfect insulation. The actual heat loss was estimated as follows. The tank was filled with hot water and left alone. Since no heating or cooling was applied, temperature change was solely due to the imperfect insulation. By measuring the change in water temperature for a certain period of time, we could estimate the heat loss. During the measurement, the water was mixed to make the water homogeneous. The ratio of the heat loss to the temperature difference between the water and the laboratory was about $3watts^{\circ}C^{-1}$.

The conductive heat loss through the Styrofoam insulation could also be estimated using the heat conduction coefficient of Styrofoam $\rho_S C_{pS} \kappa_S = 3 \times 10^{-4} Jcm^{-1}\ s^{-1}\ ^{\circ}C^{-1}$ as follows:

$$(\rho_S C_{pS} \kappa_S / 5cm) \times \text{surface area of the tank} = 1.2watts^{\circ}C^{-1}. \tag{2.25}$$

To allow access to the water, the cover of the tank was placed over the walls of the tank. Thus, the contact between the cover and the walls was not air-tight so warm air could escape

from the tank to the laboratory in addition to the evaporation through the thermistor insertion slots. The remaining $1.8 watts^{\circ}C^{-1}$ must be from heat loss due to evaporation.

The heat loss was always from the water to the environment so that the upper bound of the meridional heat transport H_U

$$H_U = H_{heating\ pad}.$$

The lower bound of the meridional heat tranport H_L

$$H_L = H_{heating\ pad} - (T_{water} - T_{lab}) 3.0 watts^{\circ}C^{-1}.$$

The mean of H_U and H_L can considered as the actual (corrected) meridional heat transport H of the experiment. Thus,

$$H \equiv H_{heating\ pad} - (T_{water} - T_{lab}) 1.5 watts^{\circ}C^{-1}. \tag{2.26}$$

Here, T_{lab} is the temperature of the laboratory, which was set to $20^{\circ}C \pm 1^{\circ}C$ using a laboratory-wide temperature and humidity controller. Thus, T_{lab} can considered the same as the temperature of the cold water bath $T_B = 20^{\circ}C$. It was assumed that the water in the tank was homogeneous and the temperature was T_{water}. If the thermal boundary layer of the experiment is excluded, water temperature shows very little spatial change, so T_{water} could be considered as the highest temperature measured through a run. The typical uncertainty in H due to H_U and H_L is about 20%. Hereafter, H or meridional heat flux means the corrected value using Eq. 2.26 and H_N or nominal heat flux means $H_{heating\ pad}$.

All the thermistors were calibrated using a constant temperature water bath. Readings were made at four different temperatures and correction coefficients were obtained for each thermistors. The error due to the thermistors, $\pm 0.1^{\circ}C$, was small compared to the one caused by imperfect insulation, and therefore was considered negligible. The thermistor array was moved vertically by a stepper motor so the uncertainty in vertical position was far less than $1mm$. Horizontal position was, however, determined manually so the uncertainty in horizontal position was $\pm 5mm$ or less.

Parameters of the Experiment Various parameters of the experiments are listed in Table 2.2. In the table H is estimated using Eq. 2.26. Although the nominal heat flux H_N is fixed, as the rotation becomes faster, ΔT increases; the heat loss due to the imperfect insulation becomes larger so that H decreases slightly.

In Fig. 2.11, the runs are plotted in (E, Ra) space. The dashed lines in the figure represent contours of $r = (\delta_{T_n}/\delta_E)^2$, which represents the dynamic balance in a thermal boundary layer. In the direction of the upper right corner, the Ekman layer becomes thicker and r decreases so a frictionally balanced thermal boundary layer was obtained. In the direction of the lower left corner, r increases and the Ekman layer gets thinner so we could get a geostrophically balanced thermal boundary layer, which is suitable for oceanic application. Smaller H and greater f gave higher r, which was felt to be desirable, so in most runs $r > 10$. The runs with $r < 10$ were for comparison.

Table 2.2: Parameters of the experiments. From the experimental results, ΔT (see Section 2.3.1) and δ_T (see Section 2.3.2) are obtained.

$f\ (sec^{-1})$	$H_N\ (watts)$	$H\ (watts)$	$\Delta T\ (°C)$	$\delta_T\ (cm)$
0.25	20	15	3.6	3.2
0.63	20	14	3.8	3.5
1.25	20	14	4.2	4.5
0.00	50	43	4.7	1.4
0.25	50	40	6.4	2.2
0.32	50	40	6.4	2.7
0.45	50	40	6.6	2.7
0.63	50	40	7.0	3.3
1.00	50	39	7.3	3.4
1.25	50	39	7.5	3.5
0.25	100	86	9.7	1.7
0.32	100	84	10.8	2.0
0.45	100	83	11.5	2.3
0.63	100	82	11.8	2.4
1.00	100	81	12.4	2.6
1.25	100	81	13.0	2.8
0.00	200	178	14.5	-
0.06	200	178	14.8	-
0.08	200	178	14.9	-
0.13	200	176	15.8	-
0.18	200	176	15.9	-
0.25	200	177	15.5	1.3
0.32	200	175	16.6	1.1
0.54	200	174	17.4	1.6
0.63	200	173	18.2	1.6
1.00	200	171	18.9	2.5
1.25	200	170	19.8	2.5
0.25	300	271	19.5	-
0.63	300	268	21.6	-
1.25	300	266	22.7	-
0.25	400	361	26.2	-

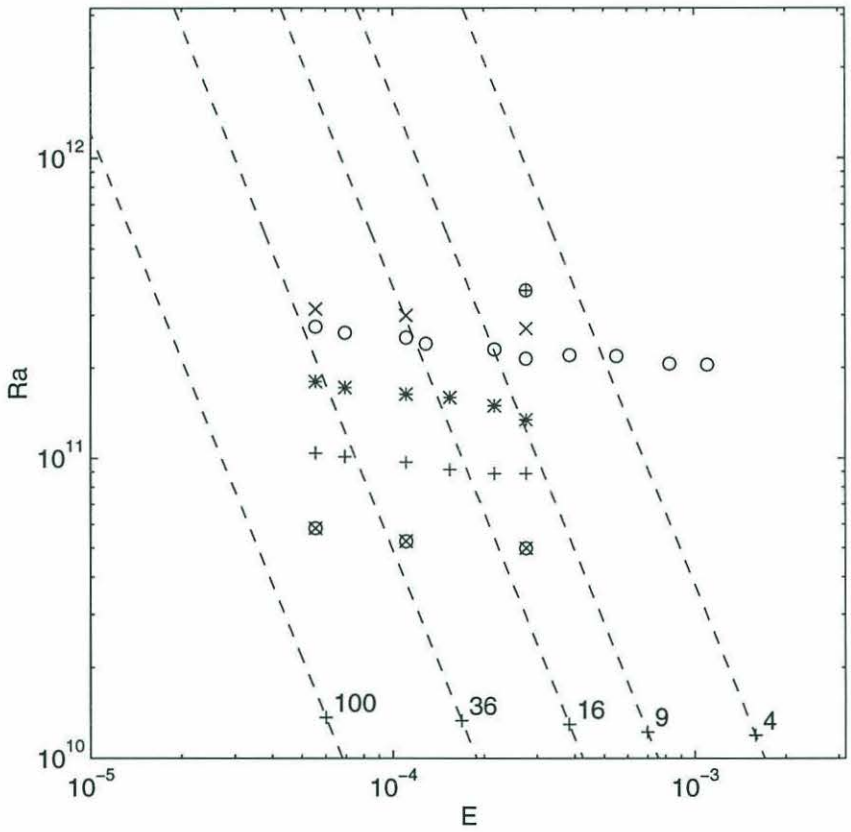

Figure 2.11: Experimental parameters in $(Ra,\ E)$ space. The dashed lines are the contours of r. Here, $\otimes$ is for $H_N = 20W$, $+$ is for $H_N = 50W$, $*$ is for $H_N = 100W$, $\circ$ is for $H_N = 200W$, $\times$ is for $H_N = 300W$, and $\oplus$ is for $H_N = 400W$.

2.3 Results

2.3.1 Meridional Temperature Sections

The meridional temperature distribution is qualitatively similar to that of Rossby (1965), as shown by a comparison between Fig. 2.12, which has typical meridional temperature sections, and Fig. 2.1. A thin thermal boundary layer extended from the cold end toward the hot end along the bottom of the tank. A rising region, where stratification was zero, or close to zero, was confined to a small region near the hot end. The interior temperature was uniform and close to that of the rising region.

From the meridional temperature sections, ΔT, the temperature difference between the heating pad and the cooling plate, T_B, was estimated. Sometimes the hottest temperature was measured not at the bottom but in the interior. Temperature was measured at discrete locations so it was possible to miss the hottest point. The temperature difference between the hottest water observed in the interior and the water near the heating pad was small, however. Since there was no other source of the heat than the heating pad, the highest temperature measured, irrespective of the location, was considered the temperature of the heating pad. The heat conductivity of the cooling plate, which was 0.32mm thick copper plate, was high so that the estimated temperature change across the plate was less than the accuracy of a thermistor $0.1°C$. The temperature of the cold water bath was effectively the same as T_B so

$$\Delta T = T_{max} - T_B.$$

In the thermal boundary layer with thickness of about $2cm$, temperature changed very rapidly so that it was not possible to resolve it with $2mm$ diameter thermistors, especially right near the bottom. The thermistor readings were a weighted average of temperature over $2mm$, so the readings within a thermal boundary layer must have been higher than the actual temperature. It, however, turned out that the measurements were adequate for the estimation of a thermal boundary layer thickness as shown in Section 2.3.3. In the rising region or in the interior away from the thermal boundary layer, the temperature gradient

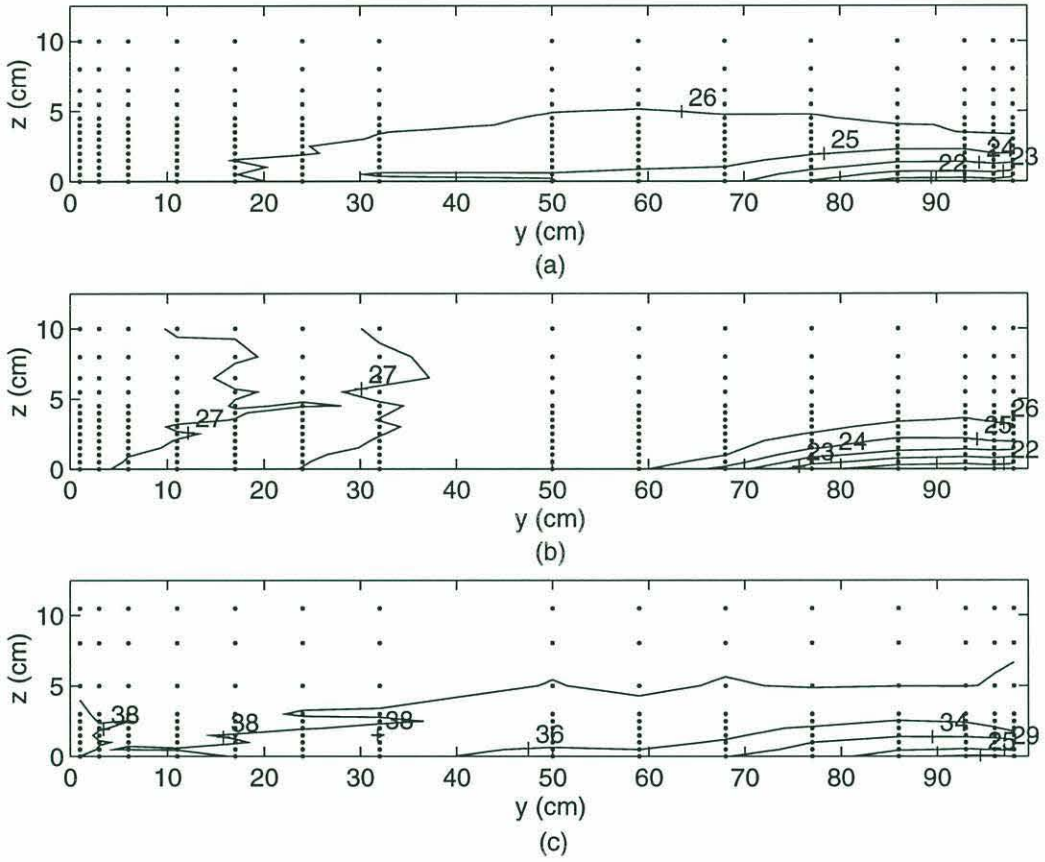

Figure 2.12: Meridional temperature sections at $x = 50cm$ with (a)$f = 0.63s^{-1}$ and $H_N = 50W$ ($Ra = 5.0\times10^{11}$, $E = 1.1\times10^{-4}$), (b) $f = 1s^{-1}$ and $H_N = 50W$ ($Ra = 5.2\times10^{11}$, $E = 6.9 \times 10^{-5}$), and (c) $f = 1s^{-1}$ and $H_N = 200W$ ($Ra = 1.4 \times 10^{12}$, $E = 6.9 \times 10^{-5}$). The meridional wall to the left when looking toward the cold end was at $x = 0cm$ and is equivalent to the eastern boundary of the oceans. The dots indicate the location of temperature measurements. The heating plate was $0cm \leq y \leq 20.3cm$ and the cooling plate was $79.7cm \leq y \leq 100cm$.

was small, so there was no difficulty of using the thermistors.

When Figs. 2.12(a) and(b) are compared, the interior temperature increases as f increases, although H_N is fixed. As f increases, vertical motion becomes more difficult and convective circulation becomes weaker. The water over the heating pad was exposed to the heat from the heating pad more before it filled the interior so that the interior temperature became higher. A run with higher H_N shows obviously higher interior temperature as the comparison between Fig. 2.12(b) and (c) shows.

2.3.2 Vertical Profile

Normalized vertical temperature profiles at $(x, y) = (49.5, 96)cm$ are shown in Fig. 2.13. Considering the size of the thermistors, the position of the center of the probes was considered the depth of the measurement. A solid line is the least square fit of a temperature profile to an exponential function, $1 - e^{-h/a_1}$, where h is height, and a_1 is a constant which minimizes the residual between the fit and the data. The constant a_1 for each case is comparable to the scale of the thermal boundary layer thickness, which is described in Section 2.3.4. The overestimation of temperature due to the large vertical temperature gradient near the bottom can be seen clearly; at $h = 1.5mm$, the measurement is significantly higher than the fit. When the vertical temperature gradient is small, one can get a better temperature profile so that the fit becomes better as h increases.

The results discussed in Section 2.3.4 suggest that the advective-diffusive heat balance was satisfied in the experiment. The advective-diffusive heat balance and the exponential temperature profile suggest that the vertical velocity profile also satisfies the same exponential form as in the classical thermocline theory by Robinson and Stommel (1959). The exponential form, furthermore, can satisfy no flow condition at the bottom. The vertical velocity profile of the experiment could be obtained, however.

Runs with higher H_N and lower f showed thinner thermal boundary layers. Higher heat input to the fluid causes a faster vertical overturning cell as a response to the increased buoyancy. A faster overturning cell brings more heat to a thermal boundary layer through

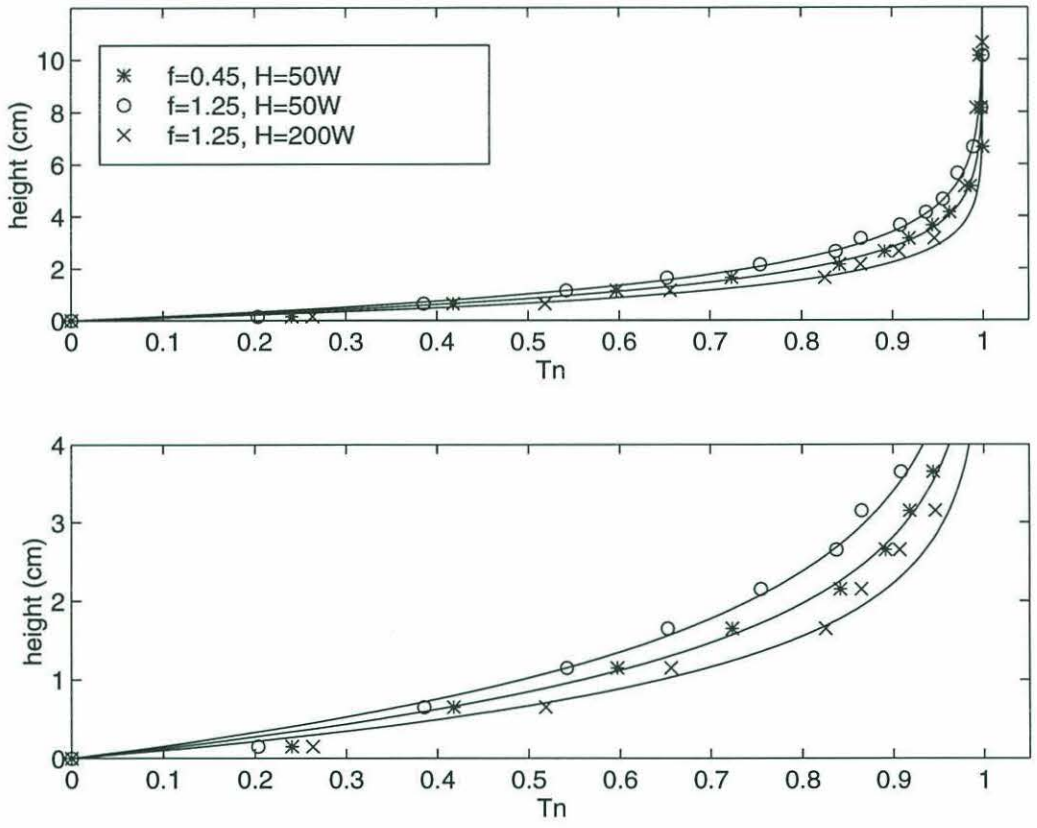

Figure 2.13: Normalized temperature profiles at $(x, y) = (49.5, 96)cm$ for selected parameters. (b) is blow up of (a). A solid curve is the least square fit of a profile to an exponential function.

vertical advection. Consequently, the diffusive heat loss through the thermal boundary layer should be intensified so that the thermal boundary layer becomes thinner. If we use a scaling argument, the heat equation ($wT_z \approx kT_{zz}$) gives $\delta_T \sim \kappa W^{-1}$. A faster overturning cell, which occurs when f is smaller, pushes a thermal boundary layer toward the bottom and gives a thinner thermal boundary layer. This argument is consistent with the relation between the heat transport efficiency and the thermal boundary layer thickness (in Section 2.1.5); when convective overturning becomes faster, the meridional heat transport becomes greater and the thermal boundary layer becomes thicker. In the experiment, for fixed H_N, as f became faster, ΔT became higher. The meridional heat transport processes became less efficient so that the thermal boundary layer became thicker (Fig. 2.13).

2.3.3 Scaling Law

Meridional Heat Transport

In Fig. 2.14, f versus ΔT for $H_N = 50W$ is shown along with the three scaling laws discussed earlier. To see the power dependence, a log-log plot was used. An appropriate $O(1)$ proportionality constant was applied to each case to make the comparison easier. The proportionality constants are about 3 for the geostrophic scaling law, 1.1 for the Ekman scaling law, and 1.3 for the baroclinic eddy scaling law.

The comparison can be made in an (H, ΔT) phase space, instead, to study the power dependence of ΔT on H. As can be seen in Table 2.1, the power dependence with the geostrophic scaling law is 3/4, with the Ekman scaling law, 2/3, and with the baroclinic eddy scaling law, 7/10. The three values are so close that it may not be possible to differentiate them with 20% uncertainty in H. In fact, the mean power dependence of ΔT on H is about 0.61 as can be seen in Table 2.3. It is close to that of the Ekman scaling law but is not significantly different from those of other scaling laws.

In Table 2.4, the power dependence of ΔT on f using the linear least squares fit for fixed H_N with the runs of $r > 10$ is listed. Although H_N is fixed, H varies so $\Delta T \sim H^{0.61}$ is assumed in the calculation. If the correction to H_N is neglected, i.e. H is considered

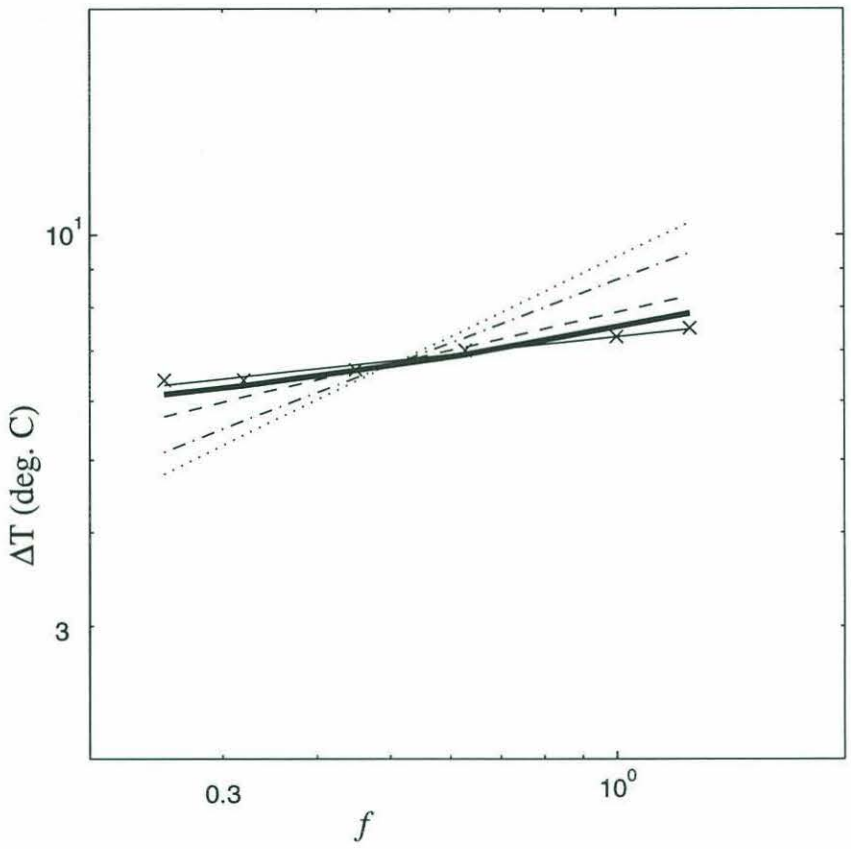

Figure 2.14: ΔT versus f when $H_N = 50W$. The experimental results are shown using '×'. The solid line (slope=0.12) is the least squares fit to the data. The dashed line (slope=1/4) is for the geostrophic scaling law. The dotted line (slope=1/2) is for the Ekman scaling law. The dash-dotted line (slope=2/5) is for the baroclinic eddy scaling law. The thick solid line (mean slope=0.17) is for the corrected scaling law discussed in Section 2.3.4. An appropriate proportionality constant was applied to each case to fit the scaling laws to the data.

Table 2.3: The power dependence of ΔT on H using linear least squares fit for fixed f. Residual is the root mean square of normalized difference between the measurement and the estimation using the fit.

$f(s^{-1})$	0.25	0.32	0.63	1.00	1.25	mean
power	0.58	0.65	0.60	0.64	0.59	0.61
residual	0.023	0.044	0.074	0.055	0.10	0.059

Table 2.4: The power dependence of ΔT on f using the linear least squares fit solution for fixed H_N.

$H_N(W)$	20	50	100	200	300	mean
power	0.12	0.12	0.18	0.15	0.10	0.13
residual	0.023	0.013	0.038	0.024	0.021	0.024

constant, the power dependence decreases by about 10%. As seen in Table 2.1, the power dependence of ΔT on f with the Ekman scaling law is $1/2$ and the one of the baroclinic eddy scaling law is $2/5$; the values are about 3.5 to 4 times as large as the mean slope of the experimental result. The geostrophic scaling law shows the weakest power dependence, which is $1/4$, but that value is also significantly larger than the mean slope of the constant H branches of the experiment, which is 0.13. Although the geostrophic scaling law is better than the others, the difference is too large to be attributed to experimental uncertainty or error.

A Thermal Boundary Layer

The thickness of a thermal boundary layer, δ_T, was estimated using temperature profiles at $(x, y) = (49.5, 96)cm$ as in Figure 2.13. The top of a boundary layer was defined as the depth at which $T_n = 0.9$. The resolution of the profile was not high enough to make accurate enough estimation of e-folding scale ($T_n = 0.63$). When $T_n > 0.9$, the temperature gradient was so tiny that small uncertainty in temperature can cause large error in the estimation. The thickness was measured with a ruler from the profiles with a $5mm$ resolution at best, thus a typical error was about $\pm 2.5mm$. As H was increased, the thermal boundary layer

Table 2.5: The power dependence of δ_T on f using linear least squares fit for fixed H_N.

$H_N(W)$	20	50	100	200	mean
power	0.20	0.29	0.27	0.50	0.32
residual	0.04	0.04	0.03	0.05	0.04

became thinner. The resolution became poorer and the error increased.

In Fig. 2.15, the results for $H_N = 50W$ are shown in an (f, δ_T) space with the scaling laws. Appropriate proportionality constants were applied to the scaling laws to make the comparison easier. As can be seen in Table 2.1, the power dependence of δ_T on H is $-1/4$ for the geostrophic scaling law, $-1/3$ for the Ekman scaling law and $-3/10$ for the baroclinic eddy scaling law. The mean power dependence of δ_T on H in the experiment from the least squares fit is -0.25. It is close to that of the geostrophic scaling law but considering the uncertainty in δ_T, the power dependence is not significantly different from those of other scaling laws. The power dependence of δ_T on f is $1/4$ for the geostrophic scaling law, which is the slope of the dashed line in Fig. 2.15, $1/2$ for the Ekman scaling law, which is the slope of the dotted line in the figure, and $2/5$ for the baroclinic eddy scaling law, which is the slope of the dashed-dotted line of the figure. It is easier to differentiate those three scaling laws in an (f, δ_T) space than an (H, δ_T) space.

In the figure, the geostrophic scaling is better than the others. The slope of the least squares fit line is close to the power law of the geostrophic scaling law. In Table 2.5, the power dependence of δ_T on f using the linear least squares fit for fixed H_N is presented. In the runs with $H_N > 200W$, the thermal boundary layers were so thin that useful results could not be obtained, and they were excluded. The mean power dependence of δ_T on f is 0.32, so it is similar to that of the geostrophic scaling law or the baroclinic eddy scaling law. If the results with $H_N = 200W$, in which $\delta_T < 2cm$ so that the error was large, are excluded, the mean power dependence becomes similar to that of the geostrophic scaling law, $1/4$.

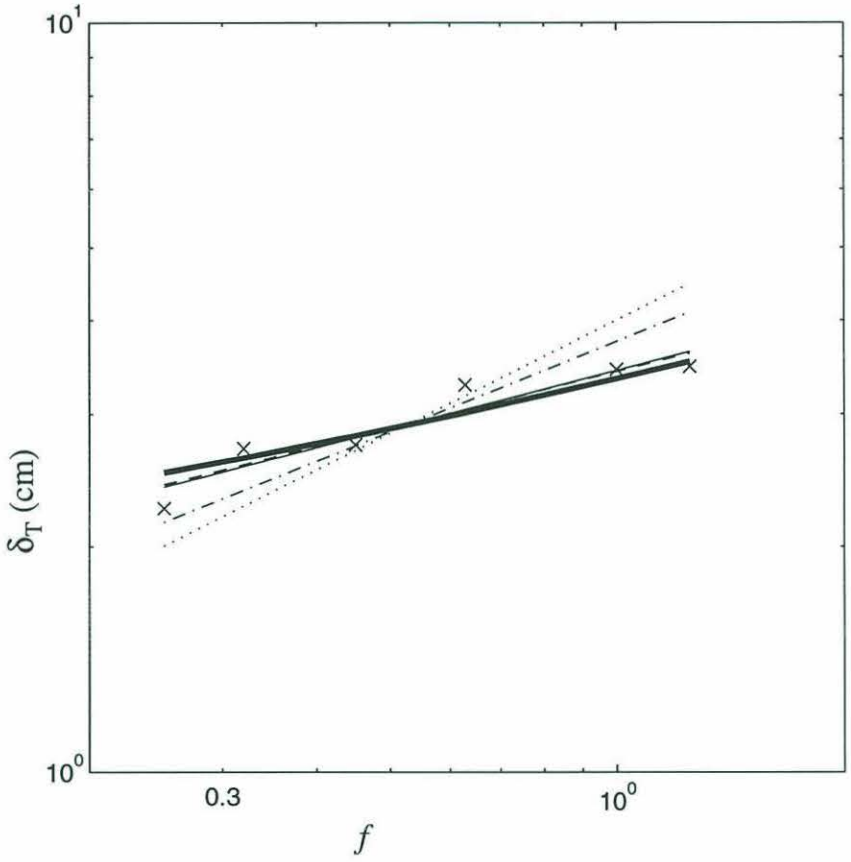

Figure 2.15: δ_T versus f when $H_N = 50W$. The experimental results are shown using '$\times$'. The solid line (slope=0.29) is the least squares fit to the data. The dashed line (slope=1/4) is for the geostrophic scaling law. The dotted line (slope=1/2) is for the Ekman scaling law. The dash-dotted line (slope=2/5) is for the baroclinic eddy scaling law. The thick solid line is for the corrected scaling law discussed in the next section. Note that appropriate proportionality constants are applied to each scaling law to make the comparison easy.

2.3.4 A Corrected Scaling Law

The preliminary comparison between the experimental results and the scaling laws suggests that the geostrophic law compares better with the results than others. The difference between the geostrophic law and the results, however, is too large to be considered as an experimental error or uncertainty. The geostrophic scaling law does not allow any frictional effects. In the experiment, however, there was always a frictional Ekman layer at the bottom. A correction to the geostrophic scaling law due to the bottom Ekman layer can be made if the thermal boundary layer of the experiment was thicker than the Ekman layer, which was satisfied by the experiments.

The Ekman layer would reduce heat transport efficiency in two ways. First, the Ekman layer retarded the meridional geostrophic flow. It reduced the meridional mass and consequently heat transports. Second, there might be a temperature drop across the Ekman layer (assumed negligible in Hignett *et al.*, 1981). The buoyancy forcing driving the geostrophic flow was weaker than that along the bottom. The role of the Ekman layer in the experiment is opposite to that in the Ekman scaling law, in which all the meridional mass and heat fluxes are solely due to the Ekman flux in the Ekman layer.

The reduced heat transport efficiency requires a thicker thermal boundary layer or higher thermal forcing to maintain the same amount of meridional heat transport. As f decreases, the Ekman layer thickens so that the effects become larger; the power dependence of ΔT on f decreases.

The geostrophic flow away from the Ekman layer is assumed to be driven by T_G

$$\Delta T_G = \Delta T - \Delta T_F.$$

As sketched in Fig. 2.16, ΔT_F is the temperature drop across the Ekman layer. Temperature profile is exponential (Fig. 2.13) so

$$T = T_I - (T_I - T_B)\exp(-z/\delta_T).$$

Here, T_I is interior temperature, T_B is the temperature of the cooling plate. From the above

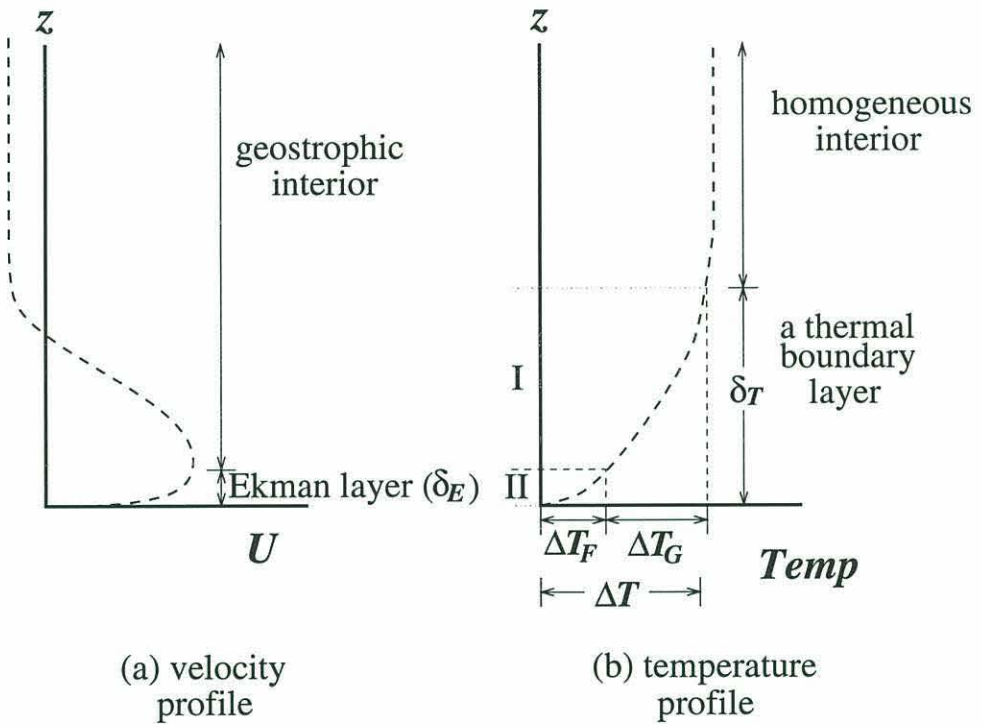

Figure 2.16: Schematic profiles of (a) velocity and (b) temperature.

temperature distribution, we can define

$$\Delta T_F = T_I - T(\delta_E), \quad \text{and}$$

$$\Delta T_G = \Delta T \exp(-\delta_E/\delta_T).$$

Here, $\Delta T = T_I - T_B$ and $\delta_E = (2\nu/f)^{1/2}$, the Ekman layer thickness, are used.

In Region I in Fig. 2.16, geostrophy is valid so thermal wind relation yields a velocity scale

$$V_G \sim \frac{g\alpha \Delta T_G \delta_T (1 - \delta_E/\delta_T)}{f l_y},$$

since the thickness of Region I is $(\delta_T - \delta_E)$. In Region II, the Ekman flux driven by a geostrophic flow of V_G in a homogeneous fluid (Pedlosky, 1987), which is the same as the retarding Ekman flux, is

$$Q_E = V_G \delta_E / 2.$$

The total meridional mass flux Q is

$$Q = Q_G + Q_E \sim U_G(\delta_T - \delta_E) + U_G \delta_E/2 \sim U_G(\delta_T - \delta_E/2).$$

From the heat equation $wT_z \approx \kappa T_{zz}$,

$$\delta_T \sim \frac{\kappa}{W} \sim \frac{\kappa l_y}{Q},$$

here continuity $W = Q/l_y$ has been used. Meridional heat flux per unit width H/l_x is then

$$\frac{H}{l_x} \sim \rho_o C_p \{U_G \Delta T_G (\delta_T - \delta_E) + U_G \Delta T_C \delta_E/2\}.$$

The first term in the curly bracket is due to the geostrophic meridional flow in Region I as in Fig. 2.16, where the meridional temperature difference is ΔT_G. The second term is due to the sum of the interior geostrophic flow and the retarding Ekman flux in Region II, where the meridional temperature difference is ΔT.

If we assume $\delta_E/\delta_T < O(1)$, we can expand all the variables using δ_E/δ_T. Since $r^{-1/2} = \delta_E/\delta_{T_n}$, and a thermal boundary layer thickness for a non-rotating system $\delta_{T_n} < \delta_T$, so $\delta_E/\delta_T < r^{-1/2}$. Thus, the condition $r > O(1)$, which we are interested in, and most of the

runs satisfy, makes the error of the expansion $(\delta_E/\delta_T)^2 = r^{-1} < O(1)$. If we expand the variables using δ_E/δ_{T_C} and solve using external parameters H and f,

$$\Delta T \sim (\rho_o C_p g\alpha)^{1/2}(fH)^{1/2}\left(1-\frac{7}{2}\frac{\delta_E}{\delta_T}\right)^{-1/2}\delta_T^{-1}, \quad \text{and} \tag{2.27}$$

$$\delta_T \sim \frac{3}{4}\delta_E + \left\{\frac{9}{16}\delta_E^2 + \left(\frac{l_x l_y^3 \kappa^2 \rho_o C_p}{g\alpha}\right)^{1/2}\left(\frac{f}{H}\right)^{1/2}\right\}^{1/2}. \tag{2.28}$$

The above relations can be written using the ones from the geostrophic scaling law $\delta_{T_{gs}}$ and ΔT_{gs}, which are in Table 2.1, as follows:

$$\begin{aligned} \delta_T &\sim \delta_{T_{gs}}\left(1+\frac{3}{4}\frac{\delta_E}{\delta_{T_{gs}}}\right), \\ \Delta T_C &\sim \Delta T_{gs}\left(1+\frac{\delta_E}{\delta_{T_{gs}}}\right). \end{aligned} \tag{2.29}$$

As expected, the correction becomes larger as f becomes slower so that δ_E becomes larger. The correction due to the Ekman layer, however, is small since δ_E/δ_T is small. Since δ_E increases as the rotation weakens, the correction becomes more important as expected. By introducing the main external parameters H and f to Eq. 2.28, one can calculate δ_T, which in turn can be used to obtain ΔT using Eq. 2.27.

The relation between ΔT and f from the corrected scaling law when $H_N = 50W$ is shown in Fig. 2.14 as a thick solid curve with an appropriate proportionality constant. Since the corrected scaling law is a polynomial, we cannot obtain an unique power law but we can obtain an average value. The correction weakens the power dependence of ΔT on f from 0.25 to about 0.17, which is closer to the experimental result 0.12. The relation between δ_T and f from the corrected scaling law when $H_N = 50W$ is in Fig. 2.15 as a thick solid line. The correction weakens the power dependence but the change is small compared to the scatter in the experimental data.

In Fig. 2.17, r versus $\Delta T_G/\Delta T$ from the experiment is shown. In other words, what portion in ΔT was due to geostrophic flow? It clearly shows that the friction effect increases with decreasing r. A thermal boundary layer becomes thinner as r decreases so that the Ekman layer becomes thicker compared to the thermal boundary layer. When $r > 10$,

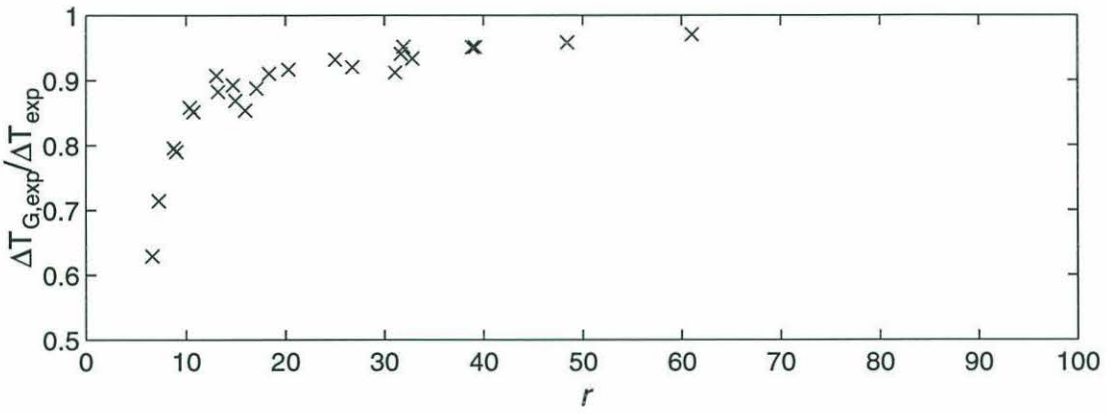

Figure 2.17: r versus $\Delta T_G/\Delta T$ from the experiment.

where most runs were done, more than 85% of ΔT was responsible for the geostrophic flow. The rest of ΔT was temperature drop across the Ekman layer, ΔT_F.

In Fig. 2.18, ΔT's from the corrected scaling law (ΔT_C) and from the experiment (ΔT_{exp}) are compared. In the figures, the runs with $r > O(1)$ were used. The dashed line represents perfect comparison between the scaling law and the experiment. The uncertainty in ΔT_C, which is from the 20% uncertainty in H, is about 10%. The variations in the temperature measurement as shown in Fig. 2.10(b) cause about 3% uncertainty in ΔT_{exp}. It is small compared to error in H and neglected. The thermal expansion coefficient α increases with temperature so α is assumed a linear function of temperature during the estimation of ΔT_C. The effect, however, is small compared to the uncertainty in ΔT_C. From the least squares solution to a line

$$\Delta T = 10^{0.61\pm0.02}\Delta T_C^{0.79\pm0.04}. \tag{2.30}$$

In Appendix 2.1, the estimation of the uncertainty in least squares solution is described.

If all the meridional heat transport can be explained by the scaling law, ΔT_{exp} and ΔT_C should show a linear relation, i.e., $\Delta T_{exp} \sim \Delta T_C^1$, within the uncertainty interval of the experiment. Although such a linear relation is outside of the experimental fit, Eq. 2.30, the

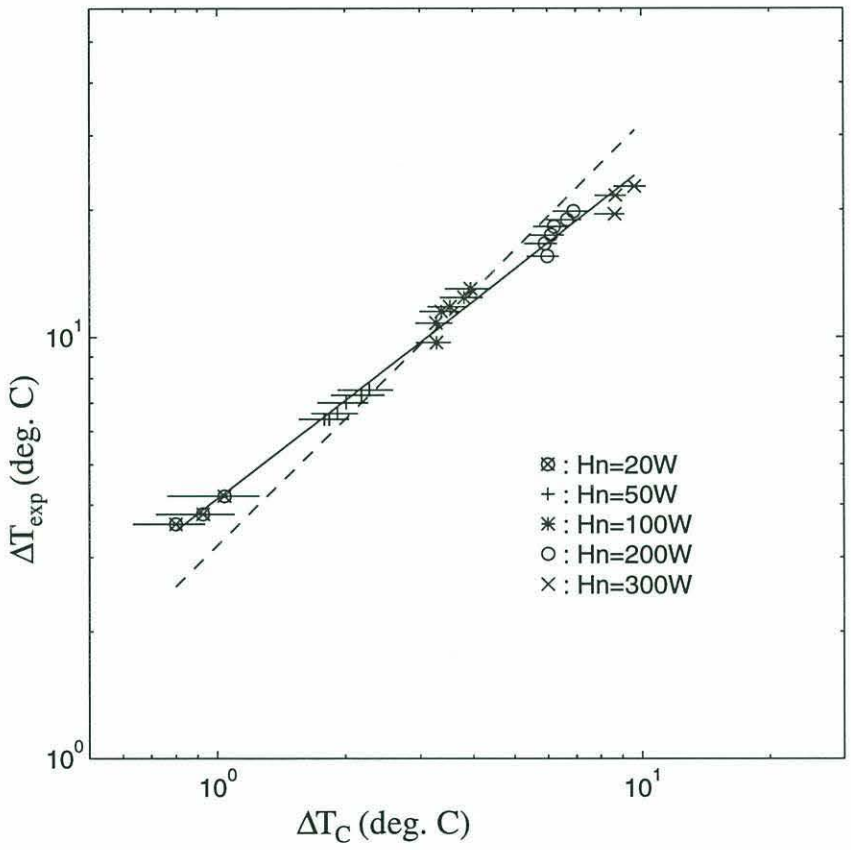

Figure 2.18: Comparison of $\Delta T(f, H)$'s from the corrected scaling law and the experiment. The dashed line is from the scaling law with a proportionality constant, 2.7. The solid line is the least squares fit of the experimental data, which is $\Delta T = 10^{0.61\pm0.02}\Delta T_C^{0.79\pm0.04}$.

fit itself is good since the uncertainty interval is small and no point is away from the fit. The internal parameter ΔT is determined by two control (external) parameters f and H_N that were varied independently by a factor of 10. Unless the dependences of ΔT on the external parameters are similar in the experiment and the scaling law such a fit cannot be obtained. The differences between the experiment and the corrected scaling law are small, so the scaling law can be considered as a first approximation of the experiment. In the other two scaling laws, the power dependences of ΔT on f are about three to four times larger than we observe, so statistically significant fits could not be obtained.

What processes are responsible for such differences? The power dependence in the fit is less than 1. The heat transport processes in the experiment are more efficient than those in the corrected scaling law. Processes other than the meridional overturning governed by geostrophy and bottom friction must be involved in the heat transport . The condition for baroclinic instability in the thermal boundary layer is (Pedlosky; 1987)

$$\frac{N\delta_T}{f} < l_{b.c.}\frac{2.399}{\pi},$$

where $N^2 = -g\alpha T_z$ and $l_{b.c.}$ is the length scale of baroclinic region. In the experiment, $N\delta_T/f \approx 20cm$ and $l_{b.c.}$ is comparable to the length of the tank. Baroclinic eddies could develop. The flow visualization, which is described in the next section, shows there were many eddies in the experiment. Although baroclinic eddies are not efficient enough to explain all the meridional heat transport of the experiment, they could contribute to the heat transport.

By assuming that the thickness of the thermal boundary layer is determined by the corrected scaling law, i.e., δ_T in the baroclinic scaling law (Eq. 2.12) is replaced by δ_T from the corrected scaling law, the residual in the fit ($\Delta T_{exp} - 10^{0.61}\Delta T_S$) and ΔT from baroclinic scaling law were compared. A suitable choice of a $O(1)$ proportionality constant made the residual and the correction due to baroclinic eddies comparable. A statistically reasonable fit between the the two could not be obtained, however.

In the absence of the bottom friction, the geostrophic scaling law can be used as an

approximation of the convective circulation in a rotating rectangular container. (The comparison between the experimental results after the removal of the frictional effects and the geostrophic scaling law shows a fit similar to Eq. 2.30.) If we assume a linear relation between ΔT_{exp} and ΔT_C, we get

$$\Delta T_{exp} = \Delta T_{G,exp} + \Delta T_{F,exp} \approx 2.2\Delta T_C = 2.2(\Delta T_G + \Delta T_F)$$

from the least squares fit. Thus,

$$\Delta T_{G,exp} \approx 2.2\Delta T_G,$$

and from the geostrophic scaling law, $\Delta T_G = \Delta T_{gs} \sim H_{G,exp}^{3/4}$, where the meridional heat transport due to the geostrophic flow of the experiment is $H_{G,exp}^{3/4}$. If we assume $\Delta T_{G,exp}$ is fixed, and estimate meridional heat transport with the geostrophic scaling law, we get

$$H_{gs} \sim \Delta T_{G,exp}^{4/3} \approx 2.2^{4/3} H_{G,exp}.$$

If we invert the above relation,

$$H_{G,exp} \approx 2.2^{-4/3} H_{gs} \approx 0.35 H_{gs}.$$

In Bryan and Cox (1967)'s numerical experiment, the proportionality constant for the meridional heat transport is about 0.3 and comparable to the experimental result, 0.35. If the similar conversion is done with the proportionality constant in Eq. 2.30, $10^{0.6}$, we get 0.16. The proportionality constant for meridional transport must be within 0.26 ± 0.1.

The correction due to the bottom friction was also applied to thermal boundary layer thickness. In Fig. 2.19, δ_T's from the corrected scaling law (δ_{T_C}) and the experiment ($\delta_{T_{exp}}$) are compared. The uncertainty in δ_{T_C} is due to that in H, and the error in $\delta_{T_{exp}}$ is from the resolution of vertical temperature profiles. The least squares fit to all data, which is the thin solid line of the figure, is

$$\delta_{T_{exp}} = 10^{-0.18\pm0.05} \delta_{T_C}^{1.4\pm0.24}.$$

If the thermal boundary of the experiment can be explained by the scaling law completely, $\delta_{T_{exp}} \sim \delta_{T_C}$ within the uncertainty interval of the fit. The deviation from a linear

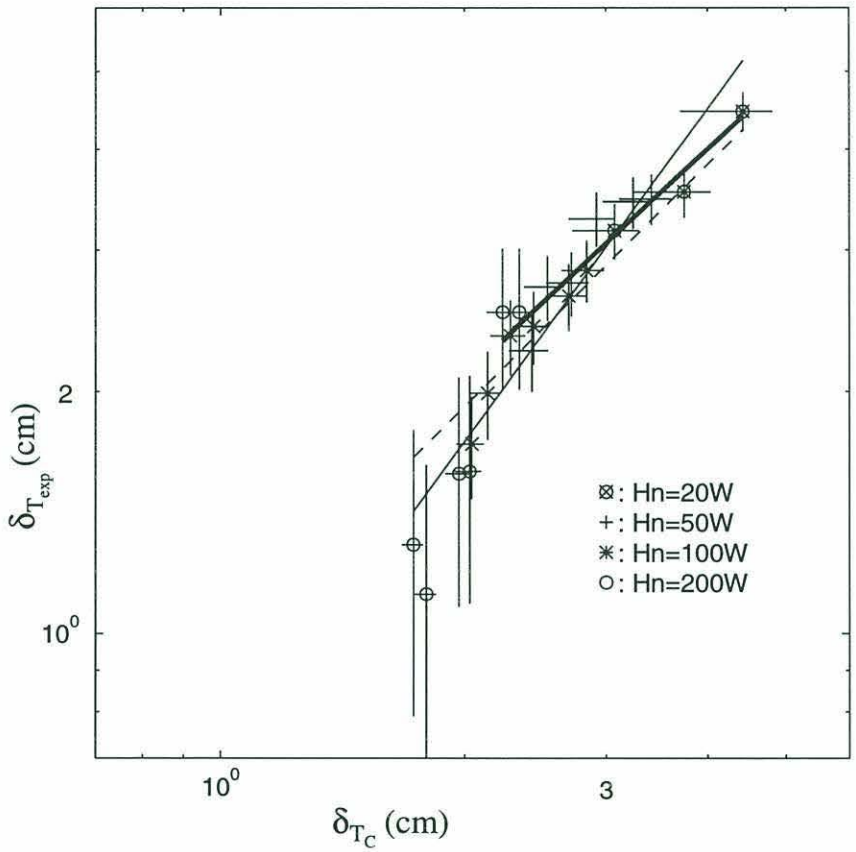

Figure 2.19: Comparison of δ_T from the corrected scaling law (δ_{T_C}) and the experiments ($\delta_{T_{exp}}$). The dashed line is from the geostrophic scaling law with a proportionality constant, 1.0. The thin solid line is the least squares fit of all the data, which is $\delta_T = 10^{-0.18\pm0.05}\delta_{T_C}^{1.4\pm0.24}$. The thick solid line is the least squares fit of $\delta_{T_{exp}} > 2cm$, which is $\delta_{T_{exp}} = 10^{0.04\pm0.08}\delta_{T_C}^{0.94\pm0.35}$.

relation is mostly due to the runs with $\delta_T < 2cm$ so that the resolution of the profiles, which was $5mm$, was not high enough to give a reasonable estimation of δ_T. If the runs of $\delta_T < 2cm$ are excluded, the least squares fit to the data, which is the thick solid line of the figure, is

$$\delta_{T_{exp}} = 10^{0.04\pm0.07}\delta_{T_C}^{0.94\pm0.35}. \tag{2.31}$$

Although the large errors in the data make the uncertainty interval of the fit large, the linear law is within the uncertainty interval. The values of δ_T are small and the scatter is large, so that the correction of the frictional effect does not have much effect. The thermal boundary layers from the two other scaling laws can be thicker than the water depth within the experimental parameter range, and power laws are significantly different from the experimental results.

2.3.5 Flow Visualization and Zonal Temperature Sections

The comparison between the experiment and the scaling law suggests that the experiment follows the corrected scaling law closely. To identify heat carrying flows directly, flow visualization was done using the thymol blue technique, and zonal temperature sections were made for selected parameters. In Fig. 2.20 flow patterns are shown. The method is equivalent to placing a source of neutrally buoyant dye at fixed locations, which are determined by the positions of visualization wires. The figures, thus, represent streak lines. A set of pictures from a single that shows the entire flow pattern was not obtained. All runs show a similar circulation patterns so pictures from different runs are compiled.

The dye streak (Fig. 2.20(a)) shows that near the upper left corner, there is a cold current toward the cold end along the wall to the left (Flow I). The flow becomes zonal when it meets the cold end wall and flows anti-cyclonically along the cold end wall. When the flow reaches the meridional wall to the right, it turns toward the hot end wall (Flow II). When the cold flow reaches near the end of the cooling plate, most of the cold water turns toward the wall to the left and becomes zonal, while the remaining part of the cold water continues to flow toward the hot end along the wall to the right. The zonal temperature

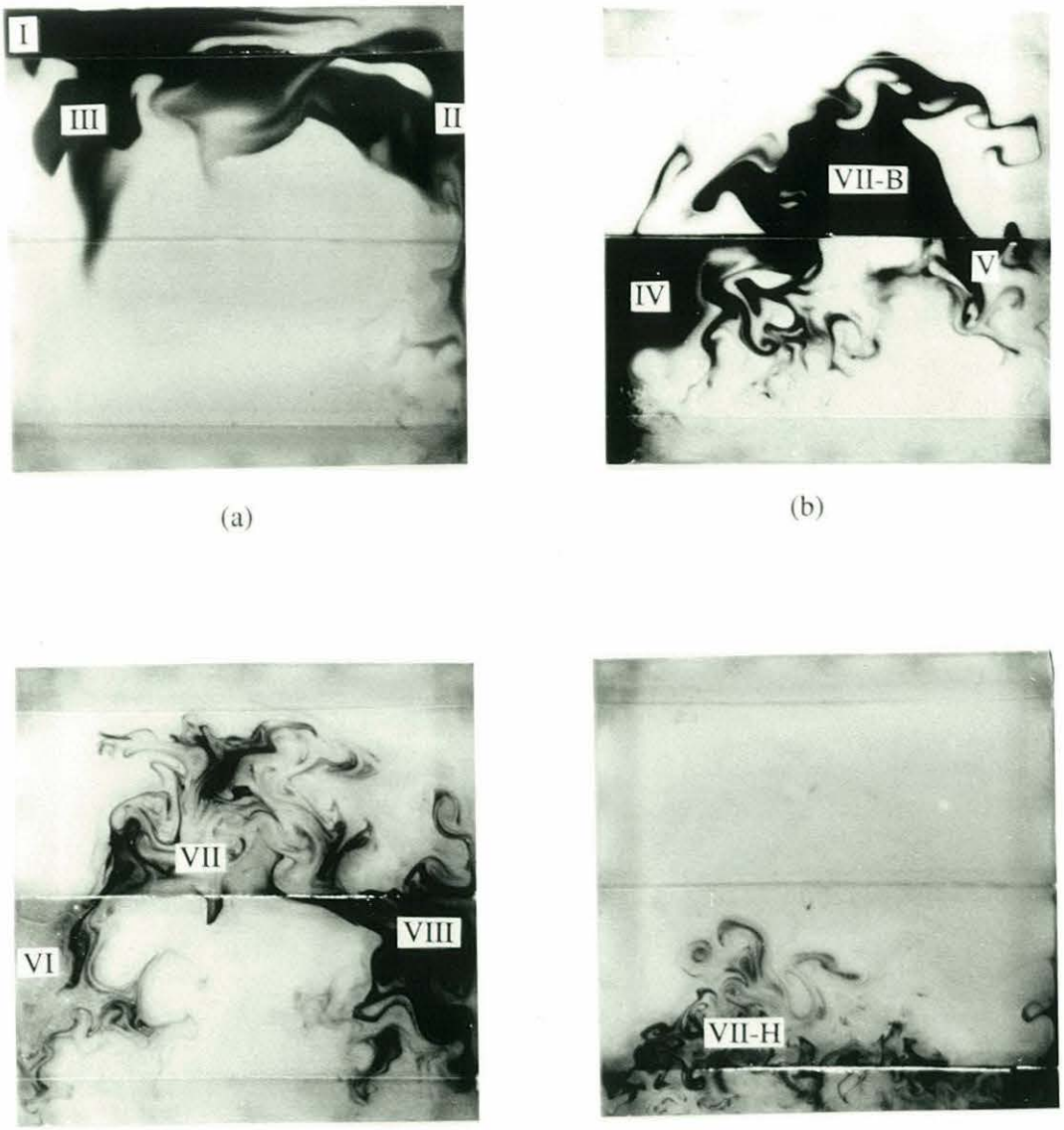

Figure 2.20: Flow pattern. Views from the above. The cold end wall is at the top and the hot wall is at the bottom of a picture.

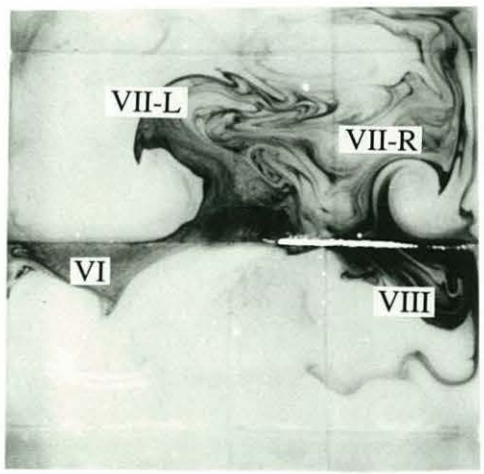

(e)

(f)

Figure 2.20 continued.: In (a) $y = 90cm$ (over the cooling plate), $z = 1cm$ and $t = 30min.$, (b) $y = 50cm$ (along the center zonal section), $z = 1cm$ and $t = 30min.$, (c) $y = 50cm$, $z = 7cm$ and $t = 30min.$, (d) $y = 10cm$ (over the heating pad), $z = 7cm$ and $t = 30min.$, (e) $y = 50cm$, $z = 7cm$, and $t = 68min.$, and (f) $y = 90cm$, $z = 7cm$ and $t = 63min.$ Here t means how long the wire has been activated in each case. In (a), (b), and (c), $f = 1s^{-1}$ and $H_N = 50W$. In (d) and (e) $f = 0.5s^{-1}$ and $H_N = 50W$. In (f) $f = 1s^{-1}$ and $H_N = 200W$.

section (Fig. 2.21(a)) also shows that there is an intensified cold water mass near the the wall to the right. As the zonal flow approaches to the wall to the left, most of it slowly turns toward the hot end wall (Flow III), and brings cold water to the hot end along the wall to the left (Flow IV in Fig. 2.20(b)). Some of the cold water from the wall to the right joins to Flow I and returns to the cold end. The two cold flows in opposite directions (Flows I and III) generate a dome-shaped cold water mass near the wall to the left as can be seen in Fig. 2.21(a). As sketch in Fig. 2.22, the water in the thermal boundary layer circulates anti-cyclonically over the cooling plates (Flows I, II), while some of it flows toward the hot end along the meridional wall to the left (Flow III).

As shown in Fig. 2.20(b), the major cold flow from the cold end toward the hot end is along the wall to the left (Flow IV). The figure also shows that there is another cold flow (Flow V) near the wall to the right, but it is weak compared to Flow IV. Thus, the zonal temperature section across the center of the tank shows more cold water near the wall to the left as shown in Fig. 2.21(b).

Between the center meridional section and the section near the cooling plate, the cold flow is mostly zonal. In the experiment, the cooling was confined to the upper $80cm < x < 100cm$ of the tank. Until the warm water reached near the cooling plate, the water could maintain its heat content and the meridional temperature gradient along the bottom was small. In Fig. 2.23, the meridional temperature gradient is small when $y < 60cm$.

As the water flowed over the cooling plate, the cooling started and the thermal boundary layer was formed. The meridional temperature gradient became larger over the boundary between the cooling plate and the insulating center plate ($60cm < y < 90cm$ in Figs. 2.23 and 2.12), and the gradient supported the zonal flow. Such a large temperature gradient made the boundary condition of this experiment different from those of numerical models or experiments, which were sinusoidal or linear. The temperature and velocity distribution of this experiment, especially near the boundary between the cooling plate and the middle plate, might be different from those of other studies. However, we are more interested in scaling laws related to large scale features and the experiment turned out to meet this

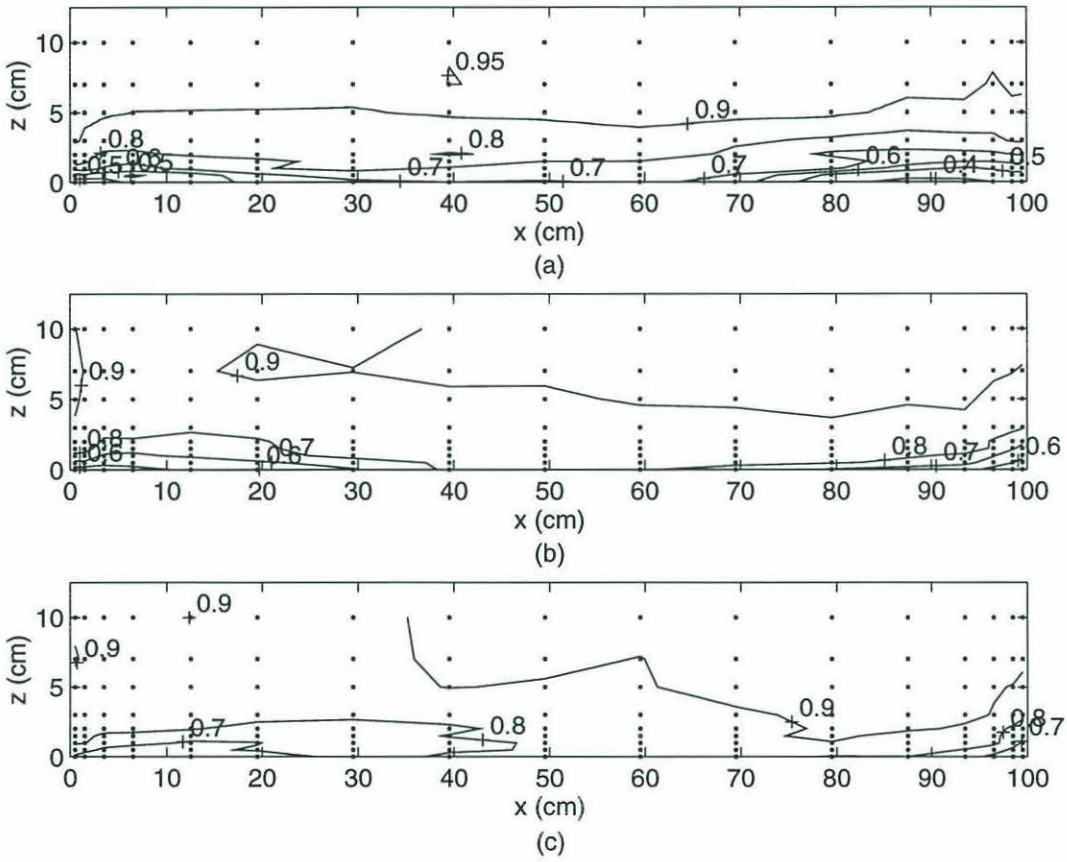

Figure 2.21: Zonal temperature sections when $f = 1s^{-1}$ and $H_N = 50W$ (a) $y = 70cm$, (b) $y = 50cm$, and (c) $y = 30cm$.

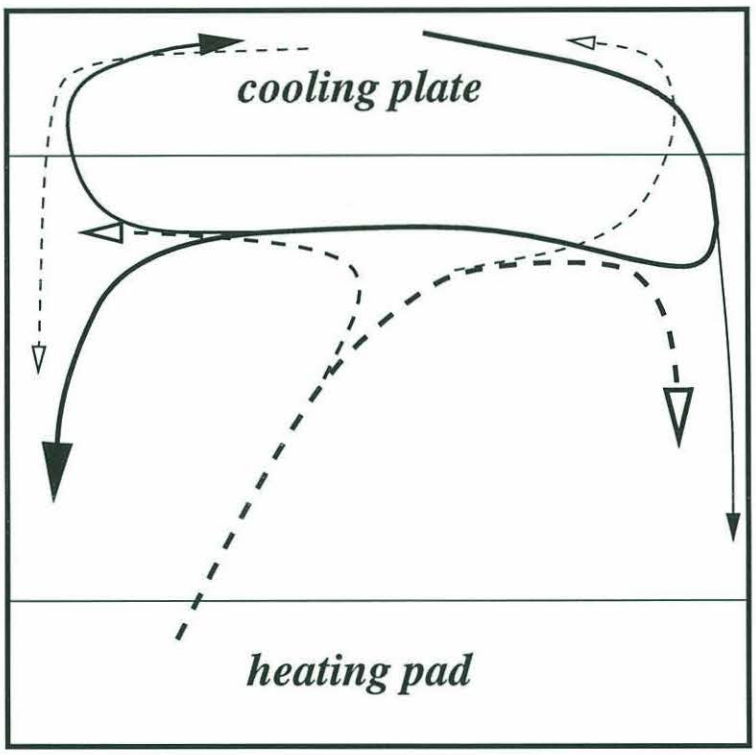

Figure 2.22: A schematic diagram of flow pattern. A solid curve represents cold current and a dotted curve represents warm current. If a solid curve and a dotted curve are stacked, the cold flow is near the bottom and warm flow is above the cold flow.

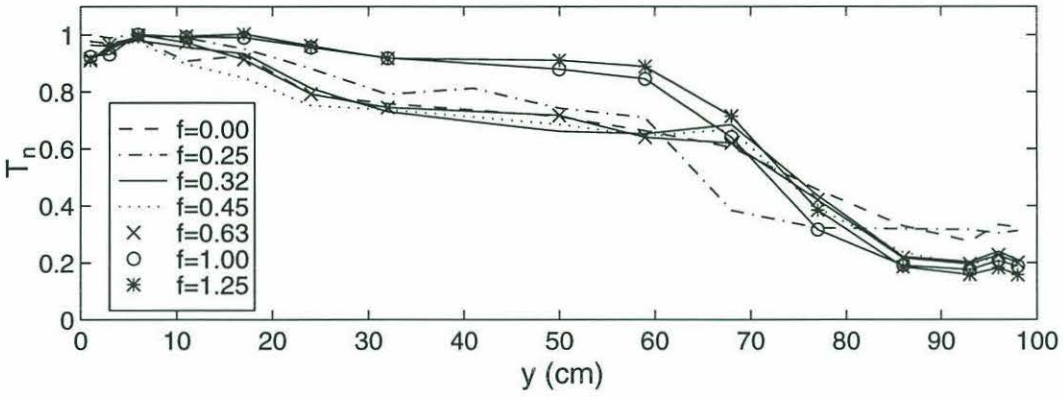

Figure 2.23: Normalized temperature along the bottom of the center meridional sections ($x = 49.5cm$) with $H_N = 50W$. Note that the temperature over the cooling plate was overestimated due to the size of the thermistors.

purpose.

Fig. 2.20(d) shows that warm water starts near the lower left corner and flows toward the upper right corner (Flow VII-H). Over the heating pad, the vertical motion was active. The dye would mix with the ambient water and decay rapidly so the streaks are not very clear. The center meridional section (Fig. 2.20(c)), however, shows the motion of the warm water clearly; the warm water flows toward the cold end along the center of the tank (Flow VII). It extends almost to the bottom so that the flow toward the cold end in Fig. 2.20(b) (Flow VII-B) is not cold water but a warm water as can be seen in the zonal temperature section Fig. 2.21(b).

When the warm water (Flow VII) reaches near the cooling plates, it splits into two zonal flows; one flows to the left forming cyclonic circulation (Flow VII-L), and the other flows to the right forming anti-cyclonic circulation (Flow VII-R) as shown in Fig. 2.20(e). When Flow VII-R meets the wall to the right, some of it returns toward the hot end along the wall to the right. The flow can be seen clearly in Fig. 2.20(c) near the wall to the right (Flow VIII). The remaining part of Flow VII-R turns cyclonically toward the cold end

and circulate along the walls of the tank. In Fig. 2.20(f), most of the dyed water started along the zonal visualization wire at $y = 90cm$ and $z = 7cm$ and flows cyclonically along the walls of the tank. The flow toward the hot end along the wall to the left (Flow VI in Fig. 2.20(c)) represents a part of the cyclonic warm flow. Flow VII-L eventually joins to the warm flow (Flow VI) and returned to the hot end. The motion of the warm water described is summarized in Fig. 2.22 as dashed lines

The flow pattern is more complicated than the one suggested earlier (Fig. 2.4). The circulation over the cooling plate, however, is similar to the expectation. To compensate for the diffusive heat loss through the cooling plates, warm water sank into the thermal boundary layer. The warm water experienced vortex column stretching, and a cyclonic circulation was induced. The cold water experienced vortex column squashing and a anti-cyclonic circulation was induced as sketched in Fig. 2.22.

In the equilibrium, the vertical vorticity balance in an f-plane was

$$f w_z = \nu \nabla^2 \zeta,$$

i.e., the production of vorticity by the vertical motion ($f w_z$) was dissipated by friction, since the thermal Rossby number $R_T \ll 0.1$, $f \gg \zeta$, and pressure $p = p(\rho)$ so the baroclinic vorticity production $\nabla\rho \times \nabla p = 0$. Here, ζ is the vertical component of the relative vorticity. In the thermal boundary layer, the frictional dissipation occurred in the Ekman layer along the bottom so

$$f \frac{W}{\delta_T} \sim \nu \frac{\zeta}{\delta_E^2}.$$

Thus,

$$\zeta \sim \frac{U_R}{l} \sim \frac{W}{\delta_T},$$

and from continuity we can see that the horizontal motion (U_R) induced by the relative vorticity is comparable to the speed of the overturning circulation.

The top surface is a free boundary so that in the interior away from the thermal boundary layer, the dissipation occurred within the side wall frictional boundary layers. In the presence of stratification, the thickness of a side wall boundary layer is δ_E (Barcilon and

Pedlosky, 1967). The stretching occurred over the horizontal surface but the dissipation occurred along the walls. If the areas of each surface are considered in the vorticity balance,

$$f\frac{W}{d}l^2 \sim \nu\frac{\zeta}{\delta_E^2}dl$$

so

$$\zeta \sim \frac{W}{d\varepsilon},$$

where $\varepsilon = d/l$, the aspect ratio. In the experiment, $d\varepsilon$ is $1.4cm$ and comparable to the thickness of the thermal boundary layer so are $W/d\varepsilon$ and W/δ_T. As the visualization shows, the vortical motions induced by the vertical velocity in the thermal boundary layer and the interior are within the same order of magnitude, although they are in opposite direction.

The warm water from the hot end did not show significant vortical motion until it met the cold water. If there was no thermal boundary layer, the water was almost homogeneous so that the Taylor-Proudman theorem held and $w_z = 0$. The downwelling, which compensated for the active upwelling over the heating pad, was constant within the geostrophic interior. The variation in the vertical velocity would be confined to the Ekman layer, and the vertical motion could not induce relative vorticity. As the warm water reached near the cooling plates, it started to feel the the thermal boundary at the bottom. Some of the water turned anti-cyclonically along the edge of the thermal boundary layer to conserve its potential vorticity, while some turned cyclonically due to the vortex column stretching.

In addition to the mean circulation, the visualization shows that there are many eddies in the warm water, whereas there are fewer in the cold water. The eddies within the warm water could not contribute heat transport because meridional temperature gradient in the warm water was almost zero. The eddies near the boundary between the cold water and warm water were expected to enhance mixing and heat transport locally.

The heat loss through the walls of the tank could deform isotherms and induce flows. The water in the tank was always warmer than the room temperature so that the heat loss would make isotherms tilt upward within a diffusive layer near the walls. If the diffusion

was a dominant process near the walls, the tilt in isotherm should be generic in temperature sections. Such isotherm tilt can be found in some locations (in Figs. 2.21(b) and (c), near $x = 100cm$), but there is no reason that the heat loss was confined to those locations; the tilt is not related to the diffusive layer but to the interior geostrophic flows. In Figs. 2.21(b) and (c), 0.9 isotherms near $x = 0cm$ are vertical. They might be an evidence of convective motion due to the side wall heat loss. The thickness of the side wall boundary layer is then about $3cm$. The flow visualization (Fig. 2.20) does not show any significant difference in flow pattern within about $3cm$ from the walls; the heat loss through the side wall did not modify the flow noticeably.

During the visualization, when the cover was removed, the formation of a few centimeters wide eddies, which were significantly smaller than those in Fig. 2.20, was observed throughout the tank within a few minutes. The eddies were due to the heat loss through the surface of the water. The evaporative heat loss described in Section 2.2.2 also could generate such eddies. The surface water temperature was uniform so that the formation of the eddies could not be localized. The eddies could modify the heat transport efficiency uniformly, but the evaporative heat loss was less than 20% of the meridional heat transport. The effects of the eddies due to the evaporation must not be significant.

Estimation of Geostrophic Shear Since zonal temperature sections are similar within the thermal boundary layers regardless of f and H_N, the geostrophic shear was estimated from a run with a relatively thick thermal boundary layer. Most of the stratification was confined to the thermal boundary layers where temperature distribution was not resolved well. Furthermore, the error in a thermistor could cause uncertainty comparable to the speed of the meridional overturning. Thus, the estimation of the geostrophic shear from the zonal sections, which are given in Fig. 2.24, should be analyzed with care.

Over the cooling region there were strong zonal flows. When they reached to the meridional wall, they turned toward the hot end or cold end. The dye streaks mixed and it was not possible to estimate flow speeds accurately. Since we are more interested in the

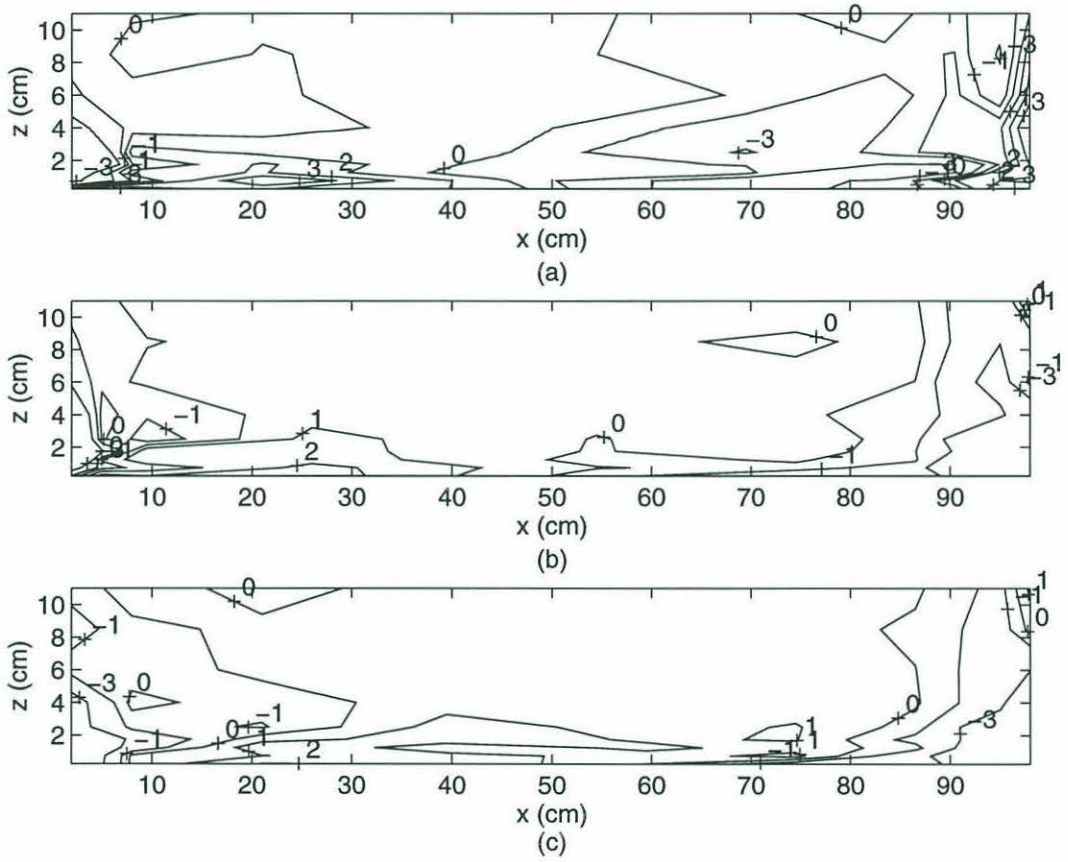

Figure 2.24: Geostrophic shear estimated from zonal temperature sections when $f = 1s^{-1}$ and $H_N = 50W$ (a) $y = 70cm$, (b) $y = 50cm$, and (c) $y = 30cm$. The unit of the contours is $10^{-2}s^{-1}$.

meridional flows, the focus will be given to the center zonal sections where the flow was predominantly meridional.

When Figs. 2.20(b) and (c) are compared, we can see that the flow toward the hot end along the wall to the right becomes stronger with height. The vertical shear between Flows V and VIII in Fig. 2.20 is

$$(-24cm/30min - (-5cm/30min))/6cm = -1.8 \times 10^{-3}s^{-1}$$

excluding $x > 90cm$. The mean shear in this region from Fig. 2.24(b) is about $-3 \times 10^{-3} \sim -2 \times 10^{-3}s^{-1}$ and comparable to that from the visualization. The warm flow (Flow VIII), in fact, intensifies toward the wall to the right but the cold flow (Flow V) becomes weaker (Fig. 2.20(c)). Thus, the shear intensifies to the right as in Fig. 2.24(b).

When $x < 40cm$, the shear is positive within the bottom $2cm$ or so. In Fig. 2.20, Flow III is faster than Flow VI. Although the visualization was done in the same level, Flow III is colder than Flow IV. When it reached the center section it would be below the visualization wire of the section. The estimate of the vertical shear between the two cold flows is

$$(-40cm/30min - (-20cm/30min))/1cm = 10 \times -10^{-3}s^{-1}.$$

The spacing between the two cold flows could not be obtained accurately, so we assumed that the spacing is $1cm$, the depth of the visualization wire in Fig. 2.20(b). The actual spacing must be smaller than $1cm$ so the estimate can be considered as a lower bound. The estimation from the zonal temperature section is about $-15 \times 10^{-3}s^{-1}$ so that they are about the same magnitude.

Except for $x > 80cm$ and away from the bottom $1cm$, the flow pattern is basically barotropic. The vertical shear is small as can be seen in Fig. 2.24(b). Although flow visualization was not made near the heating pad, the dye streaks from the center zonal section maintain the barotropic tendency until they are exposed to the heating pad directly. The vertical shear along $y = 30cm$ (Fig. 2.24(c)), thus, is similar to that along $y = 50cm$.

Near the cooling plate ($y = 70cm$), there is a thin positive shear layer centered at $x = 23cm$ neat the bottom. As in other sections, this represents the cold flow toward the

hot end in Fig. 2.20(a) (Flow III). Visualization was not made along the section so that the value cannot be verified.

Due to the poor resolution of the temperature within the thermal boundary layer and the error in the thermistors, the accurate estimation of vertical shear could not be obtained. The comparison between the geostrophic shear estimation and the flow visualization, however, shows that they are within the same order of magnitude.

2.4 Discussion

The experiment showed that convection driven by differential heating in a rectangular basin can be explained by the geostrophic scaling law in the absence of friction. The experiment, however, lacks two important factors of the real oceans, which are the β-effect and the wind stress at the surface of the oceans. Using a simple scaling argument, the effects of β and the surface wind stress on such convective circulation are described.

2.4.1 Convective Circulation in a β-plane

Stern (1975) derived a scaling law for convective circulation in a pie-shape basin in a β-plane. The thermal wind balance, and a balance between downward heat diffusion and upwelling of cold water were assumed. By assuming that the potential energy released by warm rising thermocline motion and cold sinking polar motion is balanced by dissipation in the Ekman layer, he derived the same scaling law for the thickness of a thermal boundary layer as that of a rotating annulus, the Ekman scaling law described in Section 2.1.2.

He concluded that both the β-effect and meridional boundaries were not important in thermal boundary layer structures. Although meridional boundaries were included, the meridional geostrophic flow due to zonal pressure gradient was not included. The meridional mass transport was from the Ekman transport driven by zonal geostrophic flows as in his Ekman scaling law.

It is not easy to simulate the baroclinic β-effect with a stratified laboratory experiment, so the effect of β on convective circulation is discussed using a simple scaling argument. Assume a rectangular ocean in a β-plane as sketched in Fig. 2.25. Meridional temperature difference ΔT is applied along the surface. If we exclude the water mass formation region, which is confined to a narrow region near the northern end, the ocean can be considered as a two-layer system. The lower layer is equivalent to the homogeneous deep oceans below the thermocline. The upper layer is equivalent to the surface layer above the the thermocline. The interface, thus, is equivalent to the thermocline.

Assume uniform vertical motion W, which compensates the water mass formation, from

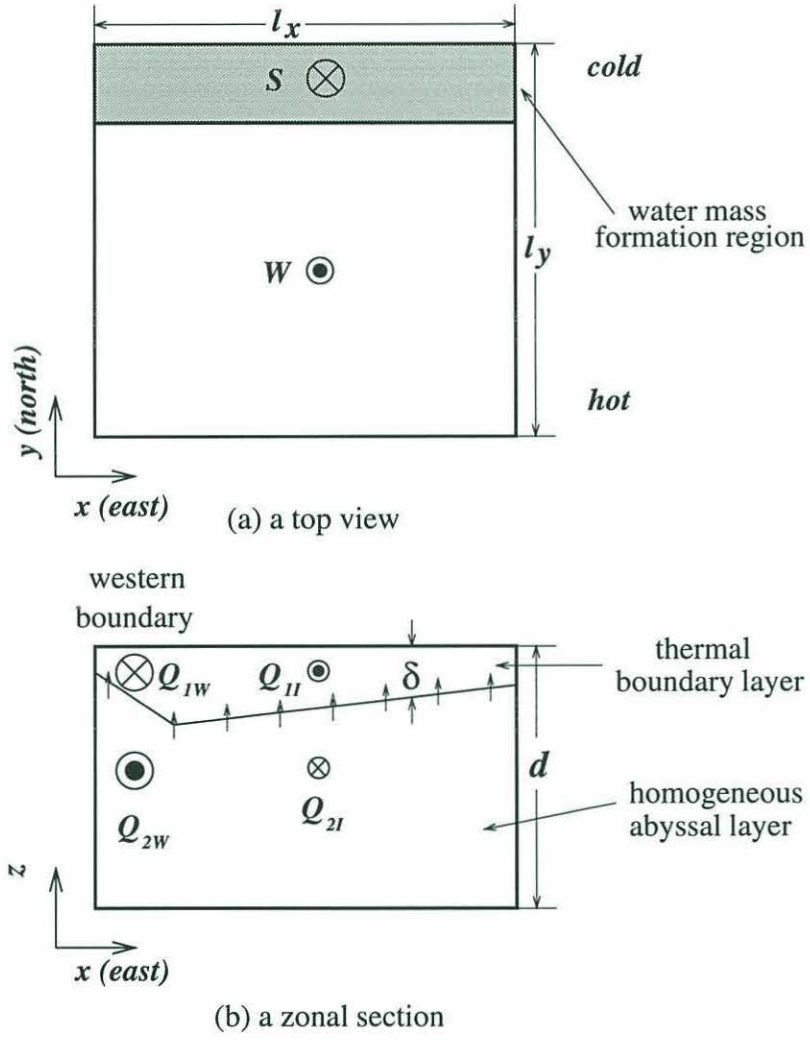

Figure 2.25: A sketch of a rectangular basin in a β-plane. (a) a top view and (b) a zonal section

the lower layer into the upper layer across the interface. The water mass formation in the northern region drives the circulation in the lower layer as in Stommel and Arons (1960). The interior vertical motion stretches the lower layer so the linear vorticity balance in the lower layer

$$\beta v_2 = f\frac{\partial w}{\partial z}$$

yields

$$\beta V_2(d - \delta_T) = fW,$$

since vertical motion vanishes at the bottom. Here V_2 is the meridional velocity scale in the lower layer. If the thermal boundary layer is thinner than the depth of the basin, i.e., $d \gg \delta_T$,

$$V_2 \sim \frac{fW}{\beta d} > 0,$$

so the interior flow is northward.

To the north of a certain latitude line θ, the mass balance in the lower layer among the interior mass transport $Q_{2I} \approx dl_x V_2$, the western boundary transport Q_{2W}, vertical mass flux $WA(\theta)$, where $A(\theta)$ is the surface area of the basin north of θ, and the water mass formation rate $S = WA(\theta_S)$, where the southern wall of the basin is at θ_S and $A(\theta_S) = l_x l_y$, requires

$$Q_{2W} = -Q_{2I} - S + WA(\theta) < 0.$$

The western boundary current is southward, and its transport is larger than that in the interior since the interior has to supply the upwelling. The net meridional transport in the lower layer is $Q_{2W} + Q_{2I} = -S + WA(\theta)$, and is southward and smaller than $|Q_{2W}|$ and $|Q_{2I}|$ as in Stommel and Arons (1960).

The vertical motion shrinks the upper layer so the vorticity equation yields the meridional velocity in the upper layer V_1

$$V_1 \sim -\frac{fW}{\beta\delta_T} < 0,$$

and the interior flow is southward. If we consider the mass balance in the upper layer to the north of θ,

$$Q_{1W} = -Q_{1I} + S - WA(\theta) > 0.$$

The western boundary transport is northward and its transport is larger than that in the interior. The upwelled water should return to the north to satisfy continuity. The interior flow is southward and it cannot carry the upwelled water. Instead, the northward western boundary current should take the water to the north so the boundary transport is larger than the interior transport. The net meridional transport is $Q_{1W} + Q_{1I} = S - WA(\theta)$, and is northward. As in the lower layer, the transport is smaller than $|Q_{1W}|$ and $|Q_{1I}|$.

The interior flows in the lower layer and the upper layer are opposite direction so that the thermal wind relation requires

$$\frac{f(V_1 - V_2)}{\delta_T} \sim \frac{g\alpha\Delta T}{l_y}.$$

Here, we assume $T_y \sim T_x$. If we assume $\delta_T \ll d$ and use V_1 and V_2 obtained earlier,

$$\delta_T \sim \left(\frac{l_y W f^2}{g\alpha\beta\Delta T^2}\right)^{1/2}.$$

The upward advection of cold water across the interface should be balanced by the downward diffusion of heat ($wT_z \approx \kappa T_{zz}$), so

$$W \sim \frac{\kappa}{\delta_T}.$$

If we eliminate W from the above two relations, the thermal boundary layer thickness δ_T becomes

$$\delta_T \sim \left(\frac{\kappa l_y f^2}{g\alpha\beta\Delta T}\right)^{1/3}. \tag{2.32}$$

This is the same as that by Robinson and Stommel (1959), Eq. 2.21.

The meridional heat flux H is

$$H \sim \rho_o C_p \Delta T S,$$

and since $S = Wl_x l_y$

$$H \sim \rho_o C_p \left(\frac{g\alpha l_y l_x^2 \kappa^2 \beta \Delta T^4}{f^2} \right)^{1/3} . \tag{2.33}$$

If $\beta = f/l_y$ is introduced, δ_T and H in Eqs. 2.32 and 2.33 are the same as those of a rectangular basin in f-plane, Eqs. 2.17 and 2.20, respectively.

Stommel (1965) calculated the circulation driven by uniform vertical motion in a two-layer ocean using the linear vorticity balance and mass balance as in this study, when the thickness of the interface is given. Later, Veronis (1976) solved such a problem much more rigorously and obtained circulation pattern and the shape of the interface, when the upper layer depth along the eastern boundary is given. The unknown locations and rate of deep water mass formation in remote oceans, that communicates with the basin of interest, does not allow one to obtain exact solutions. If we confine our interest to a single hemispheric basin, and specify the location and the rate of water mass formation, we can obtain exact solution within his framework. However, there is no way of parameterizing the upper layer depth along the eastern boundary, that determines the scale depth of the interface. Although the analysis of circulation in β-plane described in this paper is much simpler than those of Stommel (1965) and Veronis (1976), it was possible to determine the thickness of upper layer by introducing the thermodynamics.

In an f-plane basin, the vertical motion due to water mass formation induces relative vorticity and horizontal circulations. The combination of the horizontal gyres and the meridional overturning circulation happens to produce strong flows near the wall to the left (equivalent to the west in the Northern hemisphere) looking from warm region to cold region as shown in Fig. 2.4. There, however, is no distinction between the interior and western boundary layer in dynamics. The relative vorticity is balanced by dissipation within the frictional layers along the boundaries of the container. In a β-plane basin, in the interior, the vertical motion produces not relative vorticity but southward or northward motion due to the planetary vorticity gradient. The western boundary layer is required to balance mass and vorticity as the interior circulations forces.

Although, the balances for horizontal motions are different in two cases, the scales for

the meridional heat transport and thermocline thickness follow the same relation. Winton (1996) performed a series of numerical experiments in which β was varied. When β was increased from zero to the standard value of the oceans $2 \times 10^{-11} m^{-1} s^{-1}$ with $f_o = 10^{-4} s^{-1}$, the meridional heat transport was increased by 20%. This does not necessary prove that β-effect and the western boundary current do not play any role in the meridional overturning circulation, but this tells us that f determines most of the meridional heat transport at least within the parameter range of oceanic relevance. Since a thermal boundary layer is an indicator of heat transfer efficiency (as explained in Section 2.1.5) and the heat transports are the same in both oceans, so do δ_T's.

2.4.2 The Effect of Wind Stress

In Bryan and Cox (1967), wind stress at the surface had no apparent effect on meridional heat transport, although the wind stress changed horizontal circulation from a single gyre structure to a faster double gyre one. The wind driven gyre was faster than the thermally driven one, but a large part of the former is simply recirculation and did not contribute to the meridional overturning circulation much.

The thermocline thickness from the geostrophic scaling law (the advective-diffusive thermocline) is not compatible to the Ekman pumping at the surface. Stommel and Webster (1962) show how Ekman pumping modifies the advective-diffusive thermocline in the interior of an ocean with a similarity solution. The zonal advection of heat was neglected, and the same vertical structure and a balance between the advection and diffusion were assumed. The ocean could be divided into two vertical regions. The upper region is above the thermocline with $W > 0$, and the lower region is below the thermocline $W < 0$. The interface between the two layer represents the depth of the thermocline. The diffusion acts only at the interface so that the density balance is advective away from the interface. The location and the thickness of the interface are determined by matching temperature, vertical velocity and their vertical gradients through the interface.

In a subtropical ocean, the thermocline becomes an internal boundary layer. The depth

is the same as the thermocline thickness from the ideal fluid (wind driven) thermocline theory (δ_a from Eq. 2.23). The thickness of the boundary layer is

$$\delta_I \sim \left(\frac{df_o^2 \kappa}{g\alpha \Delta T \delta_a \beta} \right)^{1/2} = \left(\frac{dl f_o \kappa}{g\alpha \Delta T \delta_a} \right)^{1/2},$$

where δ_a is given in Eq. 2.23 and $\beta = f_o/l$ is used. If the values used to estimate δ_T and δ_a in Section 2.1.6 are introduced to the above relation, δ_I is about $100m$ and smaller than δ_a. In subpolar ocean, $w < 0$ from the top to the bottom so that the interface becomes the same as the sea surface. Ekman suction at the surface lifts the thermocline and makes it shallow. Salmon (1990) showed similar results with a similarity solution of a simpler form.

We can guess that wind stress does not change the meridional heat transport much, but it does change the thermocline depth; where $W_E < 0$, it makes the thermocline deep, and where $W_E > 0$, it makes the thermocline shallow. At this stage, however, it is not possible to a give quantitative answer to how the surface wind stress modifies the thermocline thickness and the meridional heat flux of the diffusive thermocline theory.

Appendix 2.1

The least square solution of an overdetermined system with a set of N data points $(x_i,\ y_i)$ to a linear model

$$\mathbf{Y} = \mathbf{Xm},$$

where,

$$\mathbf{m} = (a\ \ b)^T,$$

$$\mathbf{y} = (y_1\ \ldots\ y_N)^T, \text{ and}$$

$$\mathbf{X} = \begin{pmatrix} 1 & x_1 \\ 1 & x_2 \\ \vdots & \vdots \\ 1 & x_N \end{pmatrix}$$

is

$$\mathbf{m} = (\mathbf{X}^T\mathbf{X})^{-1}\mathbf{X}^T\mathbf{Y}.$$

Here, x_i's are the values of the dependent variable known exactly, y_i's are known measurements, a and b are model parameters, and the superscript 'T' means transpose. When the variance in $\mathbf{Y}$ is known, the variance in $\mathbf{m}$, cov($\mathbf{m}$), can be estimated as follows (Menke, 1989);

$$\text{cov}(\mathbf{m}) = ((\mathbf{X}^T\mathbf{X})^{-1}\mathbf{X}^T)\mathbf{S}((\mathbf{X}^T\mathbf{X})^{-1}\mathbf{X}^T)^T.$$

Here, $\mathbf{S}$ is a diagonal matrix and S_{ii} is the variance of y_i. The diagonal elements of cov($\mathbf{m}$) represent the variance of $\mathbf{m}$.

In the experiment, x_i's are ΔT_C and δ_{T_C} from the corrected scaling law, and y_i's are ΔT and δ_T from the measurements, respectively. In the analysis, x_i's are to be known exactly. In the experiments, however, uncertainty in H produces uncertainty in x_i's and measurement error produces uncertainty in y_i's.

In the case of ΔT, uncertainties x_i's are much larger so the uncertainties in y_i's are ignored. The least squares solution of $x_i = ab^{-1} + b^{-1}y_i$ and its variance are obtained while considering $-ab^{-1}$ and b^{-1} as model parameters. By inverting the solution, a and b along

with their variances were obtained. It is possible that $y_i = a + bx_i$ and $x_i = ab^{-1} + b^{-1}y_i$ yield different solutions since model parameters are different. In this case, the scatter in the data is small so that the difference is very small and not significant.

In the case of δ_T both x_i's and y_i have uncertainties. The variances in the model parameters due to those in y_i could be obtained easily from $\mathrm{cov}(\mathbf{m})$. The scatter in the data is large so that $y_i = a + bx_i$ and $x_i = ab^{-1} + b^{-1}y_i$ yield different solutions. Thus, the uncertainties in a and b due to those in x_i could not be obtained by solving $x_i = ab^{-1} + b^{-1}y_i$. Considering the propagation of errors, the variance σ_v^2 in the values of any function v (Press *et. al.*, 1986) is

$$\sigma_v^2 = \sum_{i=1}^{N} \sigma_{x_i} (f_{x_i})^2,$$

where v is a or b. Since the uncertainties in x_i's and y_i's are independent, the larger values are taken.

Chapter 3

A Box Model

3.1 Introduction

The sea surface thermal forcing, which acts in the direction of the present thermohaline circulation in the North Atlantic, is opposite to the haline forcing from the fresh water flux. The strong negative feedback between the sea surface temperature and the surface heat flux removes changes in the sea surface temperature rapidly. However, the fresh water flux, which arises from the local imbalance between precipitation and evaporation, is independent of the sea surface salinity. It has been known that the competition between the two forcings and the difference in the boundary conditions of temperature and salinity may give rise to multiple equilibria of the thermohaline circulation under identical boundary conditions (See Weaver and Hughes, 1992; Marotzke, 1994; Whitehead, 1995 for reviews). Thus, the thermohaline circulation driven by the two competitive forcings can be unstable against changes in the fresh water flux (Huang *et al*, 1992) or salinity in polar oceans (Walin, 1985; Marotzke, 1990).

If, for example, we assume that the fresh water flux to the polar ocean becomes larger somehow, then the salinity of the polar ocean declines so that the meridional surface salinity gradient intensifies. We may be able to assume, however, the strong negative feedback between the sea surface temperature and heat flux does not allow much change in the

sea surface temperature and the meridional sea surface temperature gradient. The change in the surface salinity gradient is mainly responsible for the variations in the meridional surface density gradient, which drives the circulation. The increased surface salinity gradient weakens the surface density gradient, and subsequently the circulation. The polar ocean gains more fresh water so that the polar salinity declines further. The salinity gradient intensifies more and the circulation weakens further until it reaches a new equilibrium.

If the change in the fresh water flux is large enough, the circulation becomes so slow that the salinity anomaly cannot be removed but intensifies until the salinity gradient overcomes the temperature gradient and reverses the circulation. This reversal is known to occur rapidly so it is called a *thermohaline catastrophe.* Since the thermohaline circulation is responsible for more than half of the oceanic meridional heat transport in the North Atlantic (Bryden and Hall, 1980; Hall and Bryden, 1982), such a sudden change in the circulation would cause large effects on the climate of the earth.

Studies ranging from simple box models to fully developed primitive equation numerical models have demonstrated the thermohaline catastrophe. With a box model such as Stommel (1961), it is easier to change parameters and study processes related to the stability of thermohaline circulation. The basic principle of a box model is simple. There are two well-mixed boxes; one for a polar ocean and the other for an equatorial ocean as sketched in Fig. 3.1. The density in each box is determined by the air-sea heat and the fresh water exchanges (or virtual salt flux) and the advection of heat and salt between the adjacent boxes. The density difference between the boxes determines the circulation and thereby the advection of heat and salt.

When the thermal forcing dominates, it drives a *thermal mode* circulation. The density in each box is mainly determined by temperature so that the water in the polar box is denser. The cold and fresh deep current flows from the polar box to the equatorial box, and the warm and salty surface return current flows from the equatorial box to the polar box. When the haline forcing dominates, it drives a *haline mode* circulation, which is opposite to the thermal mode circulation. The density is mainly determined by salinity so that the

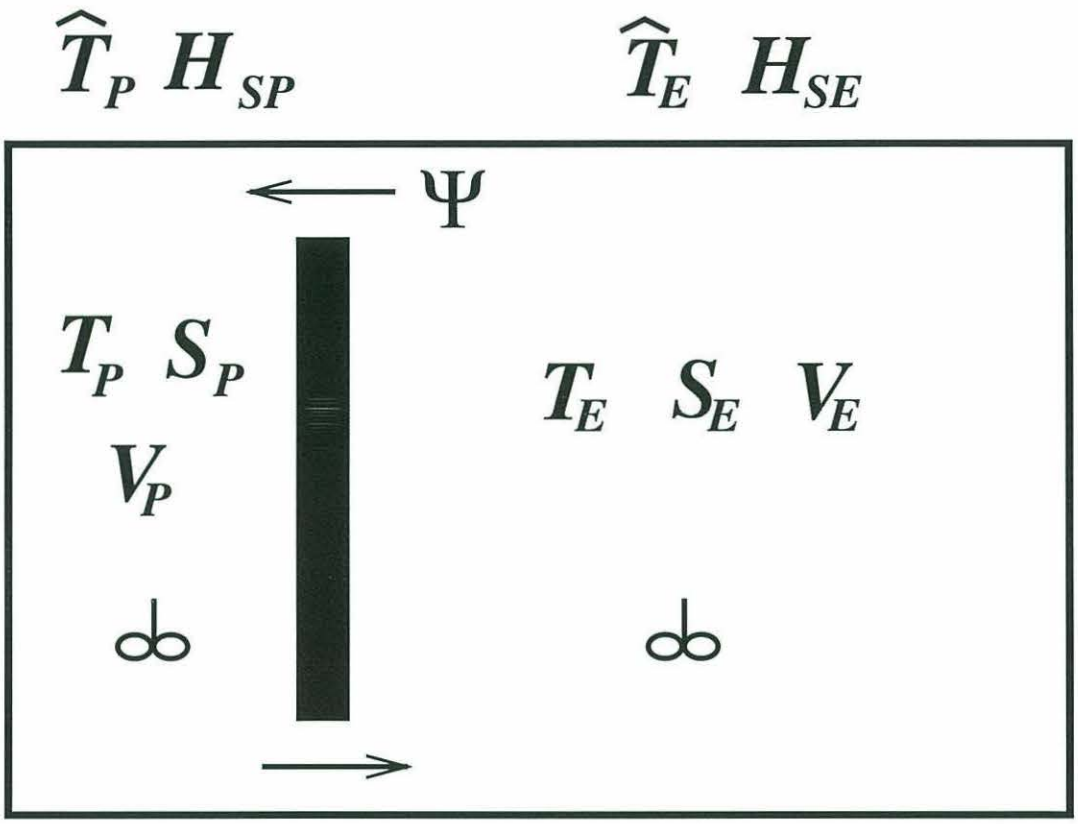

Figure 3.1: A configuration of a two box model. The temperature of each box T_i, where $i = P$ and E, are restored to $\hat{T}_i$. The salinity of each box is S_i. H_s represents air-sea fresh water exchange or virtual salt flux. The mass transport Ψ is determined by the density difference between the two boxes. A counterclockwise circulation gives positive Ψ.

water in the equatorial box is denser. The warm and salty deep current flows from the equatorial box to the polar box and the cold and fresh surface current flows from the polar box to the equatorial box.

Since the difference in the boundary conditions of temperature and salinity can cause the thermohaline catastrophe, many studies have been focused on the parameterization of boundary conditions for temperature and salinity, in other words the air-sea heat and fresh water exchanges. In the case of temperature, a restoring boundary condition (Haney, 1971)

$$\text{heat flux} \sim \frac{T_{ref} - T_{sea}}{\tau_T}$$

has been commonly used. Here, τ_T is a restoring time constant for temperature, and the subscript 'ref' is for a reference value.

In the case of salinity boundary conditions, there are a few ways. (For more detail discussions of salinity boundary conditions see Huang (1993).) One is fresh water flux from evaporation (E) minus precipitation (P) and river run off. The fresh water flux at the surface not only modifies salinity but also drives circulation such as the Goldsbrough-Stommel circulation (Goldsbrough, 1933; Stommel, 1957; Huang and Schmitt, 1993).

Another is a virtual salt flux condition, which is deduced from $E - P$ as follows:

$$\text{salt flux} \sim (E - P)\frac{\overline{S}}{d},$$

where d is the depth of a box. Another is a restoring boundary condition

$$\text{salt flux} \sim \frac{S_{ref} - S_{sea}}{\tau_S},$$

here S_{ref} is a reference salinity. In the oceans, not salt but fresh water leaves or enters the surface so that the fresh water flux condition is physical and natural as Huang (1993) shows. However, when $\tau_S \to \infty$ and $S_{ref} \to \infty$, with a finite S_{ref}/τ_S, the virtual salt flux is weakly influenced by salinity so that a restoring boundary condition can be used as a first approximation to a flux boundary condition (Welander, 1986). In most studies, however, S_{ref} is determined from climatological mean surface salinity. It also has been shown that

when $\tau_S \gg \tau_T$, the thermohaline catastrophe is possible under restoring conditions for temperature and salinity (Stommel, 1961).

The salinity boundary conditions described earlier are independent of the sea surface temperature, although the evaporation (E) is dependent upon the sea surface temperature. If we assume the thermal mode circulation becomes weaker somehow, the meridional temperature gradient becomes larger so that the equatorial box becomes warmer or the polar box becomes colder. As the equatorial oceans become warmer, more fresh water evaporates while producing a positive salinity anomaly. The evaporated fresh water is carried to the polar oceans by atmospheric motion and produces a negative salinity anomaly in the polar oceans. The meridional salinity gradients becomes stronger so that the circulation becomes weaker. The meridional temperature gradient intensifies further, and so does the fresh water flux. Thus, the interaction between the sea surface temperature gradient and the fresh water flux produces a positive feedback to the thermal mode circulation.

Recently, a virtual salt flux condition from (E-P) that includes the positive feedback has been introduced in a series of studies by Nakamura *et al.* (1994), Marotzke and Stone (1995), and Marotzke (1996). The fresh water flux of the condition

$$(E - P) = \frac{\gamma_n}{\epsilon_w}(T_E - T_P)^n.$$

Here ϵ_w is the ratio of the ocean area to the catchment area of the ocean basin, and γ_n is atmospheric transport efficiency. Since the boundary condition includes the interaction between the sea surface temperature and the fresh water flux, it can be called an "interactive" salinity boundary condition. (In Nakamura it et al. (1994), it is called the "eddy moisture transport-thermohaline circulation" (EMT) feedback since eddy activities, which become stronger as meridional temperature gradient increases, are responsible for the fresh water transport in the atmosphere so the interaction between the fresh water flux and thermohaline circulation.) When $n = 0$, the virtual salt flux from the interactive condition is the same as that from fixed $(E - P)$. A thermal mode circulation with the interactive condition is less stable than one with fixed (E-P) or a restoring boundary condition for

salinity (Nakamura *et al.*, 1994; Marotzke and Stone, 1995; Marotzke, 1996).

Another density determining factor, whose effect on the stability of the thermohaline circulation has mostly been neglected, is the heat and salt advection that is controlled by the mass flux Ψ between the adjacent boxes. In almost all the box models,

$$\Psi \sim \Delta\rho,$$

where $\Delta\rho$ is the density difference between the two adjacent boxes. The relation can be motivated from the balance between frictional dissipation (κu_{zz}) and a meridional pressure gradient (p_y/ρ_o) (Stommel, 1961), which is

$$\kappa U/l^2 \approx \Delta P/D\rho_o \sim \Delta\rho.$$

The proportionality constant of such a relation can be chosen to meet the observed oceanic values of thermohaline circulation, which is $\Psi \approx 10Sv$ when $\Delta T = 20°C$ and $\Delta S = 2ppt$. While introducing such a scaling law, the effect of the Earth's rotation is not considered at all (Stommel, 1961; Thual and McWilliams, 1992) or it was claimed that the effect has been included in the scaling law (Joyce, 1991).

In a box model, the equation of motion is highly truncated or integrated for simplicity. It is not easy to include some important factors of the thermohaline circulation such as the effects of the thermocline and rotation explicitly. Using a 2×2 box model, Huang *et al.* (1992), in fact, showed that the thermohaline catastrophe is a surface phenomenon, geometrically depending on the thickness of the upper boxes, which is equivalent to the thermocline depth. If a proper scaling law is used, the effects of the Earth's rotation and the thermocline on heat and salt transports can be included in a box model without increasing the resolution.

Based on Stommel (1961), a simple two-box model with the mass transport relation from the geostrophic scaling law (Eq. 2.19) is developed. Numerical experiments by Colin de Verdiére (1988) and Huang and Chou (1994) show that the meridional mass transport does not follow the geostrophic scaling law, although the meridional heat transport and the thickness of the thermal boundary layer (Bryan, 1991) do. The relations confirmed

through the experiment described in Chapter 2 are not for the mass transports but for the meridional heat transport and the thermal boundary layer thickness. As discussed later in this chapter, the advection of buoyancy is more important in determining the structure of the model than the mass transport. For the convenience of the calculation, the mass transport relation is used in the model.

In the temperature equations of the model, restoring boundary conditions are used. The results are compared with those from a model with frictional mass transport law while focusing on the catastrophic transition points. By comparing results under a restoring salinity conditions and the interactive condition, the effects of salinity boundary condition on the stability of thermohaline circulation is also studied.

3.2 A Two Box Model

The model consists of a polar box and an equatorial box as shown in Fig. 3.1, whose geometry is basically the same as that of Stommel (1961). The equations of temperature and salinity in each box, using notations of Thual and McWilliams (1992), are

$$\begin{aligned} V_P\dot{T}_P &= C_{TP}(\hat{T}_P - T_P) + |\Psi|(T_E - T_P) \\ V_P\dot{S}_P &= V_P H_{SP} + |\Psi|(S_E - S_P) \\ V_E\dot{T}_E &= C_{TE}(\hat{T}_E - T_E) + |\Psi|(T_P - T_E) \\ V_E\dot{S}_E &= V_E H_{SE} + |\Psi|(S_P - S_E) \end{aligned} \tag{3.1}$$

$$\begin{cases} \textit{restoring} & H_{Si} = \dfrac{1}{\tau_S}(\hat{S}_i - S_i),\ i = P, E \\ \textit{interactive} & \begin{cases} H_{SE} = \dfrac{1}{2}F_n(T_E - T_P)^n \\ H_{SP} = -H_{SE}. \end{cases} \end{cases}$$

The subscript P is for the polar box and E is for the equatorial box. The quantities with a hat such as $\hat{T}$ and $\hat{S}$ are reference temperature and salinity. The volume of a box is V_i, where $i = E$ or P, $\tau_T = V_i/C_{Ti}$ and $\tau_S = V_i/C_{Si}$ are restoring time scales for temperature and salinity, respectively, and $F_n = (\gamma_n\overline{S})/(\epsilon_w d)$.

The volume transport between the boxes Ψ can be represented in two different ways:

$$\Psi \equiv \begin{cases} \Psi_G = C_G[\alpha(T_E - T_P) - \beta(S_E - S_P)]^{1/3} & \textit{geostrophic} \\ \Psi_F = C_F[\alpha(T_E - T_P) - \beta(S_E - S_P)] & \textit{frictional}, \end{cases} \tag{3.2}$$

where C_G and C_F are constants whose values are set to yield $\Psi = 10Sv.$ when $\Delta T = 20°C$ and $\Delta S = 2ppt$, which is the present oceanic state of the model. For thermal mode $\Psi > 0$, and for haline mode $\Psi < 0$.

In the temperature (salinity) equation, the first terms in the right hand side represent air-sea heat (fresh water or salt) exchange, and the second terms represent advective heat (salt) flux from the adjacent box. The heat (salt) advection is independent of the sign of Ψ since it is determined by the magnitude of the meridional mass transport and the temperature (salinity) difference between the two boxes.

Following Thual and McWilliams (1992), the non-dimensionalization factors for the variables are

$$\begin{array}{cc} \text{time} & \tau_{To} = 100 \text{ days} \\ \text{mass transport} & (1/V_P + 1/V_E)^{-1}/\tau_{To} \\ \text{temperature} & (1/V_P + 1/V_E)^{-1}/\alpha\tau_{To}C_F \\ \text{salinity} & (1/V_P + 1/V_E)^{-1}/\gamma\tau_{To}C_F. \end{array}$$

The mass transport Ψ is determined by $\Delta\rho = \alpha(T_E - T_P) - \beta(S_E - S_P)$, so $\Theta = T_E - T_P$ and $\Sigma = S_E - S_P$ are more convenient variables than T and S. The dimensionless equations are then

$$\begin{aligned} \dot{\Theta} &= \zeta - \Theta(\tau + |\Psi|), \\ \dot{\Sigma} &= H_s - \Sigma|\Psi|, \end{aligned} \tag{3.3}$$

$$\Psi = \begin{cases} \lambda(\Theta - \Sigma)^{1/3} = \lambda\Delta\rho^{1/3} & \text{geostrophic model} \\ \Theta - \Sigma = \Delta\rho & \text{frictional model} \end{cases} \tag{3.4}$$

$$H_s = \begin{cases} \eta - \xi\tau\Sigma & \text{restoring condition} \\ F_n\Theta^n & \text{interactive condition,} \end{cases} \tag{3.5}$$

where $\lambda = C_G C_F^{1/3}[(1/V_P + 1/V_E)\tau_T]^{2/3}$. The thermal forcing $\zeta = \hat{T}_E - \hat{T}_P$, and the haline forcing $\eta = \xi(\hat{S}_E - \hat{S}_P)$ (or F_n and n), $\xi = \tau_T/\tau_S$ and $\tau = \tau_{To}/\tau_T$ are the control parameters of the model. The multiple equilibria occur when $\xi \ll 1$.

Thual and McWilliams (1992) showed that when $\xi = 0.002$ a frictional two box model and a frictional two-dimensional model show similar bifurcation structures. All the calculations in this study were performed with $\xi = 0.002$, and the effect of varying ξ was not studied. In most calculations, $\zeta = 0.00577$ so that $\Theta = 20°C$ in an equilibrium state when $\Psi = 10Sv.$ and $\tau_T = 100$ days, in dimensional units. Nakamura *et al.* (1994) showed that $n \approx 3.5$, but for simplicity n is set to 1, following Marotzke and Stone (1995). The effect of different n is discussed briefly later.

In Fig. 3.2, the two mass transport laws are compared. The solid line is the mass transport for the geostrophic model, Ψ_G, and the dashed line is the one for the frictional

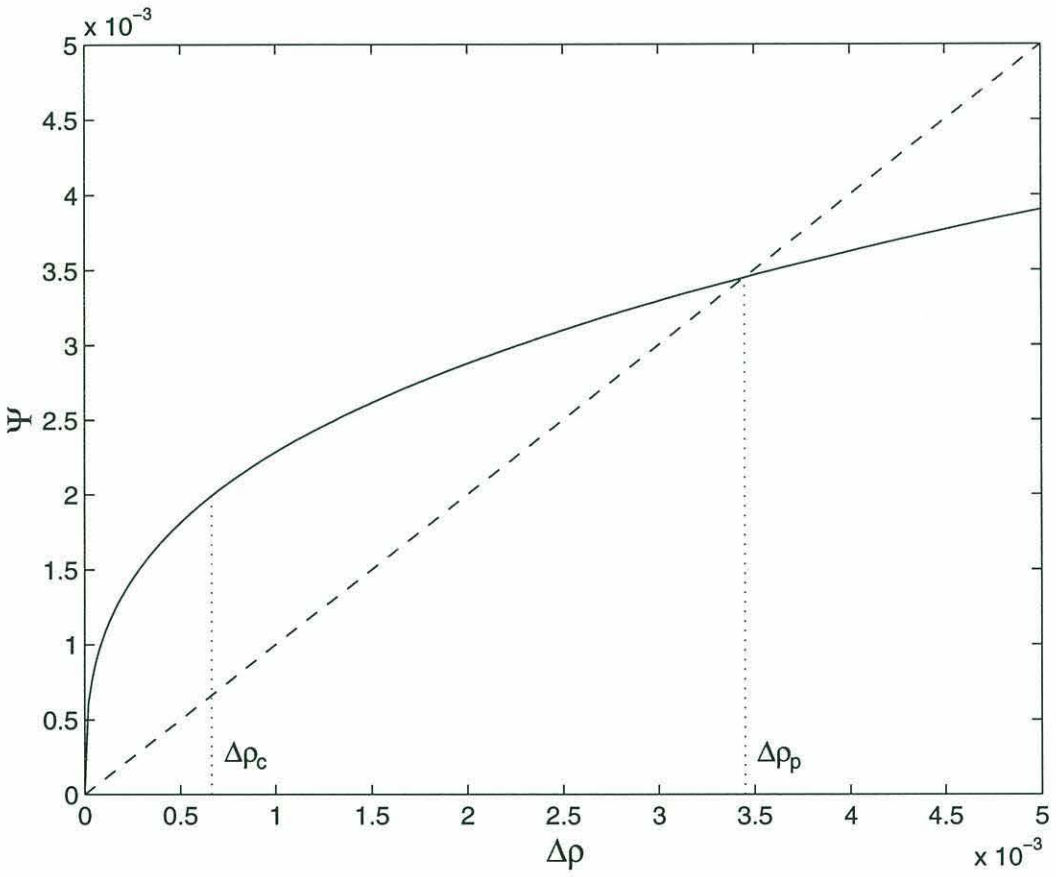

Figure 3.2: The meridional mass transport Ψ versus $\Delta\rho$. The solid curve is for the geostrophic model, Ψ_G, and the dashed line is for the frictional model, Ψ_F. The value of the present North Atlantic is shown as $\Delta\rho_p$. When $\Delta\rho < \Delta\rho_c$, $d\Psi_G/d\Delta\rho > d\Psi_F/d\Delta\rho$.

model, Ψ_F. Both scaling laws give the same mass transport, by definition, when $\Delta\rho = \Delta\rho_p$, which represents the meridional sea surface density gradient of the present North Atlantic. When the haline forcing, η, becomes larger than the present value so that $\Delta\rho < \Delta\rho_p$, we find that $\Psi_G/\Psi_F > 1$. Thus, the meridional heat and salt transports are greater in a model with the geostrophic mass transport law.

The equilibrium solution of Eqs. 3.3, 3.4 and 3.5 can be determined graphically. Equilibrium $\Delta\rho$ from equilibrium temperature and salinity, Eq. 3.3 with $\dot{\Theta} = 0$ and $\dot{\Sigma} = 0$, is

$$\Delta\rho = \Theta - \Sigma = \frac{\zeta}{\tau + |\Psi|} - \frac{\eta}{\tau\xi + |\Psi|}, \tag{3.6}$$

if restoring salinity boundary condition is used. Similar approach can be applied to models with interactive condition. In Fig. 3.3, the dash-dotted curves represent the above equation with various η. The dashed line is $\Delta\rho$ from the mass transport of the frictional model, Eq. 3.4(b). The intersections between a dash-dotted curve and the dashed line are equilibrium solutions of the frictional model for given parameters. The solid curve is $\Delta\rho$ from the mass transport of the geostrophic model, Eq. 3.4(a). The intersections between the solid curve and a dash-dotted curve are equilibrium solutions for the geostrophic model for given parameters.

In the geostrophic model, when η (haline forcing) is small ($\eta < \eta_o$), the solid curve and the dash-dotted curve meet at one point (point O) in the first quadrant; only a thermal mode solution is possible. As η increases, Σ becomes larger so that $\Delta\rho$ decreases; the dash-dotted curve moves downward. When $\eta = \eta_o$, the two curves meet at two points (points A and C); multiple equilibria occurs. As η increases further ($\eta_o < \eta < \eta_{T_G}$), the two curves meet at three points; two in the first quadrant and one in the third quadrant.

It is known that the thermal mode solution with smaller Ψ is an unstable equilibrium, a saddle point (Stommel, 1961). As η increases further until $\eta = \eta_{T_G}$, the unstable thermal equilibrium point moves up while the stable one moves down along the curve until they shrink to one point (point B) in the first quadrant. At the same time the intersection in the third quadrant moves downward. When η becomes even larger ($\eta > \eta_{T_G}$), the dash-

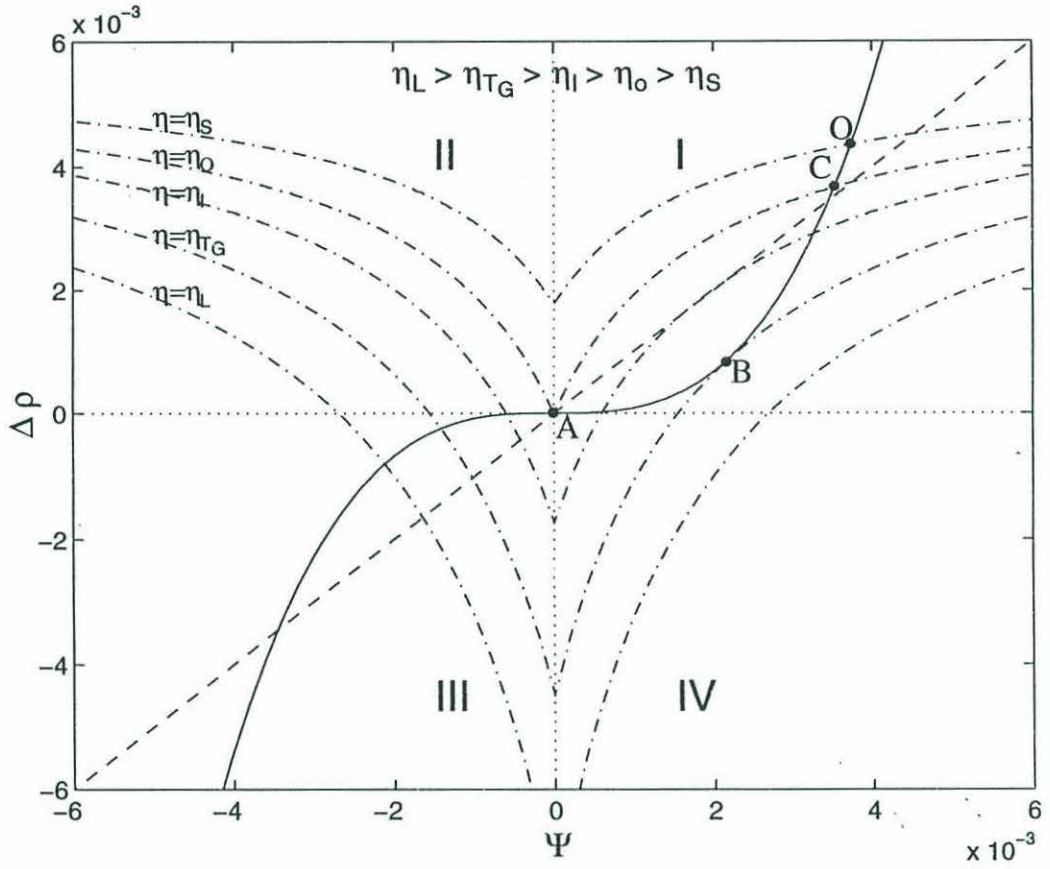

Figure 3.3: Graphical representation of the equilibrium solutions of Eqs. 3.3, 3.4, and 3.5 when restoring salinity boundary condition is used. During the calculation, $\zeta = 0.00577$ $(20°C)$, $\tau = 1$ $(\tau_T = 100 days)$ and $\xi = 0.002$. The quadrants labeled I-IV are separated by dotted lines. The dash-dotted curves are for $\Delta\rho$ from the temperature and salinity equations (Eq. 3.6). The solid curve is $\Delta\rho$ from the mass transport of the geostrophic model (Eq. 3.4(a)). The dashed line is $\Delta\rho$ from the mass transport of the frictional model (Eq. 3.4(b)).

dotted curve and the solid curve meet only at one point in the third quadrant so only a haline mode is possible. The equilibrium solution of the frictional model shows qualitatively similar dependence on η.

Using the above features, we can determine the multiple equilibria regions analytically. In Fig. 3.4, the results from models with the restoring salinity boundary condition are presented. The constants used in the calculations are $V = V_E + V_P = 5000km \times 5000km \times 4km$, $V_P = 0.1V$, $V_E = 0.9V$, $\alpha = 2 \times 10^{-4}\,{}^{\circ}C^{-1}$, $\gamma = 8 \times 10^{-4} ppt^{-1}$, $\tau = 1$ ($\tau_T = 100\,days$). A geostrophic thermal mode is possible below the solid, and a frictional one below the dashed one. The upper bound of a thermal mode is the family of the point B of Fig. 3.3 in (ζ, η) space. A haline mode is possible above the dotted line, which is the zero circulation line (Thual and McWilliams, 1992) $\eta = \xi\zeta$, in both models. The line is the family of the point A of Fig 3.3 in a (ζ, η) space. The domain common to both modes in each model is the multiple equilibria region where two opposite modes are possible under the same boundary conditions.

The equilibrium Ψ from the models with the restoring salinity boundary conditions is in Fig. 3.5. The solid curves are for the geostrophic model and the dotted curves are for the frictional model. The lower branches ($\Psi < 0$) are for the haline modes and the upper branches are for the stable thermal mode in each case. The middle branches (thin curves) are for the unstable thermal modes for both cases. The stable branches (thick curves) were obtained by integrating Eqs. 3.3, 3.5(a) and 3.4(a) or 3.4(b) over time numerically until they reached an equilibrium state while varying η by a small amount. Such numerical integration cannot yield unstable solutions, so the unstable branches were obtained by solving the steady versions of the equations numerically.

As one can expect from Fig. 3.3, both the geostrophic model and the frictional model show qualitatively similar characteristics when the haline forcing varies. For fixed thermal forcing (ζ), as the haline forcing (η) increases from zero, the salinity gradient (Σ) intensifies. The temperature also changes, but the strong negative feedback between the temperature of a box and the reference temperature prohibits significant change in temperature. Although

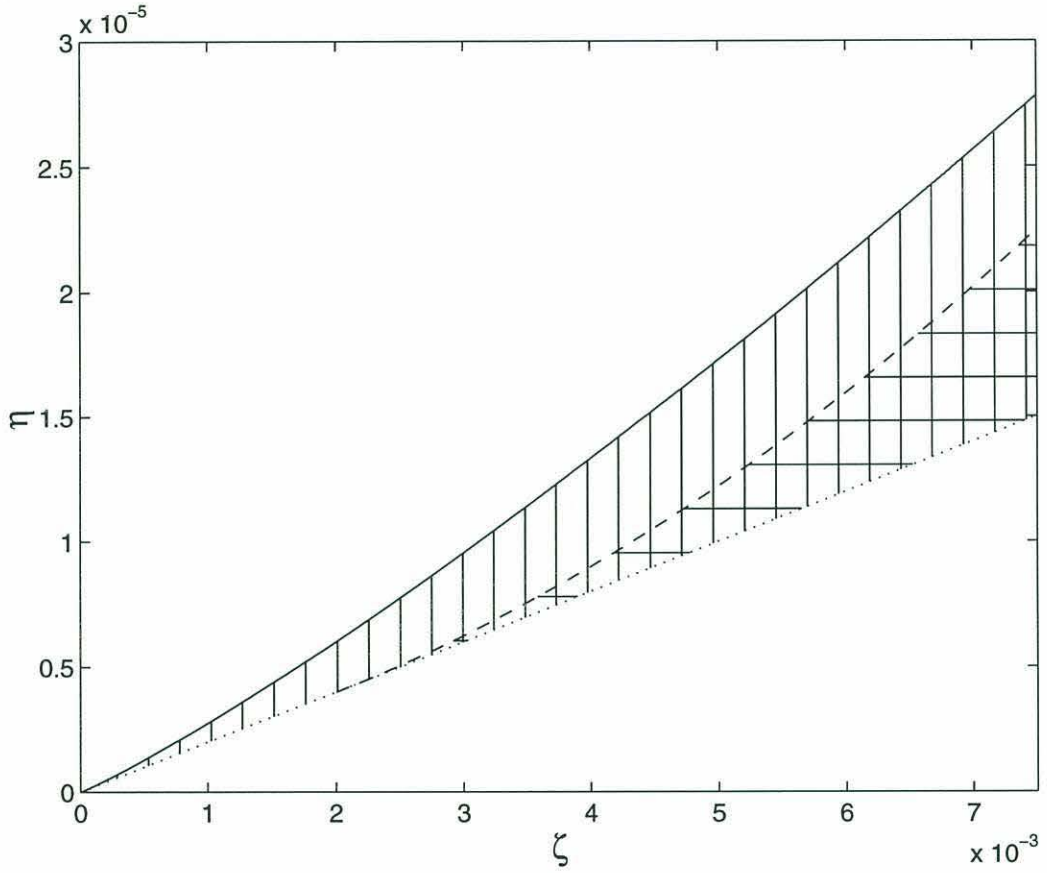

Figure 3.4: The domain for multiple equilibria is shown here as a region where the haline mode and thermal mode overlap. The dotted line is the zero circulation line and common to both models. This line is the family of the point A of Fig. 3.2 in $(\zeta,\ \eta)$ space. It is the lower bound of the haline mode and of the multiple equilibria region. The solid curve is the upper bound of the thermal mode and of the multiple equilibria region with the geostrophic box model. This curve is the family of the point B of Fig. 3.2 in $(\zeta,\ \eta)$ space. The dashed curve is the one with the frictional box model. The multiple equilibria region for the geostrophic model has vertical hatches, and that for the frictional model has horizontal hatches.

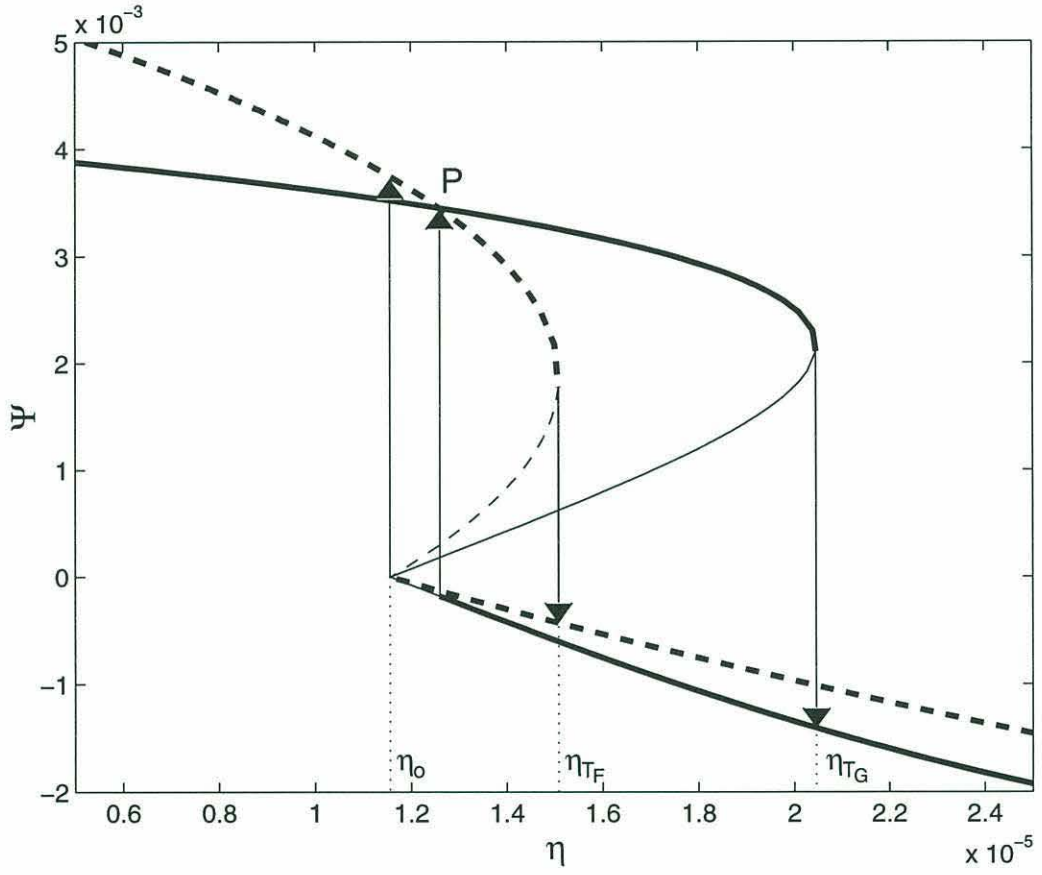

Figure 3.5: The mass transport Ψ versus the haline forcing η, with $\zeta = 0.00577$ and $\tau = 1$. The solid curves are for the geostrophic model and the dotted curves are for the frictional model. The arrows indicate the direction of change in each case. The middle branches (thin curves) in each case are for the unstable thermal modes.

the temperature gradient is larger, the change in the density gradient is mainly controlled by the salinity gradient.

The intensified Σ weakens the density gradient so that Ψ becomes weaker gradually along the stable thermal mode branch until $\eta = \eta_T$, where η_T is the catastrophic transition point from a thermal mode circulation to a haline mode. Note that the geostrophic model shows significantly higher η_T. At the transition point $\Psi > 0$ so that the temperature gradient is larger than the salinity gradient. After the transition, the salinity gradient becomes stronger than the temperature gradient. The circulation follows the haline mode branch as η increases beyond η_T.

When η declines from a value larger than η_T, the salinity gradient gradually weakens. The buoyancy forcing weakens so that the strength of the circulation ($|\Psi|$) becomes weaker along the haline mode branch until, in the frictional model, it approaches the zero circulation line ($\eta = \eta_o$), where the salinity gradient and the temperature gradient are exactly the same so that the circulation stops. If the haline forcing weakens further, a haline mode is not possible so that the circulation reverses to a thermal mode catastrophically. In the geostrophic model, the haline mode becomes unstable and the circulation reverses to the thermal mode before it reaches the zero circulation line. Its effect to the multiple equilibria region is small within the parameter of interest for the present oceans, so it will not be discussed.

Based on a similar frictional box with fresh water flux, Huang *et al.* (1992) argue that the present North Atlantic is close to the transition point, η_T, so that a small increase in the polar fresh water flux such as rain can reverse the present thermohaline circulation to a haline mode. If the frictional model is used, the present ocean of the model (point P) is close to the transition point η_{T_F}, as shown in Fig. 3.5, so that one can draw a conclusion similar to that of Huang *et al.* (1992). In contrast, if the geostrophic model is used, one could conclude that it is unlikely that a small increase in the haline forcing (or fresh water flux) causes a transition from a thermal mode circulation to a haline mode one.

Joyce (1991) used a two-hemisphere model with the frictional mass transport law. When

an asymmetric sinusoidal perturbation in the salinity boundary condition was applied to a stable thermal mode circulation, which represents the present oceanic circulation, an oscillation between a thermal mode and a haline mode with a frequency different from that of the perturbation was found. He suggested that this oscillation might be related to the glacial oscillation. Thual and McWilliams (1992) showed that when $\xi \ll 1$ the circulation in a complicated box model can be treated as a linear superposition of a two box model, so Joyce's (1991) calculation can be compared to that of the present study. The oscillations suggest that the amplitude of the perturbation is comparable to the width of the multiple equilibria region of his model. Since the geostrophic model shows a significantly wider multiple equilibria region than that of the frictional model, a version of Joyce's model with the geostrophic scaling law is unlikely to show such oscillations between a thermal mode and a haline mode under the same perturbation.

In Fig. 3.6, a hysteresis diagram from models with the interactive condition are presented while considering F_1 to be an external parameter. By comparing Fig. 3.6 and Fig. 3.5 one can see that the result from models with the interactive condition is qualitatively similar to those with the restoring salinity boundary condition. Multiple equilibria, two thermal mode and one haline mode, are possible under the same boundary conditions. The thermal mode of weaker circulation strength (thin dashed curve) is unstable. Increase in the fresh water flux, which is equivalent to intensification in the haline forcing, can switch a thermal mode to a haline mode. The model with the geostrophic scaling law requires higher fresh water flux for a thermal mode to switch to a haline mode.

When $\tau_S \to \infty$, which is a condition for a proper restoring salinity boundary condition (Welander, 1986), $\xi \to 0$. The zero circulation line, $\eta = \xi\zeta$, which is the lower bound of the multiple equilibria region for models with the restoring salinity boundary condition as in Fig. 3.4, approaches $\eta = 0$. In this limit the cusp of the frictional model with the restoring salinity boundary condition at $(\zeta_o, \eta_o) = (\xi[1-\xi]^{-1}, \xi^2[1-\xi]^{-1})$ (Thual and McWilliams, 1992) approaches the origin $(0,0)$. At this cusp, the upper bound of the multiple equilibria and the zero circulation line meet as in Fig. 3.4. If the salinity restoring boundary condition

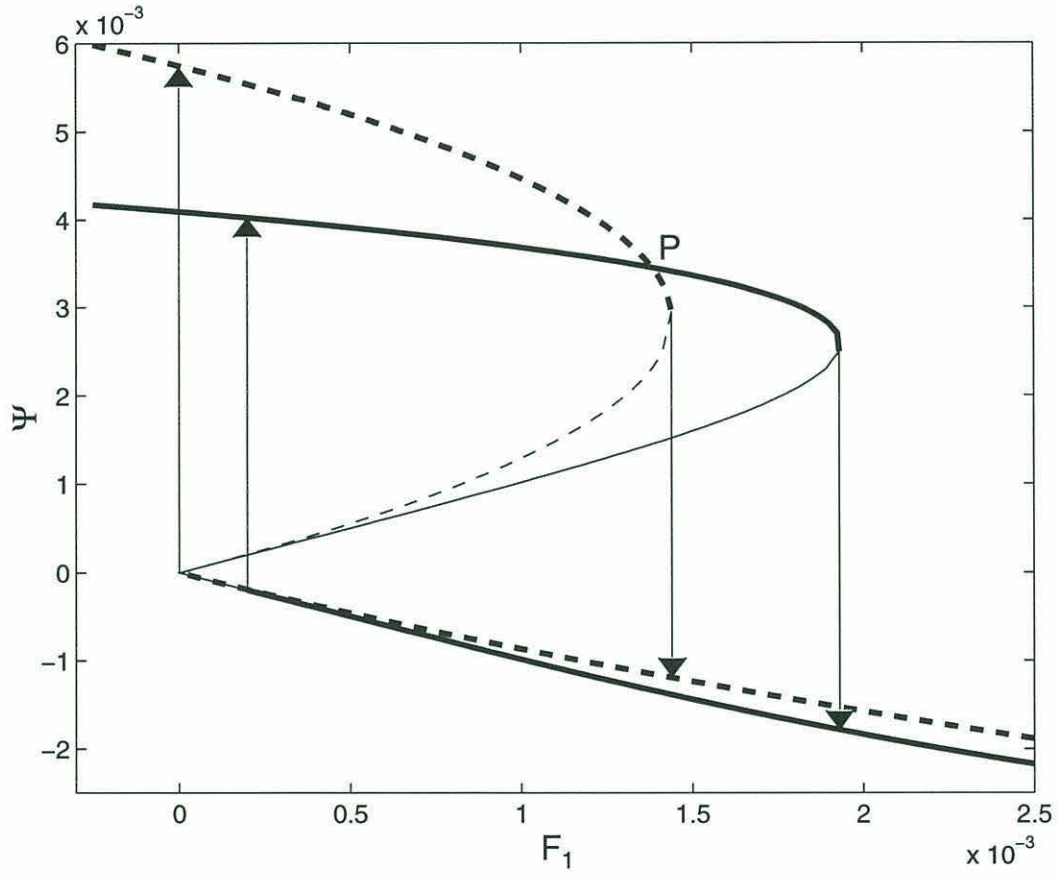

Figure 3.6: The mass transport Ψ versus F_1 with $\tau = 1$. The solid curves are for the geostrophic model and the dashed curves are for the frictional model. The arrows indicate the direction of change in each case. The middle branches (thin lines) in each case are for the unstable thermal modes.

is used properly as Welander (1986) suggested, a haline mode is possible if the haline forcing and the thermal forcing are in opposite direction as in models with the interactive condition (as in Fig. 3.6) or the fresh water flux (Huang, *et al.*, 1992).

As Nakamura *et al.* (1995) and Marotzke and Stone (1995) show, the change in the salinity boundary condition from the restoring one to the interactive condition, moves the upper catastrophic transition points toward the present state. In the geostrophic model, the effect is small so that the transition point is still quite far away from the present state. In the frictional model, the effect is strong so that a small change in the fresh water flux could drive the present circulation to a haline mode. Thus, the mass transport relation has stronger effect on the stability of thermohaline circulation than the parameterization of the air-sea fresh water exchange. This comparison is, however, qualitative.

Using a linear stability analysis, we can study processes that affect the transition point or the stability of a circulation quantitatively. Since we know that the transition point from a haline mode to a thermal mode is either zero circulation line, $\eta = \xi\zeta$ (with the restoring salinity boundary condition) or $F_1 = 0$ (with the interactive condition), a linear stability analysis was done with a thermal mode circulation in each case.

Apply a small perturbation (Θ', Σ') to an equilibrium thermal mode circulation $(\overline{\Theta}, \overline{\Sigma})$ without changing the parameters related to the boundary conditions such as ζ and η (or F_1). In the geostrophic model with the restoring salinity boundary condition, $\overline{\Theta}$ and $\overline{\Sigma}$ satisfy

$$\zeta - \overline{\Theta}(\tau + \overline{\Psi}) = 0, \text{ and } \eta - \overline{\Sigma}(\tau\xi + \overline{\Psi}) = 0.$$

The equations for the perturbation variables from Eq. 3.3 are as follows:

$$\begin{aligned} \dot{\Theta}' &= -\{\Theta'(\tau + \overline{\Psi}) + \overline{\Theta}\overline{\Psi}\Psi'\} \\ \dot{\Sigma}' &= -\{\Sigma'(\tau\xi + \overline{\Psi}) + \overline{\Sigma}\overline{\Psi}\Psi'\}. \end{aligned} \tag{3.7}$$

The mass transport $\Psi = \overline{\Psi} + \Psi'$ also can be written as

$$\begin{aligned} \Psi_G &= \lambda\{(\overline{\Theta} - \overline{\Sigma}) + (\Theta' - \Sigma')\}^{1/3} \\ &= \lambda(\overline{\Theta} - \overline{\Sigma})^{1/3} + \frac{1}{3}\lambda(\overline{\Theta} - \overline{\Sigma})^{-2/3}(\Theta' - \Sigma') + \mathbf{O}(\Theta', \Sigma')^2. \end{aligned}$$

Thus,

$$\Psi' = \frac{1}{3}\lambda^3\overline{\Psi}^{-2}(\Theta' - \Sigma'), \text{ and } \overline{\Psi} = \lambda(\overline{\Theta} - \overline{\Sigma})^{1/3}. \tag{3.8}$$

If we rewrite Eq. 3.7 using a matrix form,

$$\begin{pmatrix} \dot{\Theta}' \\ \dot{\Sigma}' \end{pmatrix} = \mathbf{A} \begin{pmatrix} \Theta' \\ \Sigma' \end{pmatrix} \tag{3.9}$$

where

$$\mathbf{A} \equiv \begin{pmatrix} a & b \\ c & d \end{pmatrix}$$

with

$$\begin{aligned} a &= -(1 + 1\overline{\Psi} + \frac{1}{3}\lambda^3\overline{\Theta\Psi}^{-2}) & b &= \frac{1}{3}\lambda^3\overline{\Theta\Psi}^{-2} \\ c &= -\frac{1}{3}\lambda^3\overline{\Sigma\Psi}^{-2} & d &= -(\tau\xi + \overline{\Psi} - \frac{1}{3}\lambda^3\overline{\Sigma\Psi}^{-2}). \end{aligned} \tag{3.10}$$

If we apply the same procedure to other models, the perturbation equation satisfies Eq. 3.9, while $\mathbf{A}$ for each case is as follows:

frictional model with restoring	$\mathbf{A} = \begin{pmatrix} -\tau - \overline{\Psi} - \overline{\Theta\Psi} & \overline{\Theta\Psi} \\ -\overline{\Sigma\Psi} & -\tau\xi - \overline{\Psi} + \overline{\Sigma\Psi} \end{pmatrix}$
geostrophic model with interactive condition	$\mathbf{A} = \begin{pmatrix} -1 - \overline{\Psi} - \frac{1}{3}\lambda^3\overline{\Theta\Psi}^{-2} & \frac{1}{3}\lambda^3\overline{\Theta\Psi}^{-2} \\ F_1 - \frac{1}{3}\lambda^3\overline{\Sigma\Psi}^{-2} & -\overline{\Psi} + \frac{1}{3}\lambda^3\overline{\Sigma\Psi}^{-2} \end{pmatrix}$
frictional model with interactive condition	$\mathbf{A} = \begin{pmatrix} -\tau - \overline{\Psi} - \overline{\Theta\Psi} & \overline{\Theta\Psi} \\ F_1 - \overline{\Sigma\Psi} & -\overline{\Psi} + \overline{\Sigma\Psi} \end{pmatrix}$.

(3.11)

The matrix $\mathbf{A}$ and its eigenvalues represent the feedback and stability of each model. Since the sum of the two eigenvalues of a model is

$$\text{trace}(\mathbf{A}) < 0,$$

if the product of the two eigenvalues

$$\det(\mathbf{A}) = ad - bc > 0,$$

the eigenvalues are negative and the equilibrium solution of the model is stable. If not, one of the eigenvalues is positive and the equilibrium solution is unstable to the perturbation.

When commonly used temperature restoring time scale, which is $\tau_T \approx 100$ days, and equilibrium thermal mode solutions are applied to the matrix $\mathbf{A}$, then $a \gg b, c, d$ and $a \approx -\tau \approx -1$ in all four models. Thus, a thermal mode circulation is stable if

$$\det(\mathbf{A}) \approx -\mathrm{d} > 0. \tag{3.12}$$

The stability condition $d < 0$, in fact, holds when $\tau > 0.1$, i.e., $\tau_T > 1000$ days. In this limit, in the models with the interactive condition, the stability is independent of the salinity boundary condition, since F_1, the moisture transport coefficient, is in c.

As in Walin (1985), for a moment assume that the effect of the salinity restoring boundary condition $-\tau\xi$, is negligible. (The term $-\tau\xi < 0$ so it stabilizes circulation and the effect is discussed later more detail.) The stability condition is independent of the salinity boundary conditions at all in all four models; it is completely determined by the advection related properties. The advection of the salinity perturbation due to the equilibrium circulation $-\overline{\Psi}$ makes negative contribution to d so it stabilizes the circulation. The advection of the equilibrium salinity gradient due to the circulation driven by the salinity perturbation ($\lambda^3\overline{\Sigma}\overline{\Psi}^{-2}$ in geostrophic models or $\overline{\Sigma}$ in frictional model) makes positive contribution to d; this is the **only** destabilizing mechanism.

The stability condition, $-d > 0$, shows that the geostrophic thermal mode is stable when the density ratio R, which is the ratio of the meridional salinity difference $\overline{\Sigma}$ to the meridional temperature difference $\overline{\Theta}$, satisfies

$$R \equiv \frac{\overline{\Sigma}}{\overline{\Theta}} < R_c = \frac{3}{4}, \tag{3.13}$$

regardless of the salinity boundary conditions. Note that the circulation becomes unstable before the salinity gradient becomes as strong as the temperature gradient, i.e., $R = 1$. One can easily show that when $\Psi \sim \Delta\rho^{1/n}$, a thermal mode is stable to a small perturbation if $R < n/(n+1)$. Thus, the frictional thermal mode is stable when

$$R < R_c = \frac{1}{2},$$

as Walin (1985) and Marotzke (1990) show. Tziperman *et al.*'s (1994) frictional four-box model shows that the critical value would decrease to about 0.45 mainly due to the

increase in the resolution. Such a small difference may not be significant in such simple models, especially when we are to apply the result to more complicated systems such as the oceans or 2 or 3-dimensional numerical models. The geostrophic model, however, yields a critical value that is 50% larger than that from the frictional one, so the difference must be significant.

It is easy, in fact, to find R that satisfies $\det(\mathbf{A}) > \mathbf{0}$ for each model. In Fig. 3.7, a curve (R_c), which satisfies $\det(\mathbf{A})=0$, is presented for several different cases. To the left of a curve $\det(\mathbf{A}) > 0$ so the model is stable. To the right of a curve $\det(\mathbf{A}) < 0$ so the model is unstable. Since the strong negative feedback between the sea surface temperature and the atmosphere does not allow much change in temperature, $\overline{\Theta}$ is fixed to $\Theta_o = 0.00577$. Although the temperature restoring time τ_T is varied, $\xi = \tau_T/\tau_S$ is fixed to 0.002. In the figure, the results from the models with the interactive feedback in which $H_s \sim F_{3.5}\Theta^{3.5}$ as in Nakamura *et al* (1994) are included. Since $F_1\Theta_o = F_n\Theta_o^n$, $H_s' \sim nF_n\overline{\Theta}^{n-1}\Theta' = nF_n(\overline{\Theta}/\Theta_o)^{n-1}\Theta'$, where Θ_o is the meridional temperature gradient of the present model ocean. By replacing F_1 in c of $\mathbf{A}$ to $nF_1(\overline{\Theta}/\Theta_o)^{n-1}$ with $n = 3.5$, we can get the curves $g1$ and $f1$.

The models with the geostrophic mass transport law show greater stability than those with the frictional law when the same salinity boundary conditions are used. The largest contribution to $\det(\mathbf{A})$ is from the competition between the advection of the salinity perturbation by the equilibrium circulation and the advection of the mean salinity gradient due to the circulation induced by the salinity perturbation ($-\tau d$ for the model with the interactive condition, or $-\tau(d+\tau\xi)$ for the model with the restoring salinity condition). Thus, change in the mass transport law makes the largest contribution to the stability; the stabilizing effect due to the geostrophic mass transport law is stronger than any other feedbacks in the models. The faster circulation in the geostrophic model weakens the meridional salinity gradient and removes the salinity anomalies more effectively. The water in each box does not have enough time to obtain a strong enough salinity gradient. A stronger haline forcing is required to reverse a thermal mode circulation in the geostrophic model.

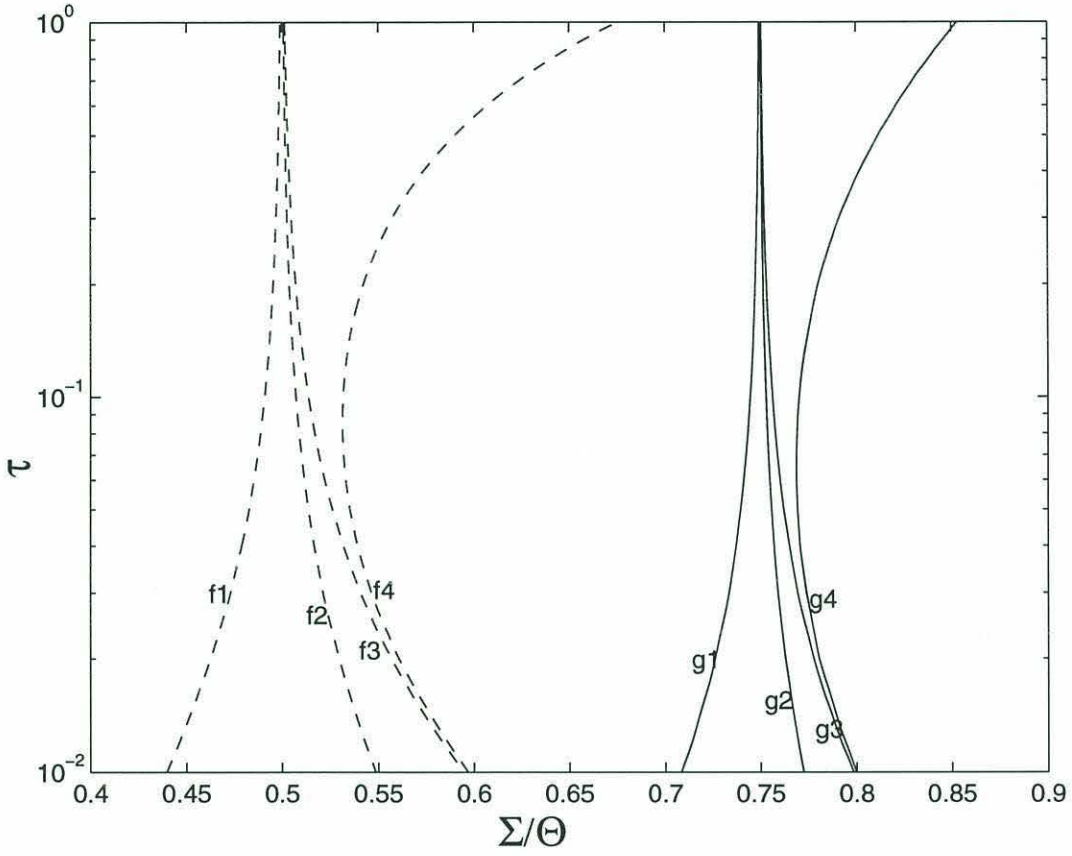

Figure 3.7: Stability diagram. A curve denotes R_c that makes $\det(\mathbf{A}) = 0$ for a certain model as τ varies while $\xi = \tau_T/\tau_s = 0.002$ and $\overline{\Theta} = \Theta_o = 0.00577$, which is equivalent to $20°C$, and $F_1 = 1.38 \times 10^{-3}$. To the left of a curve, $\det(\mathbf{A}) > 0$ so the thermal mode circulation of the model is stable. To the right, $\det(\mathbf{A}) < 0$ so the thermal mode circulation is unstable. Note that the same equilibrium solutions are compared so that the boundary forcings are not necessarily the same for each case. The results from the models with the geostrophic scaling law are labeled using the character 'g', and those with the frictional scaling laws are labeled using the character 'f'. The results of the models with the interactive condition with $n = 3.5$ are labeled using '1' and with $n = 1$ using '2', those with fixed $(E-P)$ (or the interactive condition with $n = 0$) using '3', and those with the restoring boundary condition using '4'.

When $\tau > 0.1$, in Fig. 3.7 the critical values with the restoring salinity boundary condition ($f4$ and $g4$) show greater stability than those with fixed $(E-P)$. Within this range of τ, $\det(\mathbf{A})$ and the stability are mostly determined by ad, which becomes larger as τ increases. Thus, the interactive condition, whose effect is in c, does not make much contribution to the stability regardless of n. The term a is independent of the salinity boundary conditions, so the difference in the stability is solely due to $\tau\xi = 100$ days$/\tau_S$, which represents the effect of salinity restoring and is neglected in the previous analysis, in d. The difference becomes smaller as τ decreases, since ξ is fixed so that τ_S increases and the dependence of salinity boundary condition on the sea surface salinity weakens. In this study $\xi = \tau_T/\tau_S = 0.002$ so it is about two orders of magnitude smaller than commonly used values in other studies, but the effect is significant. Such an artificial stability does not exist in a system whose salinity boundary condition is independent of salinity such as the real oceans, models with fixed (E-P) or the interactive condition.

In Fig. 3.7, R_c decreases ($f1$ and $g1$) or increases (all the rest) depending models, when τ varies. One might conclude that the temperature restoring could be stabilizing or destabilizing depending on the configuration of a model and the restoring time scale. We can rewrite the stability condition, $\det(\mathbf{A}) > \mathbf{0}$, as follows:

$$\begin{aligned} d + \tau\xi &> \frac{bc}{a} + \tau\xi \text{ (the models with the restoring salinity b.c.), or} \\ d &> \frac{bc}{a} \text{ (the models with the interactive condition),} \end{aligned} \tag{3.14}$$

where a, b, c and d are given in Eq. 3.10 or Eq. 3.11.

For the temperature restoring to change its role in the stability, the left or right hand side of the above equation has to change its sign as τ varies. The left hand sides of the equation, b and c are independent of τ. The term a (and $\tau\xi$ for the models with salinity restoring boundary condition) is dependent upon τ so the magnitude changes as τ varies, but the signs remain the same within the parameter range of this study, 100 days $\leq \tau_T \leq$ 10000 days. As the name suggests, the temperature restoring boundary condition always restores a system to the reference temperature. As the temperature restoring time scale becomes larger, its effect becomes smaller; but it remains as a stabilizing process.

In Eq. 3.14, as τ declines a becomes smaller so that the right hand side becomes larger. In models with the salinity restoring boundary condition, $bc < 0$ and $a < 0$. So bc/a, which is the advection of the temperature gradient or the advection induced by the temperature gradient, becomes a larger positive number, and stabilizes circulation. At the same time, however, $\tau\xi$ decreases. Since it is larger than bc/a if $\tau > 0.1$ or so, the right hand side shows minimum around $\tau \approx 1$ and so does R_c (curves $g4$ and $f4$ in Fig. 3.7).

As Nakamura *et al.* (1994), Marotzke and Stone (1995), and Marotzke (1996) show, the models with the interactive condition (curves $f1$ and $f2$, or $g1$ and $g2$) yields lower stability than those with fixed $(E - P)$ (curves $f3$ or $g3$), if the same mass transport law is used. The positive feedback due to the interactive condition becomes stronger as n increases (Marotzke, 1996). For a parameter appropriate for the present North Atlantic, the models with $n = 3.5$ (curves $f1$ and $g1$) show lower stability than those with $n = 1$ (curves $f2$ and or $g2$). Furthermore when $n = 1$, $c < 0$ and $bc/a > 0$. The right side of Eq 3.14 increases as τ decreases and so does R_c (curves $g2$ and $f2$ in Fig. 3.7). When $n = 3.5$, the effect of the interactive condition is large enough to make $c > 0$. Thus the right hand side decreases as τ increases and so does R_c (curves $g1$ and $f1$).

The air-sea heat fluxes versus η from the models with the restoring salinity boundary conditions are shown in Fig. 3.8. The fluxes are calculated from the stable equilibrium temperature and salinity in the polar boxes, which were obtained during the calculation for Fig. 3.5. The lower branches are for the thermal modes and the upper ones are for the haline modes. In an equilibrium, the boundary fluxes are the same as the meridional fluxes. A haline mode circulation is much slower than a thermal mode circulation. The advection of heat from the equator to the polar box is significantly reduced so that the surface heat flux is low.

The North Pacific is about two times wider than the North Atlantic. If the heat transport processes are the same in the two oceans, the meridional heat transport of the North Pacific must be about twice as large as that of the North Atlantic. Estimations using hydrography, however, show that the heat transport of the North Pacific (Bryden *et al.*, 1991) is about

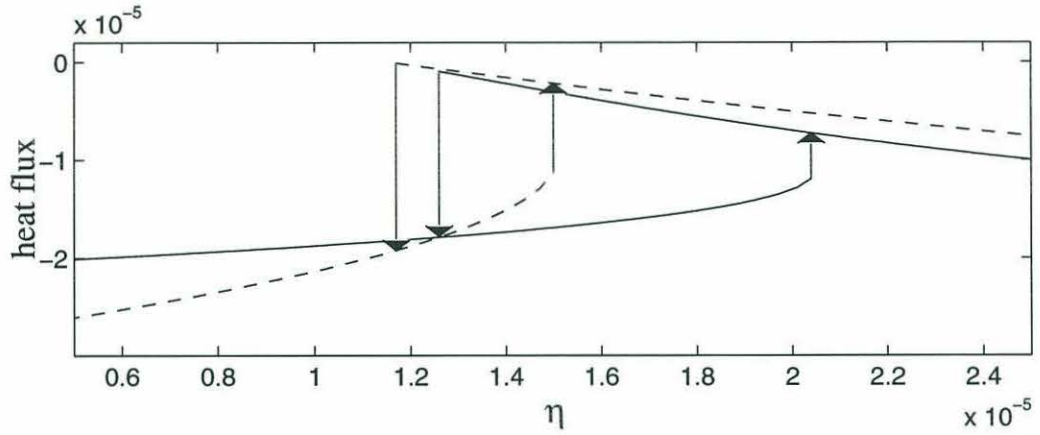

Figure 3.8: Surface heat fluxes versus η in the polar box when $\zeta = 0.00577$ and $\tau = 1$. The solid curves are for the geostrophic model and the dashed ones are for the frictional model. The lower branches are for the thermal modes and the upper branches are for the haline modes. A negative value means heat flux from the ocean to the atmosphere.

half that of the North Atlantic (Bryden and Hall, 1980; Hall and Bryden, 1982). This might be evidence that the North Pacific is thought to be in a haline mode (Warren, 1983), with smaller meridional heat flux and higher surface salinity gradient than those of the North Atlantic.

When the haline forcing changes, the geostrophic model shows smaller change in the surface heat flux as can be seen in Fig. 3.8. When $\Delta\rho > \Delta\rho_c$, the mass transport in the geostrophic model is less sensitive to the change in $\Delta\rho$, which could be induced by change in η, as shown in Fig. 3.2. Subsequently, the meridional heat transport and the air-sea heat exchange are less sensitive to the change in $\Delta\rho$ or η as shown in Fig. 3.8. Before the transition, the heat flux is similar in both models. After the transition, however, the stronger circulation of the geostrophic model allows larger meridional heat flux and thereby the air-sea heat flux. Thus, the geostrophic model shows smaller change in surface heat flux during the catastrophic transition, although it is very unlikely that the thermohaline catastrophe occurs in the geostrophic model.

The changes in Ψ and the heat flux during the catastrophic transition from a thermal mode to a haline mode in the models with the restoring salinity boundary condition are

shown in Fig. 3.9. The solid line is for the geostrophic model and the dotted line is for the frictional model. At $t < 0$, the geostrophic model is in a stable thermal mode with $\eta = 1.98 \times 10^{-5}$, and the frictional one with $\eta = 1.44 \times 10^{-5}$. At $t = 0$, η was increased by 0.12×10^{-5} in both cases to allow the catastrophic transitions from the thermal modes to haline modes. In both cases, the mass transports initially decrease slowly while maintaining thermal modes. Then the circulation reverses to haline modes suddenly.

The transition time scale of the frictional model is about 800 *years*, which is comparable to that of Huang *et al.*'s (1992) frictional model with the natural salinity boundary condition. The transition in the geostrophic model is about twice as fast as that in the frictional model. As $\Delta\rho \to 0$, the geostrophic mass transport becomes larger relative to the frictional one so that the transition is faster in the geostrophic model. During the reversal, $|\Psi| \approx 0$ so that the temperature of each box becomes very close to its restoring temperature. The heat flux becomes very small. After the reversal, the circulation redistributes the heat so that the air-sea heat exchange occurs again. The sudden reversal in the circulation accompanies a sharp peak in heat flux, whose width is related to the duration of the reversal.

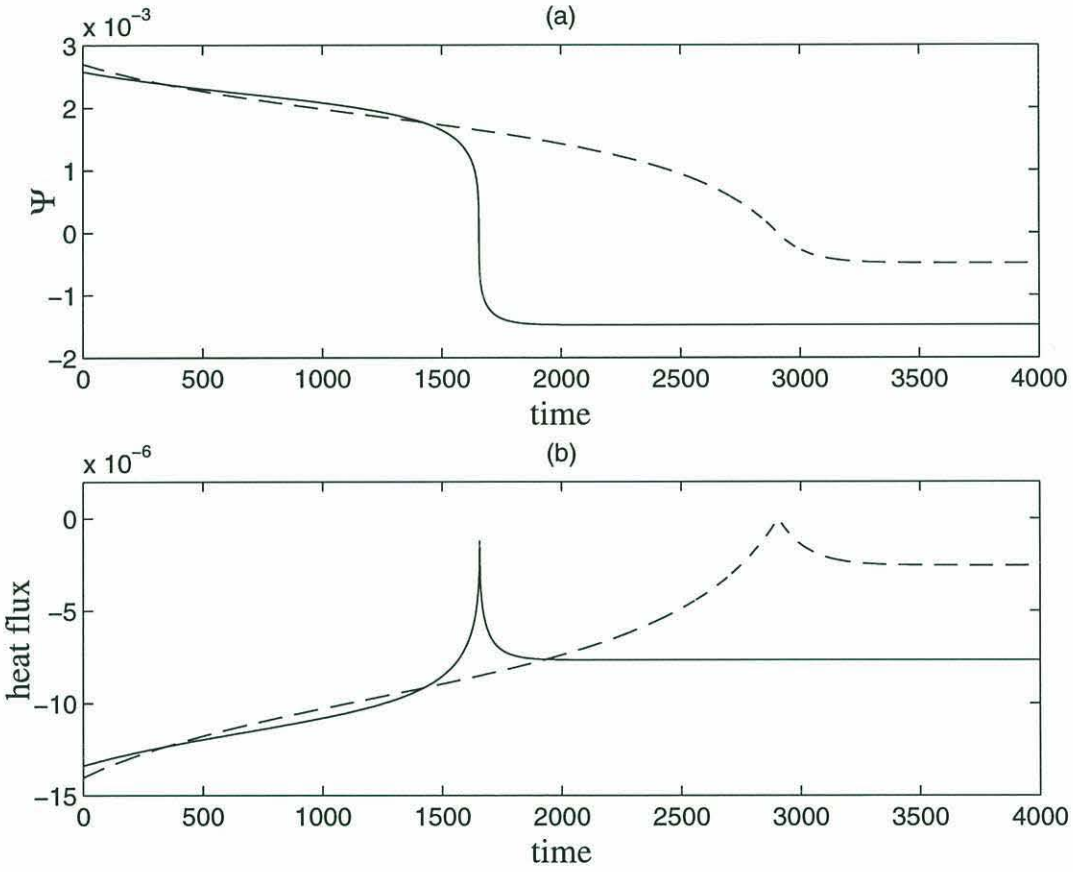

Figure 3.9: Time evolution during the catastrophic transition. The solid line is for the geostrophic model and the dotted line is for the frictional model. In both cases $\zeta = 0.00577$ and $\tau = 1$. In the geostrophic model, η was changed from 1.98×10^{-5} by 0.12×10^{-5} at $t = 0$. In the frictional model, η was changed from 1.44×10^{-5} by 0.12×10^{-5} at $t = 0$. One hundred days is equivalent to a nondimensionalized unit time.

3.3 Discussion and Conclusion

A two-box model using a mass transport law based on geostrophy and advective diffusive heat balance (geostrophic mass transport law) has been developed. The stability of a thermal mode (high latitude sinking) circulation against perturbation in salinity has been studied. The results are compared to those from a model using a traditional frictional law. The effects of the air-sea fresh water exchange parameterization on the stability of thermohaline circulation also have been studied and compared to those due to the mass transport law parameterization.

A simple linear stability analysis shows that the stability of a thermal mode is mostly determined by the competition between the mean advection of the salinity anomaly, which is a stabilizing process, and the advection of the mean salinity gradient due to the circulation induced by the salinity anomaly, which is the strongest destabilizing process. In a model with the geostrophic transport law, the circulation is stronger than that in a model with the frictional law. The stronger circulation reduces the meridional salinity gradient and removes the salinity anomaly effectively. Thus, the models with the geostrophic transport law show significantly greater stability. Some studies based on the frictional model suggested that the present North Atlantic is close to the stability boundary so that an increase in the polar fresh water flux might cause a catastrophic change in the circulation. The result from the geostrophic model, however, suggests that the present ocean is quite far away from the stability boundary so that such a change is unlikely to occur.

A similar argument can be applied to a zonally averaged thermohaline circulation model. While averaging the equation of motion, information on the zonal structure, which drives a meridional circulation, is lost. To close the equation, some assumptions on the zonal structure were made. For example, in Marotzke *et al.* (1988), a local and linear relation between the mean meridional velocity and the meridional pressure gradient,

$$A_* \overline{v}_{zz} = \overline{p}_y,$$

was assumed, with a large value of viscosity A_* adopted to reduce the transport to the

present oceanic value. The frictional balance is also used in other 2-dimensional thermohaline circulation models such as Thual and McWilliams (1992) and Quon and Ghil (1992). Thus, the results of those models may be different from those of the geostrophically balanced oceans.

The stability analysis also show that a restoring salinity boundary condition stabilizes a thermal mode circulation significantly when $\tau_T < 3$ years. Such stability does not exist in the real world, however. The artificial stability becomes stronger as the salinity restoring time scale τ_S becomes smaller. In this study, the ratio of τ_T, the temperature restoring time scale, to τ_S, $\xi = \tau_T/\tau_S = 0.002$. It is about two orders of magnitude smaller than those in similar studies, but its effect is significant. The effect disappears as $\tau_S \to \infty$, which is a condition for a proper salinity restoring boundary condition (Welander, 1986), so that the boundary condition for salinity becomes independent of the surface salinity. Salinity boundary conditions such as natural boundary condition (Huang, 1993) or virtual salt fluxes from fixed (E-P) or the interactive condition do not introduces such artificial stability, obviously.

In many two or three dimensional numerical studies about the stability of thermohaline circulation, a model was initialized using a restoring salinity boundary condition with $1 < \xi < 0.1$. After the circulation reaching an equilibrium state, virtual salt fluxes at the sea surface were estimated. When the restoring boundary condition was replaced by the virtual salt flux diagnosed, the circulation showed rapid transition to different states, in some cases. It has been argued that such transition suggests that the thermohaline circulation is unstable under mixed boundary conditions (a restoring boundary condition for temperature and a flux boundary condition for salinity). The change in the salinity boundary condition removes the unnatural stability is externally. Thus, it is not clear that the transition induced by the external removal of the artificial stability or instability in the circulation.

A restoring temperature boundary condition always tries to restore temperature to a reference value. Thus, it is always stabilizing process regardless of the restoring time scale, τ_T, and salinity boundary conditions. As τ_T becomes larger, its stabilizing effect becomes

less dominant so that other processes begin to modify the stability. The modifications are small, especially when $\tau_T < 3$ years and not significant.

The models and the real oceans are so different that one can ask what is the proper choice of the tuning parameters $\Delta\rho_p$ and Ψ_p, and how does the stability and the bifurcation structure depend on the choice. As evident from the preceding analysis, the stability of a thermal mode is mainly determined by the advection of the salinity gradient. Although $\Delta\rho_p$ and Ψ_p of the study are just one realization of the real oceanic values, they are known to well within the correct order of magnitude. As long as Ψ_G is significantly larger than Ψ_F when $\Delta\rho < \Delta\rho_p$, the thermal mode of a model with the geostrophic mass transport law is significantly more stable than that of a model with the frictional mass transport law.

Although we cannot apply the model to the oceans directly, we can roughly estimate the stability parameter of the oceans. The surface temperature and salinity distribution of the North Atlantic give $\overline{\Theta}_{N.A.} \approx 20°C$ and $\overline{\Sigma}_{N.A.} \approx 2ppt$ so $R_{N.A.} \approx 0.4$. In the North Pacific, $\overline{\Theta}_{N.P.} \approx 20°C$ and $\overline{\Sigma}_{N.P.} \approx 3ppt$ so $R_{N.P.} \approx 0.6$. If we use the frictional model, both stability parameters are close to the critical value 0.5 so we may conclude that both oceans are close to the catastrophic transition or they are in haline mode as Walin (1985) and Huang *et al.* (1992) argue. If we use the geostrophic model, $R_{N.A.}$ is significantly smaller than the critical value 0.75 so we may conclude that the thermohaline circulation of the North Atlantic is stable to a small change in the fresh water flux. In the case of the North Pacific, $R_{N.P.}$ is closer to the critical value so we may conclude that the North Pacific is close to the transition or in a haline mode. (During a haline mode $R > 1$ always regardless of model configuration so we can easily see the limitation of the model.) We also may argue that this is consistent with Warren (1983) who showed that the fresh flux to the northern North Pacific prevents the deep water mass formation so the direction of the thermohaline circulation in the ocean is opposite to that of the North Atlantic.

Chapter 4

Summary and Conclusion

A convection experiment was done in a rotating rectangular tank. Buoyancy forcing was applied by differentially heating the bottom of the tank using an electrical heater of constant heat flux and a cooling plate of constant temperature. The experiment was equivalent to an upside-down f-plane ocean.

In an equilibrium, the heat flux due to the heating pad was equivalent to the meridional heat flux (heat flux from the heating pad to the cooling plate due to the convective circulation) within the experimental error. Since the meridional heat flux was a known experimental parameter, the temperature measurement with an array of thermistors allowed us to study scaling laws for the meridional heat flux for the first time in such a laboratory convection experiment. Scaling laws for a thermal thermal boundary layer were also studied.

A thin thermal boundary layer along with an interior of almost homogeneous temperature was observed, in agreement with other convection experiments with differential bottom heating. The comparison between the experiment and scaling laws developed earlier showed that most of the meridional heat flux was due to the meridional geostrophic flow with minor correction from the bottom friction. The same applied to the thermal boundary of the experiment.

Zonal temperature sections and flow visualization showed that over the cooling plate, the

cold water circulated anti-cyclonically and the warm water above the cold water circulated cyclonically. The flow pattern is consistent with a simple balance between the squashing (in the cold water) or stretching (in the warm water) of a vortex column and the dissipation of vorticity in the bottom frictional layer (in the cold water) or in the side wall frictional layer (in the warm water). Most of the cold water flowed toward the hot end along the wall to the left (looking from the hot end to the cold end). The hot flow toward the cold end was along the center of the tank but most of that water returned to the hot end along the side walls. The zonal temperature sections show that the flows satisfy geostrophy.

The estimation of the meridional heat transport in the North Atlantic from hydrographic data (Bryden and Hall, 1980; Hall and Bryden, 1982) is compared with that using the geostrophic scaling law. The meridional heat transport of the North Pacific is also available (Bryden *et. al.*, 1991), but deep water mass formation does not occur there (Warren, 1983). It is not appropriate for comparison.

The estimation of the total meridional heat transport in the North Atlantic across $25°N$ using hydrographic data is $1.22 \times 10^{15}W$ (Bryden and Hall, 1980; Hall and Bryden, 1982). If the contribution added due to the surface Ekman flux driven by the wind, which is $0.42 \times 10^{15}W$, is considered, the estimation becomes $0.8 \times 10^{15}W$. If the canonical oceanic values related to the physical properties of the ocean, $l_x = 5000km$, $l_y = 5000km$, $d = 4km$, $\kappa = 1cm^2/sec$, and $\Delta T = 20°C$ are substitute to the scaling laws, the Ekman scaling law gives $H = 0.11 \times 10^{15}W$ and the geostrophic one gives $H = 1.3 \times 10^{15}W$. If the proportionality constant from the experiment, which is 0.26, is applied, the geostrophic scaling law predicts $H = 0.35 \times 10^{15}W$. The value is half of the estimated heat flux in the North Atlantic. Considering that there are heat fluxes across the equator in the Atlantic and one due to the wind driven gyres (and no equivalence in the experiment), which are included in that value of $0.8 \times 10^{15}W$, the prediction from the experiment is comparable to the estimated value in the North Atlantic.

The estimations of the abyssal eddy diffusivity from microstructure measurement shows that κ varies spatially (Toole *et. al*, 1994), although it is assumed uniform throughout this

study. The estimated average value, furthermore, is $0.1cm^2s^{-1}$ to $0.5cm^2s^{-1}$ and smaller than that used in the estimation of the North Atlantic meridional heat transport. The estimation of κ, however, becomes larger up to $2cm^2s^{-1}$ near slopes in some regions. In the thermocline layer or the western boundary, the motion is more active so that turbulent and eddy diffusivity would intensify. A proper value of κ is not available yet so it must be proper saying that when $\kappa \approx 1cm^2s^{-1}$ within upper $1000m$ or so of the oceans, the geostrophic scaling law predicts meridional heat transport comparable to the observed one in the North Atlantic.

The thermocline depth from the geostrophic scaling law is about $200m$ so it is much smaller than the oceanic one. The surface wind stress mainly determines the thermocline depth so that the geostrophic scaling law cannot be used for that purpose. When the typical oceanic values as described in the previous paragraph are used in the Ekman scaling law in Table 2.1, it gives an about $30km$ deep thermocline, which is far larger than the depth of the oceans.

Naturally, this experiment is a very idealized model of the oceanic convective circulation. We do not claim that the geostrophic scaling applies in detail to the oceans, however, it may have some important use in climate modeling. To demonstrate one application, the stability of the thermohaline circulation was studied using a two-box model. Since the low resolution of such a model does not allow one to include the Earth's rotation explicitly, the effect of the rotation, which has been ignored previously in this problem, was included by introducing the meridional mass transport from the geostrophic scaling law. The results are compared with those obtained with the traditional frictional scaling law based on the balance between a meridional pressure gradient and frictional dissipation.

The geostrophic model is significantly more stable than the frictional model under perturbations in salinity, suggesting the thermohaline catastrophe is less likely to occur in the present North Atlantic if the effects of the Earth's rotation is considered. As the polar salinity decreases the geostrophic mass transport becomes relatively stronger than the frictional transport. In the former, a salinity anomaly is removed more rapidly so a significantly

higher perturbation in the polar salinity is required before the onset of the thermohaline catastrophe. The heat accumulated in the equatorial oceans is redistributed more effectively so that the model shows a smaller change in the climate as the buoyancy forcing varies.

Using a simple linear stability analysis, the effects of various feedbacks were also studied. The feedback due to the meridional mass transport is the strongest, thus has the strongest effect on the stability. The analysis also shows that a salinity restoring boundary condition significantly stabilizes a thermal mode circulation unless the salinity restoring time scale, τ_S, is several orders of magnitude larger than the temperature restoring time scale, τ_T. Other feedbacks affect the stability significantly only when τ_T becomes larger than about 3 years.

The results of the box model show that we have be careful about the parameterization of physical processes especially in a simple model.

REFERENCES

Barcilon, V and J. Pedlosky, 1967, Linear theory of rotating stratified fluid motions. *J. Fluid Mech.*, **29**, 1-16.

Beardsley, R. C. and J. F. Festa, 1972, A numerical model of convection driven by a surface stress and non-uniform horizontal heating. *J. Phys. Oceanogr.*, **2**, 444-455.

Bryan, F., 1987, Parameter sensitivity of primitive equation ocean general circulation models. *J. Phys. Oceanogr.*, **17**, 970-985.

Bryan, K., 1991, Poleward heat transport in the ocean. *Tellus*, **43AB**, 104-115.

Bryan, K. and M. D. Cox, 1967, A numerical investigation of the oceanic general circulation. *Tellus*, **19**, 54-80.

Bryan, K. and M. D. Cox, 1968, A non-linear model of an ocean driven by wind and differential heating. Part 1, Description of the three-dimensional velocity and temperature fields. *J. Atmos. Sci.*, 25, 945-967.

Bryden, H. L. and M. M. Hall, 1980, Heat transport by currents across $25°N$ latitude in the Atlantic Ocean. *Science*, **207**, 884-886.

Bryden, H. L., D. H. Roemmich, and J. A. Church, 1991, Ocean heat transport across $24°N$ in the Pacific. *Deep-Sea Res.*, **38**, 297-324

Colin de Verdière, A., 1988, Buoyancy driven planetary flows. *J. Marine Res.*, **46**, 215-265.

Condie, S. A., 1989, A laboratory model of a convectively driven ocean. *Dyn. Atmos. Oceans*, **13**, 77-94.

Condie, S. A. and R. W. Griffiths, 1989, Convection in a rotating cavity: modelling ocean circulation. *J. Fluid Mech.*, **207**, 453-474.

Green, J. S. A., 1970, Transfer properties of the large-scale eddies and the general circulation of the atmosphere. *Quart. J. Roy. Meteor. Soc.*, **96**, 157-185.

Goldsbrough, G. R., 1933, Ocean currents produced by evaporation and precipitation. *Proc. Roy. Soc.*, **A141**, 512-517.

Hall, M. M. and H. L. Bryden, 1982, Direct estimates of ocean heat transport. *Deep-Sea Res.*, **29**, 339-359.

Haney, R. L., 1971, Surface thermal boundary condition for ocean circulation models. *J. Phys. Oceanogr.*, **1**, 241-248.

Hignett, P., A. Ibbetson and P. D. Killworth, 1981, On rotating thermal convection driven by non-uniform heating from below. *J. Fluid Mech.*, **109**, 161-187.

Huang, R. X., 1984, *The Thermocline and Current Structure in Subtropical/Subpolar Basins. Ph. D. Thesis.* MIT/WHOI-84-42, 218pp.

Huang, R. X., 1988, On boundary value problems of the ideal-fluid thermocline. *J. Phys. Oceanogr.*, **18**, 619-641.

Huang, R. X., 1993, Real freshwater flux as a natural boundary condition for the salinity balance and thermohaline circulation forced by evaporation and precipitation. *J. Phys. Oceanogr.*, **23**, 2428-2446.

Huang, R. X., 1995, Advances in theories of wind-driven and thermohaline circulation, Joint Inst. Marine and Atmos. Res., U. Hawaii Manoa, SOEST-95-01, 213pp.

Huang, R. X. and R. L. Chou, 1994, Parameter sensitivity study of saline circulation. *Climate Dyn.*, **9**, 391-409.

Huang, R. X., J. R. Luyten, and H. M. Stommel, 1992, Multiple equilibrium states in combined thermal and saline circulation. *J. Phys. Oceanogr.*, **22**, 231-246

Huang, R. X. and R. W. Schmitt, 1993, The Goldsbrough-Stommel circulation of the world oceans. *J. Phys. Oceanogr.*, **23**, 1277-1284.

Hughes, T. M. and A. J. Weaver, 1994, Multiple Equilibria of an asymmetric two-basin ocean model. *J. Phys. Oceanogr.*, **24**, 619-637.

Holton, J. R., 1992, *An Introduction to Dynamic Meteorology. 3rd ed.* Academic Press, 511pp.

Joyce, T. M., 1991, Thermohaline catastrophe in a simple four-box model of the ocean climate. *J. Geophys. Res.*, **96**, 20393-20402.

Luyten, J. R., J. Pedlosky, and H. Stommel, 1983, The ventilated thermocline. *J. Phys. Oceanogr.*, **13**, 292-309.

Marotzke, J., 1990, *Instabilities and multiple equilibria of the thermohaline circulation.* Ph.D Thesis, Inst. Meereskund, Univ. Kiel, Germany, 126pp.

Marotzke, J., 1994, Ocean models in climate problems. *Ocean Processes in Climate Dynamics: Global and Mediterranean Examples,* P. Malanotte-Rizzoli and A. R. Robinson, eds., Kluwer, 79-109.

Marotzke, J., 1996, Analysis of thermohaline feedbacks. *Climate Variability: Dynamics and Predictability,* D. L. T. Anderson and J. Willebrand, eds., NATO ASI Series, *in press.*

Marotzke, J. and P. Stone, 1995, Atmospheric transports, the thermohaline circulation, and flux adjustments in a simple coupled model. *J. Phys. Oceanogr.*, **25**, 1350-1364.

Marotzke, J., P. Welander and J. Willebrand, 1988, Instability and multiple steady states in a meridional-plane model. *Tellus*, **40**, 162-172.

Menke, W., 1989, *Geophysical Data Analysis: Discrete Inverse Theory. revised ed.*, Academic Press, 289pp.

Munk, W. H., 1966, Abyssal recipes. *Deep-Sea Res.*, **13**, 707-730.

Nakamura, M., P. H. Stone and J. Marotzke, 1994, Destabilization of the thermohaline circulation by atmospheric eddy transports. *J. Climate*, **7**, 1870-1882.

Needler, G. T., 1967, A model for thermohaline circulation in an ocean of finite depth. *J. Marine Res.*, **25**, 329-342.

Nelken, H., 1987, *Thermally Driven Circulation. Sc. D. Thesis.*, MIT/WHOI, WHOI-87-33, 186pp.

Pedlosky, J., 1987 *Geophysical Fluid Dynamics. 2nd ed.*, Springer-Verlag, 710pp.

Press, W. H., B. P. Flannery, S. A. Teukolsky and W. T. Vetterling, 1986, *Numerical Recipes: the Art of Scientific Computing.* Cambridge University Press.

Quon, C. and M. Ghil, 1992, Multiple equilibria in the thermosolutal convection due to salt-flux boundary conditions. *J. Fluid Mech.*, **245**, 449-483.

Robinson, A. and H. Stommel, 1959, The oceanic thermocline and the associated thermohaline circulation. *Tellus*, **2**, 295-308.

Rossby, H. T., 1965, On thermal convection driven by non-uniform heating from below: an experimental study. *Deep-Sea Res.*, **12**, 9-16.

Salmon, R., 1990, The thermocline as an "internal boundary layer". *J. Marine Res.*, **48**, 437-467.

Somerville, R. C. J., 1967, A non-linear spectral model of convection in a fluid unevenly heated from below. *J. Atmos. Sci.*, **24**, 665-676.

Speer, K. G. and J. A. Whitehead, 1988, A gyre in a non-uniformly heated rotating fluid. *Deep-Sea Res.*, **35**, 1069-1077.

Stern, M. E, 1975, *Ocean Circulation Physics.* Academic press.

Stommel, H. M., 1957, A survey of ocean current theory. *Deep-Sea Res.*, **4**, 149-184.

Stommel, H. M., 1961, Thermohaline convection with two stable regimes of flow. *Tellus*, **13**, 224-230.

Stommel, H. M., 1965, *The Gulf Stream: a Physical and Dynamical Description.* 2nd ed., Univ. California, Berkeley, and Cambridge Univ. Press, London, 248+xiii pp.

Stommel, H. M., and A. B. Arons, 1960, On the abyssal circulation of the world ocean-I. Stationary planetary flow patterns on a sphere. *Deep-Sea Res.*, **6**, 140-154.

Stommel, H., and J. Webster, 1962, Some properties of thermocline equations. *J. Marine Res.*, **20**, 42-56.

Stone, P. H., 1972, A simplified radiative-dynamical model for the static stability of rotating atmospheres. *J. Atmos. Sci.*, **29**, 405-418.

Tziperman, E., J. R. Toggweiler, Y. Feliks, and K. Bryan, 1994, Instability of the thermohaline circulation with respect to mixed boundary conditions: is it really a problem for realistic models? *J. Phys. Oceanogr.*, **24**, 217-232.

Thual, O., and J. C. Mc Williams, 1992, The catastrophe structure of thermohaline convection in a two-dimensional fluid model and a comparison with low-order box models. *Geophys. Astrophys. Fluid Dyn.*, **64**, 67-95.

Veronis, G., 1976, Model of World ocean circulation: II. Thermally-driven, two-layer. *J. Marine Res.*, **34**, 199-216.

Vonder Haar, T. H. and A. H. Oort, 1973, New estimate of annual poleward energy transport by northern hemisphere oceans. *J. Phys. Oceanogr.*, **3**, 169-172.

Walin, G., 1985, The thermohaline circulation and the control of ice age. *Palaeoclimatol. Palaeoecol.*, **50**, 323-32.

Warren, B. A., 1983 Why there is no deep water formed in the North Pacific? *J. Marine Res.*, **41**, 327-347.

Weaver, A. J. and T. M. C. Hughes, 1992, Stability and Variability of the thermohaline circulation and its link to climate. *Trends Phys. Oceanogr.*, **1**, 15-70.

Welander, P., 1959, An advective model of the ocean thermocline, *Tellus*, **3**, 309-318.

Welander, P., 1971a, The thermocline problem. *Philosophical Transactions of the Royal Society, London*, **A.270**, 415-421.

Welander P., 1971b, Some exact solutions to the equations describing an ideal-fluid thermocline. *J. Marine Res.*, **29**, 60-68.

Welander, P., 1986 Thermocline effects in the ocean circulation and related simple model. In *Large-scale transport processes in oceans and atmosphere*, Willebrand, J. and Anderson, D. L. T. (Editors), 163-200, Reidel Publ. Co.

Whitehead, J. A., 1991, Small and mesoscale convection as observed in the laboratory. In *Deep convection and deep water formation*, Chu, P. C. and Gascard, J. C. (Editors), 355-368, Elsevier Sci. Pub.

Whitehead, J. A., 1995, Thermohaline ocean processes and models. *Annu. Rev. Fluid Mech.*, **27**, 89-113.

Winton, M., 1996, The role of horizontal boundaries in parameter sensitivity and decadal-scale variability of corse-resolution ocean general circulation models. *J. Phys. Oceanogr.*, **26**, 289-304.